

Arbeitsbericht NAB 13-83

**Gas related property distributions
in the proposed host rock
formations of the candidate siting
regions in Northern Switzerland
and in the Helvetic Zone**

December 2013

R. Senger, A. Papafotiou, P. Marschall

Nationale Genossenschaft
für die Lagerung
radioaktiver Abfälle

Hardstrasse 73
CH-5430 Wettingen
Telefon 056-437 11 11

www.nagra.ch

Arbeitsbericht NAB 13-83

**Gas related property distributions
in the proposed host rock
formations of the candidate siting
regions in Northern Switzerland
and in the Helvetic Zone**

December 2013

R. Senger¹, A. Papafotiou¹, P. Marschall²

¹Intera
²Nagra

KEYWORDS

Opalinus Clay, 'Brown Dogger', Effingen Member,
Helvetic Marls, gas transport, two phase flow,
gas transport mechanisms

Nationale Genossenschaft
für die Lagerung
radioaktiver Abfälle

Hardstrasse 73
CH-5430 Wettingen
Telefon 056-437 11 11

www.nagra.ch

Nagra Working Reports concern work in progress that may have had limited review. They are intended to provide rapid dissemination of information.

"Copyright © 2013 by Nagra, Wettingen (Switzerland) / All rights reserved.

All parts of this work are protected by copyright. Any utilisation outwith the remit of the copyright law is unlawful and liable to prosecution. This applies in particular to translations, storage and processing in electronic systems and programs, microfilms, reproductions, etc."

Zusammenfassung

Im Hinblick auf die provisorischen Sicherheitsanalysen für Etappe 2 des Sachplans wird untersucht, ob in den verfüllten Untertagebauwerken eines geologischen Tiefenlagers durch Korrosion sowie Materialdegradation und der damit verbundenen Gasbildung Gasdrücke entstehen können, die allenfalls die Barrierenwirkung des geologischen Tiefenlagers negativ beeinflussen könnten. Die Beurteilung dieser Frage erfordert ein genügendes Verständnis der Phänomene und Prozesse, die mit der Bildung, der Akkumulation und der Freisetzung der Gase verbunden sind. Mit Hilfe von numerischen Modellierungen kann der Gasdruckaufbau und die Gasfreisetzung nach Lagerverschluss untersucht werden für verschiedene Parameterwerte und Situationen für die Tiefenlager. Die Kenntnis der Gastransporteigenschaften der potenziellen Wirtgesteine in den vorgeschlagenen Standortgebieten bildet eine wichtige Voraussetzung für solche Modellanalysen. Zu den relevanten Gastransporteigenschaften zählen die Porosität, die intrinsische Permeabilität, die relative Permeabilität und die Kapillardruck-Sättigungsbeziehung der Wirtgesteine.

Im vorliegenden Bericht werden die für die Gasfreisetzung relevanten gasbezogenen Prozesse und Phänomene beschrieben und bewertet. Darüber hinaus werden für alle Wirtgesteinsformationen in den vorgeschlagenen Standortgebieten Referenzdatensätze für die gasbezogenen Wirtgesteinseigenschaften gegeben.

Table of Contents

Zusammenfassung.....	I
Table of Contents	III
List of Tables.....	V
List of Figures	VI
1 Introduction	1
1.1 Background and scope.....	1
1.2 Objectives	1
1.3 Geoscientific data base – status of knowledge	2
1.4 Report outline	3
2 Gas transport in clay-rich host rocks – Fundamentals	5
2.1 Rationale.....	5
2.2 Gas transport mechanisms: phenomena and conceptual models	5
2.2.1 Transport of gas dissolved in the porewater	7
2.2.2 Visco-capillary two-phase flow	9
2.2.3 Dilatancy-controlled gas flow.....	16
2.2.4 Gas flow along macroscopic tensile fractures	18
2.3 Modelling of gas transport processes in heterogeneous media.....	18
2.3.1 Basic modelling approaches	18
2.3.2 Gas transport in channel networks and fracture networks.....	19
2.3.3 Gas transport in porous media with stochastic property distributions.....	22
3 Gas-related properties of the potential host rocks.....	25
3.1 Relevant rock properties and constitutive relationships	25
3.2 Opalinus Clay	25
3.2.1 Basic geological characteristics of the Opalinus Clay formation	25
3.2.2 Gas-related characteristics of the Opalinus Clay	27
3.2.3 Reference parameters of the Opalinus Clay	35
3.3 'Brown Dogger'.....	39
3.3.1 Basic geological characteristics of the 'Brown Dogger'	39
3.3.2 Gas-related characteristics of the 'Brown Dogger'.....	41
3.3.3 Reference parameters.....	45
3.4 Effingen Member.....	47
3.4.1 Basic geological characteristics of the Effingen Member	47
3.4.2 Gas-related characteristics of the Effingen Member	49
3.4.3 Reference parameters.....	52
3.5 Helvetic Marls	54
3.5.1 Basic geological characteristics of the Helvetic Marls	54
3.5.2 Gas-related characteristics of the Helvetic Marls	55

3.5.3	Reference parameters.....	58
3.6	Evidence from elsewhere.....	60
3.6.1	Additional evidence for Opalinus Clay and similar rocks from the EURATOM 7 th Framework Project – FORGE (2010 – 2013).....	60
3.6.2	Complementary evidence from oil & gas industry.....	63
4	Summary and Conclusions	69
4.1	Phenomenology of gas transport in the proposed host rock formations.....	69
4.2	Reference parameters of the candidate host rock formations	71
5	References	73
A	Pore-space in 'Brown Dogger' and Opalinus Clay: homogeneity, percolation and RVE of porosity	A-1
B	Pore-space in "Effingen Member": homogeneity, percolation and RVE of porosity	B-1

List of Tables

Tab. 1-1:	Reference reports of particular relevance for the survey of gas transport parameters of the candidate host rock formations.	3
Tab. 2-1:	Solubilities and diffusion coefficients of a selection of gases in water at standard conditions (25°C, 1 atm) (Lide (ed) 2000).	9
Tab. 3-1:	Volume fractions of the different pore classes, determined by adsorption and desorption isotherms (H ₂ O, N ₂) after Nagra (2002). Complementary experimental evidence suggests that at least 20% of the total porewater can be attributed to the interlayer water.	27
Tab. 3-2:	Reference values for the gas-related parameters of the undisturbed Opalinus Clay for a shallow repository in Northern Switzerland (RV – reference value; AV – alternative value).	36
Tab. 3-3:	Reference values for the gas-related parameters of the undisturbed Opalinus Clay for a deep repository in Northern Switzerland (RV – reference value; AV – alternative value).	38
Tab. 3-4:	Reference values for the gas-related parameters of the clay-rich sequences of the 'Brown Dogger' in Northern Switzerland (RV – reference value; AV – alternative value).	46
Tab. 3-5:	Reference values for the gas-related parameters of the Effingen Member in the siting region JS in Northern Switzerland (RV – reference value; AV – alternative value).	53
Tab. 3-6:	Results of two-phase analysis of hydrotests and gas threshold pressure tests in the investigation boreholes Wellenberg.	56
Tab. 3-7:	Reference values for the gas-related parameters of the Helvetic Marls for a L/ILW repository at the Wellenberg siting area in Central Switzerland (RV – reference value; AV – alternative value).	59
Tab. A-1:	Mineral contents determined on the base of different methods.	A-2
Tab. B-1:	Overview of properties of FIB-nt data sets.	B-1

List of Figures

Fig. 2-1:	Classification and analysis of gas transport processes in ultra-low permeability rock such as the Opalinus Clay.....	6
Fig. 2-2:	Immiscible displacement in porous media from Lenormand et al. (1988): (a) Air displacing a viscous oil, (b+c) mercury displacing hexane, (d+e) glucose displacing oil at different C_a and $\log M$	10
Fig. 2-3:	Schematic representation of the three major flow regimes in the Ca-M-space from Lenormand et al. (1988): viscous fingering, capillary fingering and stable displacement.....	11
Fig. 2-4:	Compressibility on isotropic loading of samples with flow parallel and normal to bedding (left). Results of the water permeability tests on samples parallel and normal to bedding in terms of void ratio and hydraulic conductivity (right) (Romero et al. 2012).....	17
Fig. 2-5:	Stages of FIB-nt data processing of three rock samples recovered from the Mont Terri URL (BHG - left, BDR - middle and DR - right) from Keller et al. (2011): Pictures (a), (b) and (c) show the 3D reconstruction of the analyzed volume. Pictures (d), (e) and (f) present the 3D visualization of the segmented microstructure. The volume is separated into four categories: (i) pores (red), (ii) calcite (yellow), (iii) large mineral grains (gray) and (iv) matrix (transparent). Pictures (g), (h) and (i) display the 3D microstructure of the pore space. Note the strong preferred orientation of elongated pore objects in sample DR. The cubes in (h) and (i) indicate the orientation of the bedding plane.....	20
Fig. 2-6:	Characterisation of the water retention behaviour of fractured rock after Wettstein et al. (2011): (a) stochastic fracture network representation of the Helvetic Marls at the Wellenberg site after Nagra (1997). Colour coding of fractures reflects fracture transmissivities in relative units. (b) Invaded fractures at breakthrough marked from early to late invasion. (c) Invaded fractures after full invasion. (d) + (e) Invasion rate and derived capillary pressure-saturation relationship.....	21
Fig. 2-7:	Heterogeneous 2-D model for generic simulations of gas release from an SF/HLW repository in the Opalinus Clay: (a) Model domain and geostatistical distributions of permeability and porosity; (b) Spatial distribution of gas saturations at different times.....	24
Fig. 3-1:	Depth dependency of porosity measured in Opalinus Clay core samples recovered from different depths, from Mazurek (2011, 2013b), Ferrari et al. (2013) and Sarout et al (2013). Light colors denote core samples with exceptionally low clay content and/or high carbonates content.	26
Fig. 3-2:	Illustration of the mineralogy and structure of the Opalinus Clay at different scales, based on data from the Benken borehole in the ZNO siting area: (a) vertical profile of clay content determined by petrophysical logging, (b) core sample, (c) thin sections and (d+e) SEM images (after Nagra 2002).....	28

Fig. 3-3:	Equivalent pore size distributions of drillcore samples: (a) from Benken (sampling depth 614.82 m below ground) and Mont Terri (shaly facies), determined by mercury intrusion methods at Chevron's laboratories in Houston (by courtesy of Philip Mariotti); (b) from Schlattingen (sampling depth 880 m below ground), determined by mercury intrusion methods at EPFL (left) and UPC (right), that was complemented by BJH method.....	29
Fig. 3-4:	Capillary pressure measurements (water retention curves) by stepwise desaturation and resaturation in a desiccator (photo). The experiments were conducted by GRS (Zhang & Rothfuchs 2007) and UPC (Muñoz et al. 2003, Romero and Gomez 2013) and by EPFL (Ferrari and Laloui 2012).	31
Fig. 3-5:	Capillary pressure measurements (water retention curves) by stepwise desaturation and resaturation using a WP4c dew-point psychrometer and volumetric measurements using the Kerdane method on deep core samples from the Schlattingen borehole (Ferrari et al. 2013; Romero and Gomez 2013).	31
Fig. 3-6:	Capillary pressure measurements (water retention curves) by stepwise desaturation and resaturation using a WP4c dew-point psychrometer and volumetric measurements using the progressive method on a deep core sample from the Schlattingen borehole (Ferrari et al. 2013).	32
Fig. 3-7:	Gas injection experiments on core sample OED/Opalinus Clay (879.79 - 880.01 m) from the SLA-1 borehole with isostatic stress conditions and flow orthogonal to bedding (from Romero and Gomez 2013). Measured time evolution of pressures at the injection and outflow sides together with outflow volume and axial displacements at confining pressures of (a) $p = 15$ MPa and (b) $p = 19$ MPa.....	33
Fig. 3-8:	Simulated and measured pressures for air-pulse injection tests on core samples from Mont Terri ("shallow samples") for flow parallel (left) and perpendicular (right) to bedding after Senger et al. (2014).	35
Fig. 3-9:	Parametric models of capillary pressure and relative permeability k_r for water (w) and gas (g), representative for the shallow (undisturbed) Opalinus Clay formation in Northern Switzerland (reference parameter values RV and alternative values AV).	37
Fig. 3-10:	Parametric models of capillary pressure and relative permeability k_r for water (w) and gas (g), representative for the "deep" Opalinus Clay formation (reference parameter values RV and alternative values AV).	39
Fig. 3-11:	Depth dependency of porosity measured in 'Brown Dogger' core samples recovered from different depths (from Mazurek 2011, 2013, Ferrari et al 2013, and Sarout et al 2013). Light colors denote core samples with exceptionally low clay content and/or high carbonates content.	40
Fig. 3-12:	The 'Brown Dogger' in Schlattingen (after Bläsi et al. 2013): (a) Stratigraphy and rock mineralogical compositions indicate the correlation between carbonate-rich limestone facies (brown) and clay-rich facies (blue) alternating with sandy-calcareous marls (yellow); (b) photos of core samples, representing the main lithostratigraphic units in the 'Brown Dogger'; (c) SEM images with different magnification of a core sample from the Parkinsoni-Württembergica section (781.5 m bg) recovered from the Schlattingen SLA-1 borehole. The samples were polished with a Broad-Ion-Beam technique (BIB) perpendicular to bedding.	42

Fig. 3-13:	Equivalent pore size distributions (normalised) of drillcore samples from Schlattingen (sampling depth ranging from 766.7 to 807.4 m bg), determined by mercury intrusion methods at EPFL (left) and UPC (right), that was complemented by BJH method.....	43
Fig. 3-14:	Capillary pressure measurements (water retention curves) on a deep BD core samples from the Schlattingen borehole. Test are performed by stepwise desaturation and resaturation using a WP4c dew-point psychrometer and volumetric measurements (Ferrari et al. 2013; Romero and Gomez 2013): (a) using the Kerdane method; (b) using the progressive method for volume measurements.	43
Fig. 3-15:	Gas injection experiments on core sample OED 20/'Brown Dogger' (776.51 - 776.72 m) from the SLA-1 borehole with isostatic stress conditions and flow orthogonal to bedding (from Romero and Gomez 2013). Measured time evolution of pressures at the injection and outflow sides together with outflow volume and axial displacements at confining pressures of (a) $p = 15$ MPa and (b) $p = 19$ MPa.....	44
Fig. 3-16:	Parametric models of capillary pressure and relative permeability k_r for water (w) and gas (g), representative for the 'Brown Dogger' formation (reference parameter values RV and alternative values AV1 and AV2).	45
Fig. 3-17:	Clay mineral contents of the Wildegge-Formation based on geophysical logs (Deplazes et al. 2013) between Pfaffnau and Riniken.....	48
Fig. 3-18:	Property distributions and relevant scales in the Effingen Member: (a) Clay profiles, structural logs, fluid logging and packer testing in the Oftringen borehole; (b) brittle structures derived from core inspection; (c) microstructural investigations on core samples from the SLA-1 borehole.....	49
Fig. 3-19:	Microstructural analysis of the rock matrix of Effingen Member by FIB-nt: (a) 3D reconstruction of the analyzed volume ($1270 \mu\text{m}^3$); (b) 3D reconstruction of the framework of the non-clayey grains. Colors are label colors of individual grains; (c) 3D structure of the clay matrix; (d) 3D reconstruction of the pore space with pore radii > 20 nm.....	50
Fig. 3-20:	Normalised pore size distributions of core samples from the Effingen Member determined by mercury intrusion methods. The drillcores were recovered from the Oftringen borehole (Mazurek et al. 2013) and from the Schlattingen borehole (Ferrari et al. 2013).	51
Fig. 3-21:	Capillary pressure measurements (water retention curves) by stepwise desaturation and resaturation using a WP4c dew-point psychrometer and volumetric measurements using the progressive method on the deep Effingen Member core sample from the Schlattingen borehole measured by EPFL (Ferrari et al. 2013).	51
Fig. 3-22:	Parametric models of capillary pressure and relative permeability k_r for water (w) and gas (g), representative for the Effingen Member (reference parameter values RV and alternative values AV).	54
Fig. 3-23:	Wellenberg relationship between air-entry pressure (P_d) and intrinsic permeability.	56

Fig. 3-24:	The Wellenberg K-model: (a) Approach for the conversion of measured fracture transmissivities into effective hydraulic conductivities on the block scale ("T→K conversion") and (b) stochastic realisation of the K-distribution of the Helvetic Marls in the siting region Wellenberg (after Nagra 1997).	57
Fig. 3-25:	Helvetic marl: P_d -k-relationships based on Leverett and cubic scaling and comparison with the results of the in-situ tests (see Table 3-6, Fig. 3-23). The relationships are based on the results of the Invasion Percolation simulations by Wettstein et al. (2011), using a DFN model of the WLB site with an effective block conductivity of $1.6E-11$ m/s and an effective entry pressure of 40 kPa.	58
Fig. 3-26:	Parametric models of capillary pressure and relative permeability k_r for water (w) and gas (g), representative for the Helvetic Marls in the siting region Wellenberg (reference parameter values only; the gas entry pressure corresponds to an effective block permeability of $k_{mean} = 1E-20$ m ²).	60
Fig. 3-27:	Water retention measurements on core samples from Mont Terri (Villar and Romero 2012): (a) WRC along wetting/drying paths obtained under free volume conditions; van Genuchten curves are fitted to the different data sets. (b) WRC obtained under confinement (oedometric cell, 8 MPa vertical stress for samples from boreholes BHG-D1 and BHT-D1; constant volume conditions for samples BVE-1). The samples from borehole BVE-1 were subjected to drying paths applying total suction (for suctions above 3 MPa) or matric suction (for suctions below 3 MPa) while keeping their volume constant in the oedometer.	61
Fig. 3-28:	Long-term gas injection test on the rock samples from the Callovo Oxfordian (Harrington et al. 2012): Gas flow rates at the injection and backpressure filters during the gas injection test COx-1. The large spikes in injection flux relate to the compression of the gas phase during constant flow rate tests. The blue and green circles highlight hysteresis in the flow response.	63
Fig. 3-29:	Mesaverde Tight Gas Sandstones project (after Byrnes et al. 2009): (a) Air-mercury capillary pressure curves for selected samples ranging in permeability from 0.00025 mD to 2.24 mD (corresponding to $2.5E-19$ m ² – $2.24E-15$ m ²). The curves exhibit increasing threshold entry pressure and increasing "irreducible" wetting-phase saturation with decreasing permeability. (b) Example air-mercury successive drainage and imbibition capillary pressure curves.	64
Fig. 3-30:	Empirical threshold entry pressure – permeability relationships for various lithologies: (a) lithic sandstones (blue squares) and gas shales (open triangles) collected within the Mesaverde Tight Gas Sandstones project (from Byrnes et al. 2009). (b) wide range of undifferentiated lithologies, including shale, limestone and anhydrite, based on in situ measurements [from: Ibrahim et al. 1970; Ingram et al. 1997]. (c) shales, sandstones, anhydrites and carbonates in New Mexico (From: Davies [1991]).	67
Fig. 3-31:	Comparison of entry pressure – permeability relationships from different lithologies and different geological settings (Byrnes et al. 2009, Ingram et al. 1997, Davies et al. 1991 and Pusch et al. 2006).	68
Fig. A-1:	SEM images of 'Brown Dogger' BD-7 from the Schlattingen-1 borehole.	A-4
Fig. A-2:	SEM images of 'Brown Dogger' BD-7 from the Schlattingen-1 borehole.	A-5

Fig. A-3: 'Brown Dogger' BD-7 from the Schlattingen-1 borehole: (left) BSE images (scale bar see Fig. A-2c) that was segmented. (right) After image segmentation, the image shows the structure of major components at this microstructural level. A-6

Fig. A-4: 'Brown Dogger' BD-7 from the Schlattingen-1 borehole: A-6

Fig. A-5: Left column are BSE images of shale rocks with different clay contents. Bedding is vertical. Right columns are the corresponding segmented images. (HFW = horizontal field width). A-7

Fig. A-6: Reconstructed microstructures of major components. (a)-(f) sample OPA-3 and (g)-(l) sample BD-7. (a) and (g) are 3D reconstruction of the analyzed volume. (b)-(f) and (h)-(l) are microstructures corresponding to indicated components. A-8

Fig. A-7: Grain size distribution of (a) carbonates and (b) quartz grains. A-9

Fig. A-8: Local porosity distributions calculated for different length L of measuring cell and on the base of XCT data. a) OPA-3, b) Sample BD-7. A-10

Fig. A-9: Percolation probabilities of clay matrix. a) and b) along different directions and for a cell size L of 15 μm . c) and d) are bulk percolation probabilities calculated for different cell sizes L . Symbols are computed values and lines smooth interpolations. A-11

Fig. A-10: Bar plot shows a compilation of the calculated bulk percolation thresholds related to clay matrix of the. The values are grouped according to the applied scaling scheme (i.e. ϕ_{max} and ϕ_{av}). A-12

Fig. A-11: Mean value of clay content and intervals of confidence versus size of measuring cells L . (a) Sample OPA-3, (b) sample BD-7. A-12

Fig. A-12: Relative error ε_p vs. RVE of clay matrix for a single XCT realization. The plot gives an idea of the relative error on clay content that is related to a single XCT scan. As an example: for a sample with volume edge length of 200 μm the relative error on clay content is about 0.1 for sample OPA-3 and about 0.3 for sample BD-7. A-13

Fig. B-1: (a, c) BSE (back-scatter) and (b, d) LFD (large-field) images of a sample taken from the Effingerschichten. Images were made from BIB-polished surfaces. BSE images show phase contrast whereas the LFD detector was used to visualize the fine-grained clay grains between non-clayey grains (platy bright minerals between carbonates in b and d) (CC = carbonates, Qtz = quartz). The white rectangle marks the area which was imaged at higher resolution (c, d). The majority of the pores are within the fine-grained clay matrix are formed due to geometric incompatibilities between platy clay grains and more granular non-clayey grains. B-3

Fig. B-2: Stages of FIB-nt data processing. (First realization) a) 3D reconstruction of the analyzed volume based on BSE images. b) 3D reconstruction of the framework of the non-clayey grains. Colors are label colors of individual grains. Grains were separated using watershed separation. c) 3D structure of the clay matrix. d) 3D reconstruction of the pore space which is based on segmented SE images. The reconstructions reveal that a major part of the pore space is localized in the clay matrix. B-4

Fig. B-3: Stages of FIB-nt data processing. (Second realization) a) 3D reconstruction of the analyzed volume based on BSE images. b) 3D reconstruction of the framework of the non-clayey grains. Colors are label colors of individual grains. Grains were separated using watershed separation. c) 3D structure of the clay matrix. d) 3D reconstruction of the pore space which is based on segmented SE images. The reconstructions reveal that a major part of the pore space is localized in the clay matrix. B-5

Fig. B-4: (a) Grain size distribution of grains depicted in Figs B-2b and B-3b. b) Continuous pore size distributions of pores depicted in Figs B-2d and B-3d..... B-6

Fig. B-5: Local porosity distributions calculated for different length L of measuring cell. B-6

Fig. B-6: Percolation probabilities $\lambda_{\alpha}(\phi, L)$ along different directions. Symbols are computed values and lines smooth interpolations. a) x-direction, b) y-direction and c) z-direction. B-7

Fig. B-7: (a) ϕ_{\max} and b) ϕ_{av} vs. $L^{-1/\nu}$. Lines are least square fits of which intercept values are given in the plots and are considered as percolation thresholds. B-8

Fig. B-8: (a) Mean value of porosity and intervals of confidence versus size of measuring cells L . b) variances of porosities vs. volume of measuring cells. c) RVE of porosity vs. relative error ε_p for Effingen Member and Opalinus Clay..... B-9

1 Introduction

1.1 Background and scope

The selection of sites of geological repositories for the disposal of radioactive waste in Switzerland takes place within the Sectoral Plan for Deep Geological Repositories ("SGT") developed by the Swiss Federal Office of Energy (SFOE 2008). The Swiss waste management concept foresees separate repositories for low- and intermediate-level waste (L/ILW) and for high-level waste (HLW). In Stage 1 of the Sectoral Plan, Nagra proposed that six siting regions be considered for the disposal of L/ILW and that three regions (partially overlapping with those for L/ILW) be considered for the disposal of HLW (Nagra 2008). Four geologic formations were proposed for the disposal of L/ILW: Opalinus Clay, Effingen Member, 'Brown Dogger', and Helvetic Marls. The Opalinus Clay is the proposed host formation in all three siting regions for HLW disposal. It is the aim of Stage 2 to select and approve at least two siting regions for each repository type, followed by the selection of a site for each repository type and preparation of the application for the general licence in Stage 3.

As a decision basis for the second stage of the site-selection process, geological documents are to be elaborated for the authorities describing the relevant geological information in the six siting regions: Jura-Südfuss (JS), Jura Ost (JO), North of Lägern (NL), Zürich Nordost (ZNO), Südranden (SR), and Wellenberg (WLB). This includes, among other aspects, a compilation and evaluation of the existing data base on gas related properties, representative for all host rock formations in all siting regions.

This report summarises and integrates the lines of evidence which have proven beneficial for broadening the existing gas related data base of the candidate host rocks. Thus, new laboratory and field data have been gained within the EUP7/FORGE project (<http://www.bgs.ac.uk/forge/>). Furthermore, in collaboration with oil&gas industry, a joint industrial project has been initiated, aimed at characterising gas transport characteristics of shales (SHARC 2013). Last, but not least, comprehensive laboratory programmes were carried out in the context of recent field campaigns with emphasis on petrophysical characterisation of the candidate host rock formations in Northern Switzerland (e.g., Schlattingen-1, Gösgen, Oftringen). The results of the recent laboratory and field studies are compiled and evaluated in this report.

1.2 Objectives

Spatial distributions of gas related properties, such as porosity, intrinsic permeability, relative permeability and capillary pressure are a key input for modeling gas release from geological repositories in the candidate siting regions. For this, a comprehensive survey of the available field and laboratory data is needed. The integrated interpretation of the raw data calls for a traceable methodology. It is the purpose of the present report to:

- Provide a comprehensive survey of the existing hydrogeological data bases, needed for the inference of gas related property distributions of the host rock formations in the proposed siting regions.
- Set out a traceable workflow for an integrated interpretation methodology that provides representative gas transport parameter estimates from the existing mineralogical and hydrogeological data base.

- Apply the developed workflow on the available data from the different host rock formations for the derivation of conceptual flow models, rock-specific porosity-permeability-entry pressure relationships and, last but not least, for representative estimates of the gas transport parameter distributions and the corresponding parameter uncertainties.
- Provide gas related reference parameter sets for all host rock formations which can be used as input for modeling gas release scenarios.
- Compare the results with information from similar rock types investigated in site characterization programmes for deep geological disposal in Europe and in other geoscientific disciplines such as oil&gas exploration, CO₂ sequestration and mining industry.

1.3 Geoscientific data base – status of knowledge

Five of the six candidate siting regions, namely Jura Südfuss (JS), Jura Ost (JO), Nördlich Lägern (NL), Zürich Nordost (ZNO) and Südranden (SR), are situated in the Molasse Basin and the Tabular Jura of Northern Switzerland, respectively. The Wellenberg site is located in the Helvetic zone of the central Swiss Alps. This paragraph gives a brief survey of previous gas related studies and summarises recent activities initiated in the context of SGT – Stage 2.

As part of previous site investigation programmes, Nagra has spent comprehensive efforts in characterizing the gas transport behavior of the investigated host rock formations. The main data sources are can be linked to the following programmes and research platforms:

- *WLB*: a total 10 gas threshold pressure tests were conducted in the investigation boreholes SB2, SB3, SB4 and SB4a/v/s. A synopsis of all gas related studies within the WLB project are given in Nagra (1997).
- *OPA/Entsorgungsnachweis*: Characterisation of gas related properties of the Opalinus Clay by laboratory tests and Packer Test O7 (Nagra 2002).
- *Mont Terri URL*: A series of gas related laboratory and in-situ experiments were conducted (Marschall et al. 2005, Croisé et al. 2006)
- *EU-Projects*: Laboratory tests and field experiments performed in various URLs in argillaceous formations (NFPRO, FORGE)
- Complementary desk studies comprising evidence from elsewhere (CO₂, natural gas storage, reservoir engineering, shale gas)

In the context of Stage 2 of the Sectoral Plan, further gas related studies have been initiated as to complement the existing gas related data base of the candidate host rock formations (Nagra 2010, Marschall et al. 2013, SHARC 2013). Furthermore, Nagra participated in various drilling and logging campaigns in context of geothermal energy exploration in Northern Switzerland. Core samples from the different host rock formations were recovered and subjected to detailed mineralogical and geotechnical laboratory programmes. In several boreholes, it was possible to perform packer test campaigns in candidate host rock formations. Table 1-1 gives an overview of recent investigations which are of relevance for the present report.

Tab. 1-1: Reference reports of particular relevance for the survey of gas transport parameters of the candidate host rock formations.

Topic	Report
Hydraulic and physical rock properties	
Beauheim, R. (2013): Hydraulic conductivity and head distributions in the host rock formations of the proposed siting regions. Nagra Arb. Ber.	NAB 13-13
Sarout, J., Esteban, L., Josh, M. (2013): Laboratory Characterisation of Cores (Geothermal Well Schlattingen SLA-1, Switzerland): Petrophysics and rock mechanics / physics. Nagra Arb. Ber.	NAB 12-47
Jahns, E. (2012): Bohrung Gösgen KB-5A – Felsmechanische Untersuchungen an Kernen der Effinger Schichten. Nagra Arb. Ber. Nagra, Wettingen, Schweiz.	NAB 11-08
Mazurek, M. (2011): Aufbau und Auswertung der Gesteinsparameter-Datenbank für Opalinuston, den 'Braunen Dogger', Effinger Schichten und Mergel-Formationen des Helvetikums. Nagra Arbeitsbericht, Nagra, Wettingen, Schweiz.	NAB 11-20
Mazurek, M., Waber, H.N., Mäder, U.K., Gimmi, T., de Haller, A., Koroleva, M. (2013): Geochemical Synthesis for the Effingen Member in Boreholes at Oftringen, Gösgen and Küttigen. Nagra Tech. Ber.	NTB 12-07
Gas related rock properties	
Ferrari, A., Favero, V., Manca, D., Laloui, L. (2013): Geotechnical characterization of core samples from the geothermal well Schlattingen SLA-1. Nagra Arb. Ber., Nagra, Wettingen, Schweiz.	NAB 12-50
Romero, E., Gómez, R. (2013): Water and air permeability tests on deep core samples from Schlattingen SLA-1 borehole. Nagra Arb. Ber. NAB 13-51. Nagra, Wettingen, Switzerland.	NAB 13-51
SHARC (2013): Third Annual Report of the SHARC Consortium. Nagra Project Report. Nagra, Wettingen, Switzerland.	NPB 13-31
EUP7 -FORGE	
Marschall et al. (2013): FORGE D4-16: Gas transport processes at Mont Terri Test Site (EDZ and host rock)-Field results and conceptual understanding of self-sealing processes.	FORGE D4-16
Harrington (2013, ed): FORGE Milestone D4.24-R Summary report: Experiments and modelling of excavation damage zone (EDZ) behaviour in argillaceous and crystalline rocks (Work Package 4).	FORGE D4.24-R

1.4 Report outline

Chapter 1 describes scope and background of this report in the context of SGT – Stage 2 and details the objectives of the presented gas related analyses. A survey of relevant literature and brief report outline is given.

Chapter 2 presents an the fundamentals of gas transport in porous media, comprising gas transport mechanisms, parametric models of two phase flow and an overview of important coupled processes.

The integrated interpretation of the gas related laboratory and field data from the candidate host rock formations Effingen Member, 'Brown Dogger', Opalinus Clay and Helvetic Marls is described in Chapter 3. Gas related reference parameters are given in tabular form for each host rock.

Chapter 4 summarises the status of the knowledge on gas related properties of the candidate host rock formations in the proposed siting regions at the end of SGT – Stage 2.

2 Gas transport in clay-rich host rocks – Fundamentals

2.1 Rationale

The release of the gases produced in the backfilled disposal systems of the repository can occur by a variety of transport mechanisms. Gases will be dissolved in the pore water and eventually, when the solubility limit is exceeded, a separate phase will form and two phase flow may start. At elevated gas pressures the porous medium (host rock and backfill material, respectively) could undergo mechanical deformation, associated with significant impact on its flow and transport properties.

The prevailing gas transport mechanisms are controlled by the hydrodynamic properties of the fluids and by the environmental conditions, such as in-situ pore pressure, rock stress and water saturation in the porous medium. The microstructural and macroscopic characteristics of the porous medium are of special importance for the hydrodynamic properties, including the pore size distribution, the pore connectivity, spatial variability of porosity and the mineralogical composition of the solid phase (wettability). It is the purpose of this chapter to provide a systematic overview of the main gas transport processes, the gas-related parameters and the coupled processes which may be associated with the transport of the gas through the host rock formation (Opalinus Clay, Effingen Member, 'Brown Dogger', Helvetic Marls). Furthermore, the conceptual frameworks are presented for modelling gas transport processes in porous media. The chapter is structured as follows:

- Gas transport mechanisms in the porous rock matrix: the relevant gas transport mechanisms are specified, their characteristic features are discussed and the corresponding parameterization of transport mechanisms is given (Chapter 2.2).
- Modelling of gas transport processes in heterogeneous media (Chapter 2.3).

2.2 Gas transport mechanisms: phenomena and conceptual models

Gas transport through low-permeability rock formations is controlled not only by the hydraulic and mechanical properties of the rock mass (intrinsic permeability, porosity, rock strength), but also by the gas pressure at the location of gas entry and the hydromechanical state of the rock (i.e. water saturation, porewater pressure, stress state). Phenomenological considerations suggest the following subdivision of the basic transport mechanisms (Marschall et al. 2005; Figure 2-1):

- advective-diffusive transport of gas dissolved in the porewater
- visco-capillary two-phase flow
- dilatancy-controlled gas flow
- gas transport along macroscopic tensile fractures (hydro- and gas-fracturing)

The phenomenological description of flow and transport processes is related to the microstructural conceptualisation of the porous medium. In ultra-low permeability rock such as the Opalinus Clay, a network of connected pores in the range of micro- to nanometer defines the space, where flow of immiscible fluids can happen. Assuming that the skeleton of the solid rock matrix is subjected to elastic deformations only – in other words, the void volume of the pore network remains essentially constant - the flow of liquids and gases in the porous network can be described by well-known hydrodynamic approaches, such as (multiphase) flow in equivalent porous media and flow in channel/fracture networks, respectively.

The degree of complexity increases, when two-phase flow processes occur in a deformable porous medium. In this case the relevant state variables (i.e.; displacements, forces) of all three phases are interdependent (i.e.; coupled) and, as a consequence, the void volume of the pore network is not constant any more but is controlled by the state of deformation of the solid skeleton. In fracture mechanics terminology (e.g., Gross & Seelig 2007), irreversible deformation of the solid skeleton may be associated with ductile fracturing (sub-critical crack growth) or brittle fracturing (super-critical crack growth). Ductile fracturing is characterized by extensive plastic deformation before fracture initiation and slow fracture propagation, associated with absorption of a large amount of energy. In contrast, brittle fracturing is not associated with measurable plastic deformation before fracture initiation. The fracture propagates smoothly along the stress gradient and creates extended tensile cracks.

The different gas transport mechanisms are discussed in the following sections. A key issue in the quantitative description of two-phase flow processes is addressed in Chapter 2.3, dealing with the definition of a representative elementary volume of combined gas/water flow and with the up-scaling of two-phase flow parameters.

It is worth mentioning that different terminologies for the description of gas transport processes are found in the geoscientific literature. The term "capillary failure" is often used in oil & gas industry to describe the two-phase flow regime in cap rocks (e.g. Clayton & Hay 1994). "Membrane seal failure" describes gas transport through the pre-existing pore system of the caprock (i.e. advection / diffusion of dissolved gas and two-phase flow), whereas "hydraulic seal failure" is used to describe gas leakage due to hydro-mechanical processes in the seal (microfracturing, reopening of existing faults, hydro/gas fracturing). A comprehensive literature study on gas storage and gas transport phenomena is given in Evans (2008).

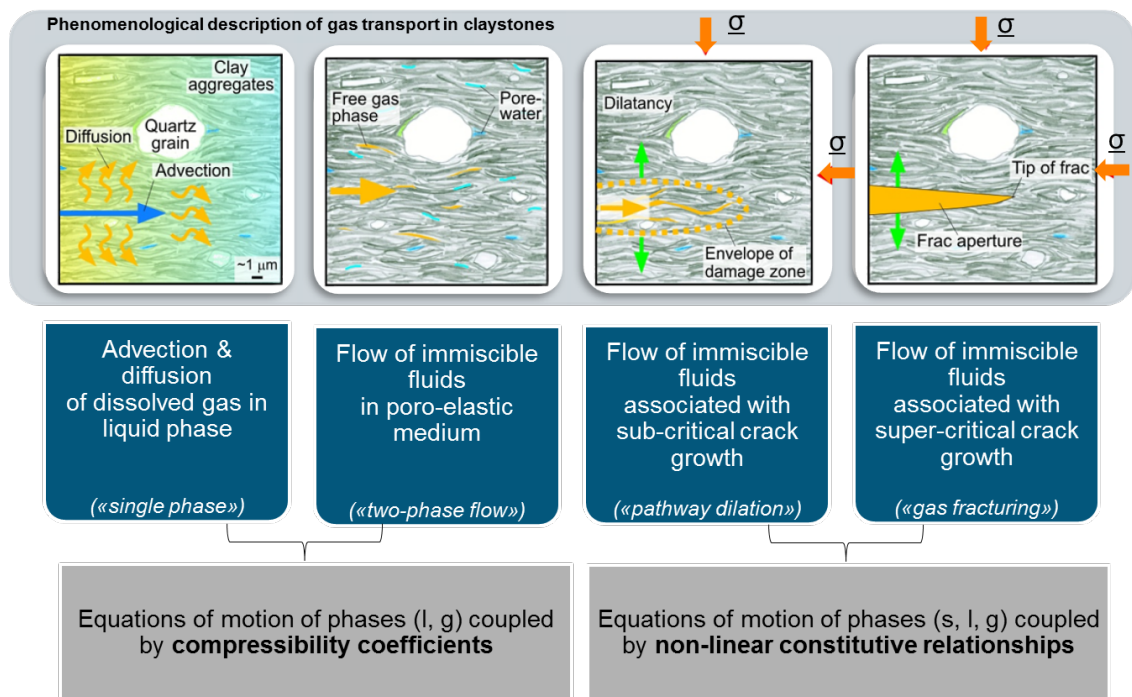


Fig. 2-1: Classification and analysis of gas transport processes in ultra-low permeability rock such as the Opalinus Clay.

2.2.1 Transport of gas dissolved in the porewater

Advective and diffusive transport of gas dissolved in porewater is characterised by three fundamental laws (Helmig 1997):

- Darcy's law, describing advective groundwater flow under the impact of pressure and gravitational forces
- Fick's law represents the diffusion of dissolved gas due to concentration gradients in the porewater
- Henry's law describes the solubility of gas in porewater

In this context, sorption of gas on clay has been identified as a possible retardation mechanism for dissolved gas transport or gas phase transport (Didier 2012). This mechanism is not considered in the present appraisal, because the sorption potential of the clay minerals decreases with increasing saturation of the rock. For the release of gases through the host rock formation, this retardation process is expected to be of very limited relevance.

Darcy's law represents the general basis for quantitative descriptions of groundwater flow. It denotes the linear correlation between the specific discharge v_f (Darcy velocity) through a representative elementary volume and the hydraulic gradient. The proportionality constant for the relationship is provided by the hydraulic conductivity K . Darcy's law is applicable only within certain limitations. For geomaterials with ultra-low permeability, such as the Opalinus Clay and bentonite, deviations from the linear flow law may be expected for low hydraulic gradients. The small pore radii cause electro-molecular rock-water interactions to gain significance in comparison to the viscous fluid properties, i.e. friction. In response, the formation water no longer behaves like a Newtonian fluid when exposed to a low hydraulic gradient. A comprehensive discussion of possible causes for non-linear porewater flow in clay-rich materials is found in Horseman et al. (1996). In empirical terms, this situation may be accounted for by introducing a hydraulic threshold gradient i_o (see, e.g. Bear 1972, de Marsily 1986). For the Opalinus Clay the threshold gradient necessary to establish Darcy flow was assessed by laboratory and in-situ experiments; the investigations indicated that Darcy's law holds for hydraulic gradients > 10 m/m (Marschall et al. 2004).

Diffusion is a process induced by the random thermal motion of molecules and ions. Diffusion in a porous medium in its simplest form can be described by Fick's law (Domenico and Schwartz 1990):

$$J = -D_d \text{grad}(C) \quad 2-1$$

with J being the diffusional flux (M/L^2T); D_d the effective diffusion coefficient (L^2/T) and C the concentration (M/L^3) of a species.

In this equation the flux of each species is related to the concentration gradient by a diffusion coefficient that is specific for that species. The value of the diffusion coefficient of a species in water depends on the type of species, the temperature and pressure and its interaction with other species (Felmy and Weare 1991). Diffusion coefficients for up to 30 species in a wide temperature and pressure range are given in Oelkers and Helgeson (1988). Table 2-1 gives the diffusion coefficients and solubility in free water for a selection of gases, which are relevant for the assessment of gas release.

In the case of diffusion in a porous medium, the diffusion rate is further defined by the structure and the properties of the porous medium such as the effective porosity, describing the total pore space available for the diffusion of the species and the tortuosity, accounting for the pore space geometry. Among various definitions, one of the most cited in Greenhorn and Kessler (1972) expressing D_d as a function of porosity and tortuosity (Greenhorn & Kessler 1972):

$$D_d = \frac{\phi \cdot d_w}{\left(\frac{L_e}{L}\right)} \quad 2-2$$

where Φ is the porosity, d_w is the diffusion coefficient in free solution, and the tortuosity is defined as the ratio of the length of a flow channel for a fluid particle, L_e , to the length of a porous medium sample, L . These parameters are to some extent also species dependent. It is clear that cations, anions and neutral species have unequal pore diffusion coefficients. The higher diffusivity of cations is generally attributed to surface diffusion (Cole et al. 2000) or to the diffuse double layer, where the concentrations of cations are increased (Bourg et al. 2003).

The diffusion coefficient for a two-phase system with porosity Φ is defined as (Pruess et al. 1999):

$$D_\beta^\kappa = \phi \cdot \tau_0 \cdot \tau_\beta \cdot d_\beta^\kappa \quad 2-3$$

where d_β^κ is the molecular diffusion coefficient for component κ in phase β , $\tau_0 \tau_\beta$ is the tortuosity which includes a porous medium-dependent factor τ_0 and a coefficient that depends on phase saturation S_β , $\tau_\beta = \tau_\beta(S_\beta)$. The diffusion coefficients for gases depend on pressure and temperature, as defined in Vargaftik (1975) and Walker et al. (1981). The saturation dependence of tortuosity can be described as functional relationships, such as that by Millington and Quirk (1961).

Gas dissolution and exsolution can transfer significant quantities of mass between the gas phase and the pore water in a porous medium. According to Henry's law the partial pressure of an ideal gas in the gas phase is proportional to the concentration of the gas in the aqueous phase (Domenico and Schwartz 1990):

$$K_H = \frac{(gas)_{aq}}{P_{gas}} \quad 2-4$$

Where K_H is the Henry's law constant (mol Pa^{-1}), P_{gas} is the partial pressure of the gas in the gas phase (Pa) and $(gas)_{aq}$ is the molar concentration of the gas in solution. Table 2-1 provides the solubilities of various gases in water.

This law is valid for ideal gases and very dilute pore waters only. In the case of real gases the fugacity should be taken into account instead of the partial pressure. The fugacity is a function of the temperature, the pressure and the composition of the gaseous phase. Equally, in the case of more realistic pore water compositions, activities should be used instead of concentrations. Activities are influenced by the pressure, the temperature and the composition of the solution

and are significantly lower than the equivalent concentrations in cases where pore waters consist of concentrated brines at higher temperatures and pressures (Kervevan et al. 2005).

The transport of dissolved gas occurs even at low (total) gas pressures; the pressure-dependent dissolution of gas in porewater and the increased groundwater flux cause the specific flux of the dissolved gas to increase with an increase in the gas pressure. The low hydraulic conductivity of argillaceous rock significantly restricts the efficiency of this transport mechanism. Thus, scoping calculations were conducted as part of the SF/HLW programme, indicating that the gas transport capacity of diffusion and advection (of dissolved gases) is several orders of magnitudes lower than the transport capacity of two-phase flow (Nagra 2004). Nevertheless, the general importance of diffusion and advection as slow background processes in all types of cap rock formations is beyond question and has been addressed in the context of many hydrocarbon exploration and reservoir engineering studies (Clayton & Hay 1994, Krooss et al. 1992, Schlömer & Krooss 1997).

Tab. 2-1: Solubilities and diffusion coefficients of a selection of gases in water at standard conditions (25°C, 1 atm) (Lide (ed) 2000).

Gas	Formula	Solubility (25°C, 1 atm) in mg l ⁻¹	Diffusion (25°C) x 10 ⁻⁹ m ² s ⁻¹
Hydrogen	H ₂	1.58	5.11
Helium	He	1.56	7.28
Oxygen	O ₂	40.76	2.42
Nitrogen	N ₂	18.41	2.00
Carbon dioxide	CO ₂	1503.52	1.91
Methane	CH ₄	22.74	1.84

2.2.2 Visco-capillary two-phase flow

Terminology and phenomenological aspects

Flow of immiscible fluids in porous media – often denoted as two-phase flow when the fluids are water and gas – has been the subject of extensive research in various disciplines of science and engineering, such as the oil & gas industry, CO₂ sequestration and environmental engineering. In its conventional form, visco-capillary two-phase flow is described as a transport process whereby porewater in the pore volume of a rock formation is displaced by gas under the influence of viscous and capillary forces (e.g. Bear 1972). This process is often called drainage, because the non-wetting fluid (gas) displaces a wetting fluid (pore water, "defending" fluid). The propagation of the gas front is controlled by the complex interaction of viscous forces, capillary forces and gravity. Many references of laboratory-scale experiments are found in the literature, with the aim to analyze and classify the governing processes of immiscible fluid flow in porous media (see for example Lenormand et al 1988, Méheust et al. 2002, Glass et al. 2001, Neuweiler et al. 2004; Marschall & Lunati 2006).

Lenormand et al. (1988) conducted two-phase flow experiments for a wide range of capillary numbers C_a and viscosity ratios M (Fig. 2-2):

$$C_a = \frac{\text{viscous forces}}{\text{capillary forces}} = \frac{\mu_{wf} \cdot v_f}{\sigma_{wf,nwf}}$$

$$M = \frac{\mu_{invading}}{\mu_{defending}} = \frac{\mu_{nwf}}{\mu_{wf}} \text{ or } \frac{\mu_{wf}}{\mu_{nwf}} \text{ (instable or stable displacement)}$$

2-5

μ_{wf} and μ_{nwf} representing the viscosities of the wetting and non-wetting fluid, v_f is the characteristic (Darcy) velocity in the medium and $\sigma_{wf,nwf}$ is the surface tension between the two fluids.

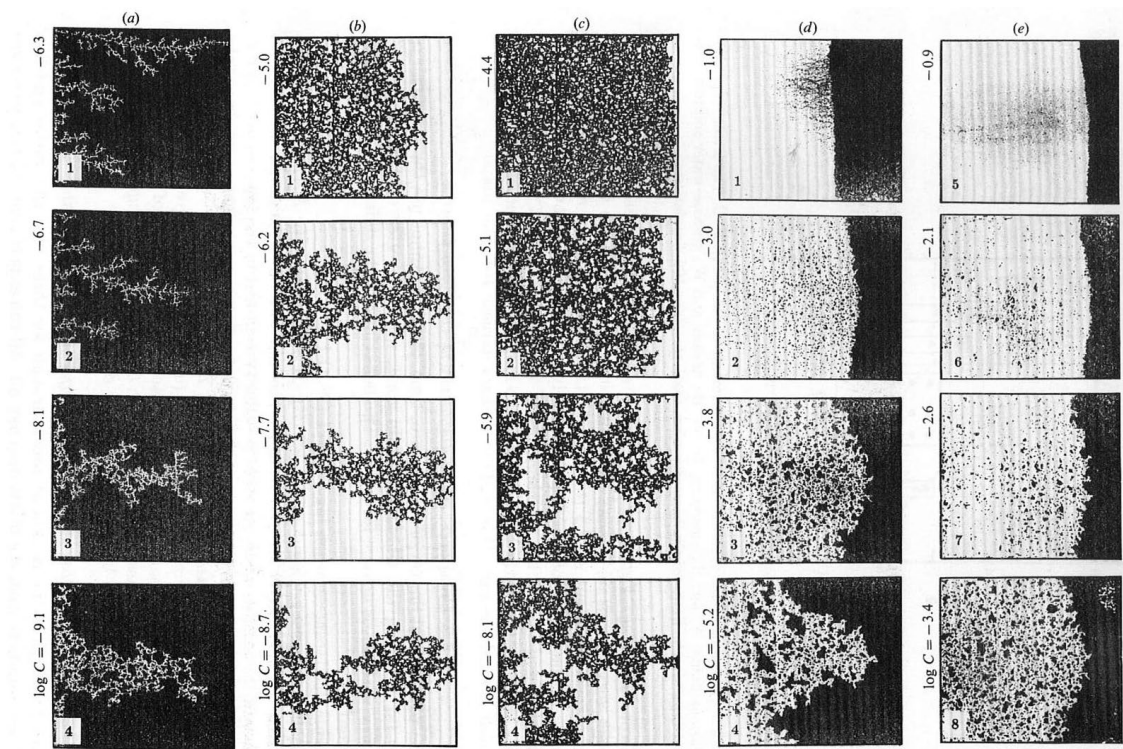


Fig. 2-2: Immiscible displacement in porous media from Lenormand et al. (1988): (a) Air displacing a viscous oil, (b+c) mercury displacing hexane, (d+e) glucose displacing oil at different C_a and $\log M$.

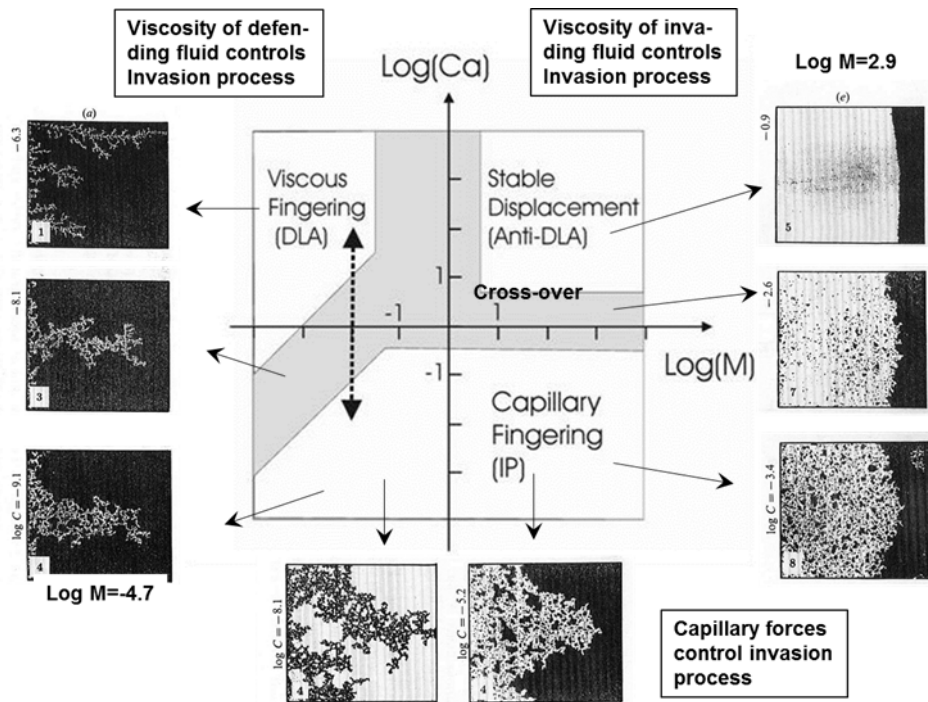


Fig. 2-3: Schematic representation of the three major flow regimes in the Ca-M-space from Lenormand et al. (1988): viscous fingering, capillary fingering and stable displacement.

Lenormand et al. (1988) identified 3 major flow regimes in the C_a -M-space, which they coined viscous fingering, capillary fingering and stable displacement (Fig. 2-3). The regime of stable displacement applies for the special case where the invading fluid has a higher viscosity than the defending fluid as for example water imbibition in a gas-filled porous medium (relevant for resaturation processes in the repository near-field). Viscous and capillary fingering are associated with instable displacement of a wetting fluid by the non-wetting fluid, giving rise to phenomena such as migration, fragmentation and coalescence of the non-wetting fluid (Wagner et al. 1997). When a gas front invades the initially saturated matrix of a low-permeability host rock, capillary fingering can be assumed as the prevailing regime ($\log M \approx -2$; $\log C_a < -10$).

Basic laws of fluid flow

The aforementioned phenomenological studies reveal that flow and transport of liquids and gases is controlled by the microscopic structure of the porous medium. For the following considerations, it is assumed that any type of pore network can be represented by basal elements with pipe-like (channel networks) or planar (fracture networks) shape.

Laminar flow of an incompressible fluid in a cylindrical pipe is described in fluid mechanics by the Hagen–Poiseuille equation:

$$q = F \cdot k \cdot \nabla P = \frac{\pi \cdot r^4}{8 \cdot \mu} \cdot \nabla P$$

where r is the pipe radius, F is the cross sectional area, k is the intrinsic permeability, ρ and μ are the density and viscosity of the fluid and P is the fluid pressure. Similarly, flow between two parallel plates expressed in terms of the cubic law:

$$q = T \cdot w \cdot \nabla P = \frac{a_h^3}{12 \cdot \mu} \cdot w \cdot \nabla P \quad 2-7$$

where T is the fracture transmissivity, a_h represents the distance between the two parallel plates and w is the trace length.

When gas enters an initially water saturated capillary tube, the Young-Laplace equation gives the relationship between the gas entry pressure (capillary threshold pressure) and the pore radius:

$$P_{ae} = \frac{2 \cdot \sigma_{gw}}{r} \cdot \cos \alpha \quad ; \quad P_{ae} = \frac{4 \cdot \sigma_{gw}}{a_h} \cdot \cos \alpha \quad 2-8a/b$$

where P_{ae} is the gas entry pressure, σ_{gw} is the surface tension gas/water (ca. 0.073 N m^{-1} at 20°C), r represents the radius of the capillary tube and α is the wetting angle. The corresponding equation 2-8b holds for the parallel plates, when the pore radius is exchanged by the half-width of the parallel plates.

Drawing on the aforementioned flow laws, pore scale modeling approaches are capable to describe multiphase flow processes in complex channel/fracture networks (see Chapter 2.3). Nevertheless, it is a great challenge to characterise the porescale variability of low permeability rocks such as Opalinus Clay in sufficient detail, required for an adequate numerical simulation of gas transport processes on the macroscopic scale. Therefore, alternative approaches have been developed. If the length scale of the considered flow processes is much larger than the scale of the microscopic variability, the flow may no longer depend on the details of the small-scale properties. It can then be described as a flow process in an equivalent homogeneous medium, where its medium properties capture the impact of the heterogeneities in an averaged sense. In the classical mixing theory of continuum mechanics of fluids (e.g.; Coussy 2004) the three phases (solid, wetting fluid, non-wetting fluid) are assumed to superimpose each other at a given location of the porous medium and the fluxes of the individual phases are described by the multiphase version of Darcy's law (linear fluid dissipation):

$$v_\beta = -k \frac{k_{r\beta} \rho_\beta}{\mu_\beta} (\nabla p_\beta - \rho_\beta \mathbf{g}) \quad 2-9$$

where v_β is the Darcy velocity (volume flux) in phase β , k is the intrinsic permeability, $k_{r\beta}$ is relative permeability to phase β , μ_β is viscosity, and $p_\beta = p + p_{c\beta}$ is the fluid pressure in phase β , p the pressure of a reference phase (in the TOUGH2 code usually the gas phase, Pruess et al. 1999) and the capillary pressure $p_{c\beta}$. The coefficient \mathbf{g} is the gravitational acceleration.

Here it is assumed that the rock mass behaves like an elastic medium, characterised by the porosity and the rock compressibility. The controlling factor for the two-phase flow characteristics of a porous medium is the gas entry pressure p_{ae} , also known as the capillary threshold pressure, which represents the difference between gas pressure and water pressure needed to displace the porewater from the initially fully saturated medium.

Once the gas entry pressure has been exceeded, the gas mobility is controlled mostly by the intrinsic permeability k of the formation, the permeability-saturation relationships (relative permeability), and the relationship between the capillary pressure and the water saturation (suction or water retention curve). The functional dependency between the pore space saturation and the relative permeability or the capillary pressure is commonly described with parametric models, such as that by van Genuchten (1980), describing the functional relationship between water saturation and capillary pressure, given as:

$$P_c = P_g - P_w = \frac{1}{\alpha} \cdot (S_e^{\frac{n}{n-1}} - 1)^{\frac{1}{n}} \quad 2-10$$

with

$$S_e = \frac{S_w - S_{wr}}{1 - S_{wr}}$$

or, alternatively:

$$S_e = [1 + (P_c/P_0)^n]^{-(1-1/n)} \quad 2-11$$

where P_c , P_g and P_w represent the capillary pressure, gas pressure and water pressure, respectively. $1/\alpha$, the inverse of van Genuchten's α parameter, is known as the capillary strength parameter P_0 or apparent gas entry pressure, and n is the shape factor (pore size distribution index). The degree of saturation S_w is the volume of porewater per volume of pores.

A related model which originated in the reservoir engineering literature is the Brooks-Corey model, where the capillary pressure as a function of saturation is given by:

$$P_c = P_d \cdot S_{e'}^{-1/\lambda} \quad 2-10a$$

with:

$$S_{e'} = \frac{S_w - S_{wr}}{1 - S_{wr}}$$

Where P_d is the capillary air-entry pressure, and the shape parameter λ is related to that in the van Genuchten model by:

$$\lambda = n - 1 \quad 2-11$$

As indicated in equation 2-4, the capillary pressure depends on the surface tension of water, which is a function of temperature. That is, for different temperatures, the effective capillary pressure can be specified by:

$$P'_c = P_c \cdot \frac{\sigma(t)}{\sigma_0} \quad 2-12$$

In the multiphase flow code TOUGH2 (Pruess et al. 1999), the functional relationship is given as:

$$P'_c = P_c \cdot \left[\frac{\sigma}{\sigma_0} - 0.0017 \cdot (T - T_0) \right] \quad 2-13$$

where σ is the surface tension at a given temperature T and σ_0 is the surface tension at a reference temperature T_0 .

The relative gas/water permeabilities $k_{r,g}$ and $k_{r,w}$ of the Opalinus Clay can be derived by integration of the capillary pressure curve following the the approach of Mualem (e.g. Helmig 1997):

$$k_{r,g} = (1 - S_e)^\varepsilon \cdot (1 - S_e^{\frac{n}{1-n}})^{2(1-1/n)} \quad 2-14$$

$$k_{r,w} = S_e^\gamma \cdot \left[1 - (1 - S_e^{\frac{n}{1-n}})^{\frac{n-1}{n}} \right]^2 \quad 2-15$$

with
$$S_e = \frac{S_w - S_{wr}}{1 - S_{wr}}$$

where ε and γ are empirical shape factors, describing the pore connectivity of the medium which are typically set to $\varepsilon = 1/2$ and $\gamma = 1/3$ (Luckner et al. 1989). With the Mualem approach, relative permeability and capillary pressure are theoretically linked by the shape factor n , which occurs in both equations and is typically determined by the water retention curve.

In the Brooks-Corey model, the relative permeabilities are defined as:

$$k_{r,g} = (1 - S_e)^2 \cdot (1 - S_e^{\frac{2+\lambda}{\lambda}}) \quad 2-14a$$

$$k_{r,w} = S_e^{\frac{2+3\lambda}{\lambda}} \quad 2-15a$$

with
$$S_e = \frac{S_w - S_{wr}}{1 - S_{gr} - S_{wr}}$$

An excellent review of the spectrum relative permeability models in multiphase flow analysis is given in Honarpour et al. (1986).

Enhancement (or reduction) of the gas mobility, as postulated in Croisé et al. (2006) for the interpretation of in-situ gas injection tests at the Mont Terri underground laboratory, can be taken into account by introducing a multiplication factor f_g in the relative permeability equation, for example for the van Genuchten model, as follows:

$$k_{r,g} = f_g (1 - S_e)^\varepsilon \cdot (1 - S_e^{\frac{n}{1-n}})^{2(1-1/n)} \quad 2-16$$

In this study a gas enhancement factor $f_g = 1$ was used for all two-phase flow simulations.

Alternatively, the enhanced gas mobility is described by the Grant model (Grant 1977), whereby the relative permeability of the gas phase is given by:

$$k_{r,g} = 1 - k_{r,l} \quad 2-17$$

whereby the gas and liquid phases tend to move independently of each other, which is typical for fracture-porous rocks where liquid tend to migrate primarily through the matrix due to higher capillary pressures, and gas migrates through the higher-permeable fractures characterized by lower capillary pressures.

A distinct hysteresis is often seen in the capillary pressure relationship, depending on the saturation path, i.e. whether the relationship corresponds to a saturation or desaturation of the porous medium. During the saturation process, the porosity of the medium cannot be saturated completely (residual gas saturation S_{gr}), because part of the pore space is poorly connected. On the other hand, assuming an initially fully saturated medium, a critical gas saturation has to be exceeded before gas starts to form a continuous phase with a gas permeability > 0 (e.g. Dury et al. 1999). In the context of this study, due to the limited experimental data base, no distinction is made between residual and critical gas saturation.

The dependency of capillary pressure on the history of flow is known as the aforementioned capillary pressure hysteresis. The dependence of capillary pressure (and of the relative permeability relationship) on the rate of change of saturation is termed in literature as "dynamic effect" or "non-equilibrium effect". A multitude of references on the dynamic effect are found in the literature (Barenblatt et al. 1990, Hassanizadeh et al. 2002; Silin & Patzek 2003; Schembre & Kavscek 2006, Juanes et al. 2006), however, the interpretation of the effect is controversial. Thus, Hassanizadeh et al. (2002) explain the non-equilibrium phenomena as a characteristic feature in the context of their new macroscopic theories of multiphase flow (Hassanizadeh and Gray 1990), whereas Bourgeat & Panfilov (1998) interpret it as consequence of upscaling of two-phase flow parameters. In the present report, the dynamic effect is not considered due to the lack of experimental evidence for ultra-low permeability rock, such as Opalinus Clay.

Juanes et al. (2006) investigate hysteresis effects in the relative permeability – saturation relationship as part of a modelling study on CO₂ sequestration. Drawing on experimental evidence, the authors demonstrate by an analysis of pore-scale processes that relative permeabilities are not single functions of fluid saturations ("dynamic effects") and that they display strong hysteresis effects. Permeability hysteresis could be of great importance for the

gas release from nuclear waste repositories, because the rock zone around the underground structures is desaturated during the operational phase of the repository. After repository closure, trapped gas in the vicinity of the backfilled tunnels could lower the gas entry pressure of the rock and thus increase its gas transport capacity in the early post-closure period.

2.2.3 Dilatancy-controlled gas flow

Dilatancy-controlled gas flow (or "pathway dilation"; terminology after Horseman et al. 1996) is a transport mechanism of special importance for argillaceous media with low tensile strength. Clay-rich rock cannot withstand long-term gas pressures with a magnitude greater than the minimum principal stress acting on the rock mass. Due to the expected micro-scale variability of the geomechanical rock properties, it is even plausible that microfractures will form before yielding (ductile fracturing). Ductile fractures propagate slowly, the fracture surface is rough and the damage zone around the fracture tip grows with increasing distance to the locus of initiation (e.g., Gross & Seelig 2007). The process of gas-driven microfracturing leads to an increase of the void space, which is accompanied by a detectable increase in intrinsic permeability and a change in the capillary pressure-saturation relationship. In the terminology of multiphase flow concepts, gas flow is still controlled by visco-capillary forces (phase interaction between wetting and non-wetting fluid) - the main difference with respect to conventional two-phase flow is that the transport properties of the solid phase (rock permeability, relative permeability, capillary pressure relationship) can no longer be viewed as invariants since they depend on the state of deformation of the rock.

Olivella and Alonso (2008) developed a hybrid formulation of pathway dilation, expressing the effective permeability of the rock as the superposition of an intrinsic matrix permeability and a stress dependent fracture transmissivity ("embedded fracture approach"). The approach was tested successfully for soft clays (bentonite) and for claystone. An even simpler approach has been introduced by Senger et al. (2008), using a pressure dependent permeability multiplier:

$$k = k_0 \left[1 + (k_{\text{factor}} - 1) \frac{(P - P_1)}{(P_2 - P_1)} \right] \quad 2-18$$

where k_0 is the reference permeability, k_{factor} is a scaling factor, P_1 is the characteristic pressure for the on-set of dilation, and P_2 is maximum pressure corresponding to the maximum permeability. The relationship between capillary strength and permeability is typically represented by Leverett's function as (provided the porosity changes are considered negligible compared to the permeability changes):

$$P_c = P_0 \sqrt{\frac{k_0}{k}} \quad 2-19$$

or by a cubic-law function:

$$P_c = P_0 \sqrt[3]{\frac{k_0}{k}} \quad 2-20$$

This simplified approach has been applied successfully for the interpretation of gas injection tests in the HG-D experiment at Mont Terri (Marschall et al. 2013).

Romero and Gomez (2013) performed water and gas permeability tests in a triaxial cell on Opalinus Clay samples from Mont Terri and Schlattingen, as well as for 'Brauner Dogger' samples from Schlattingen (see also Chapter 3.2 and 3.3). A stress dependent porosity (resp. void ratio) and permeability was identified in water injection tests under steep gradients (Fig. 2-4). Fast gas injection tests caused deformation of the clay due to the decrease in effective stresses resulting in a change in "storativity" and resulting change in porosity. The change in porosity and associated change in permeability could be described as log-linear relationships of measured permeability and void ratios of core samples under different stress conditions. This behaviour represented a largely reversible elastic deformation, expressed by the bulk compressibility of the claystone as derived from isotropic compression tests. The analyses of air-injection tests demonstrated the importance of incorporating the coupled processes associated with the elastic behaviour of the claystone in terms of the stress-induced changes in porosity, permeability and capillary pressures on the local scale (Senger et al. 2014). Further experimental evidence of hydro-mechanical coupling is given in Chapter 3.

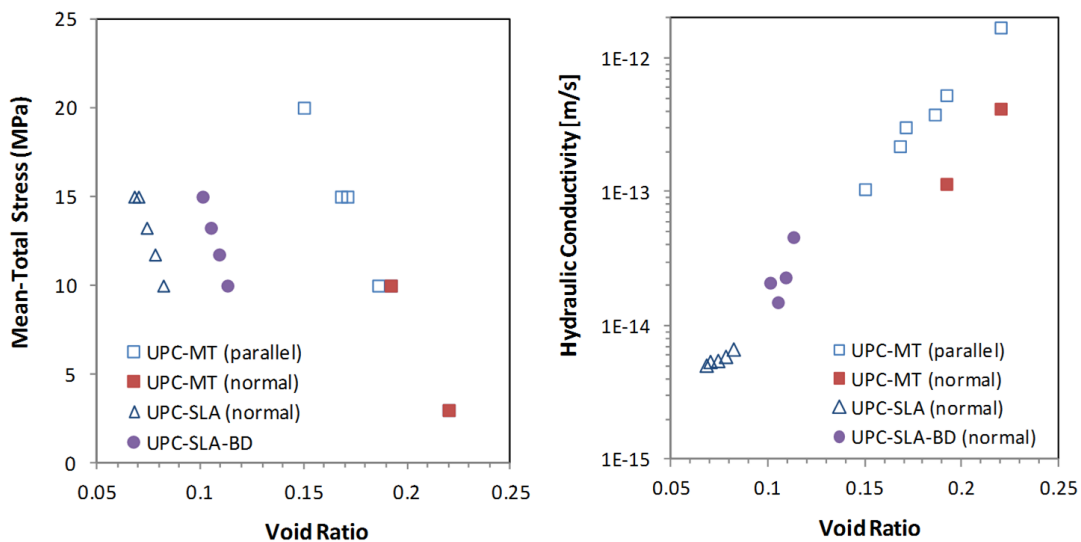


Fig. 2-4: Compressibility on isotropic loading of samples with flow parallel and normal to bedding (left). Results of the water permeability tests on samples parallel and normal to bedding in terms of void ratio and hydraulic conductivity (right) (Romero et al. 2012).

Empirical investigations and phenomenological descriptions of dilatancy-controlled gas flow through clay-rich seals were the subject of many geoscientific papers in the field of reservoir engineering (e.g. Clayton & Hay 1994, Ingram et al. 1997, Ingram & Urai 1999, Zweigel et al. 2004). Further evidence for pathway dilation phenomena has been found in other areas such as natural gas storage and CO₂ sequestration. Benson et al. (2002) reviewed the safety results of underground storage in the United States as part of a comprehensive study considering CO₂ storage in deep geological formations. The authors emphasise the importance of vertical pressure gradients as an indicator for the onset of dilatancy-controlled leakage through the caprocks which cover natural gas storage formations. According to Ibrahim et al. (1970) the critical pressure gradient for dilatancy-controlled gas leakage is bracketed by the hydrostatic gradient (≈ 9.8 kPa/m) and the lithostatic gradient (≈ 22.6 kPa/m assuming a bulk density of the overburden of about 2.3 g/cm³), where the lithostatic pressure gradient represents a lower limit for the initiation of macroscopic fractures (cf. Chapter 2.2.4). It is noteworthy that the

CSA Standard Z341 (CSA 2005) includes a recommendation that the maximum operating pressure of natural gas storage systems should not exceed 80% of the fracture pressure of the caprock formation in order to minimise the leakage rates. In the absence of local fracture pressure data, a fracture gradient of 18.1 kPa/m is assumed, which leads to the maximum pressure gradient of 14.5 kPa/m (i.e. 80% of the fracture gradient). Further references with a collection of case studies on critical pressure gradients in the field of reservoir engineering are found in Evans (2008).

An important feature of the deformation behaviour of argillaceous materials is their self-sealing capacity (e.g. Nagra 2002). Permeability enhancement at elevated gas pressures tends not to be permanent; when the gas pressure is reduced the material reconsolidates and the hydraulic and mechanical properties of the porous medium approach the values which are characteristic for the undisturbed stress state.

2.2.4 Gas flow along macroscopic tensile fractures

As a rule of thumb, a macroscopic tensile fracture (hydrofrac / gasfrac) develops when the gas pressure is larger than the sum of the minimum principal stress and the tensile strength of the rock (e.g. Valko & Economides 1997). The brittle fracture is initiated quasi-instantaneously without precursory plastic deformation and propagates at about the velocity of a shear wave (e.g., Gross & Seelig 2007). Gas flow in such a macroscopic tensile fracture can be seen as a single-phase flow process. The propagation comes to a halt when the gas pressure in the fracture becomes less than the value of the minimum principal stress (shut-in pressure). Large-size hydrofracs are characterised by a fracture transmissivity which increases the bulk permeability of the rock by many orders of magnitude. In a rock with low tensile strength, a macroscopic fracture develops only when the gas pressure build-up is rapid, i.e. when the combined effect of porewater displacement and formation of small-scale fractures (i.e. dilatancy) no longer counterbalances the gas production rate.

The conceptual, theoretical and experimental framework for fracture propagation is well documented in standard hydrocarbon exploration literature (e.g. Valko & Economides 1997).

2.3 Modelling of gas transport processes in heterogeneous media

2.3.1 Basic modelling approaches

For any of the aforementioned mechanisms, gas transport is controlled by the microscopic structure of the porous medium. Sub-scale variability of the void space may have a distinct impact on transport processes at scales, which exceed by orders of magnitudes the characteristic length of the heterogeneities. In the assessment of gas release from a geological repository, scale issues are faced not only for gas paths through the intact rock matrix, but also when gas release takes place in fracture networks (fractured host rocks such as the Helvetic Marls and the Effingen Member; gas transport along the excavation damaged zone around the backfilled underground structures).

The modelling concepts reported in the scientific literature for the simulation of two-phase flow processes in porous media are based on two different fundamental approaches:

- *Discrete pore network models (channel networks or fracture networks)* represent the porous medium as a network of connected channels. At a given location, a channel is occupied either by the wetting or by the non-wetting fluid. Flow in the channels occurs by piston-like

displacement as a result of the pressure difference between the phases and the fluid displacement is simulated by simplified invasion percolation (IP) algorithms. Frequently, stochastic approaches are adopted to describe the geostatistical properties of the porous medium at the pore scale. Such stochastic discrete network models have been applied successfully for the simulation of two-phase flow processes in the regime of capillary fingering (Glass & Yarrington 2003, Lenormand & Zircon 1989). The main challenge is the realistic geostatistical description of the pore network in a stochastic framework, which requires comprehensive microstructural databases for the model identification and conditioning process.

- *Equivalent porous medium models* are based on the classical mixing theory of continuum mechanics of fluids (e.g. Coussy 2004). In this concept, the three phases (solid, wetting fluid, non-wetting fluid) are assumed to superimpose each other at a given location of the porous medium. Basic physical principles, such as mass and momentum balance and the laws of thermodynamics apply for each phase and for all types of energy transformation in the system. The phases are described in terms of continuous density functions, implying that a representative elementary volume exists, which is relevant at the macroscopic scale for all the physical phenomena involved in the intended application. On the macroscopic scale, phase couplings are expressed in terms of capillary pressure and relative permeability-saturation relationships. Numerous scientific papers have been published in the recent years, aimed at assessing the range of validity of the continuum models of two-phase flow (Artus & Noetinger 2004, Jacobs & Gelhar 2005, Stauffer et al. 2009, Neuweiler et al. 2010).

2.3.2 Gas transport in channel networks and fracture networks

Claystones exhibit low permeability, low porosity and a pore size distribution, which consists mainly of micropores (< 2nm) and mesopores (2 – 50 nm). The low permeability is associated with low capillary numbers, suggesting that gas transport occurs in the regime of capillary fingering. The displacement of porewater by a gas phase is mainly restricted to the sparse network of macropores (> 20 nm), because the micro- and mesopores are hardly invaded by the gas phase due to their high capillary entry pressure. The poor connectedness of the network of macro-pores raises the issues of the appropriate averaging volume ("representative elementary volume") and, as a consequence, of the transferability of the equation of motion from a local (pore) scale to a global scale formulation, which can be expressed in terms of macroscopic "effective" two-phase flow properties of the equivalent porous medium.

Valuable insight addressing the issue of spatial continuity of the pore structure can be gained by high resolution 3-D imaging techniques such as Transmission Electron Microscopy (TEM), Focussed Ion Beam nano-tomography (FIB nT) and Micro-CT (Keller et al. 2010, 2013a).

Keller et al. (2013b) performed geostatistical analyses on Opalinus Clay samples (Fig. 2-5), which had been subjected to comprehensive microstructural characterisations (TEM, FIB-nt, SEM) at scales ranging between 5 nm and 500 µm. Local porosity distributions and directional percolation probabilities were inferred, drawing on the conceptual framework of local porosity theory (Biswal et al. 1998). Keller et al. concluded that the porosity of the Opalinus Clay samples homogenizes at sample sizes < (10 µm)³, which defines the order of magnitude of the REV (Representative Elementary Volume). Percolation probability of the Opalinus Clay samples displayed a marked variability and a distinct anisotropy, indicating enhanced connectivity parallel to bedding. Connectivity perpendicular to bedding was generally poor. However, the analysed data base was yet too small for a reliable geostatistical interpretation of the directional percolation probability.

In fractured rock such as the Helvetic Marls and the Effingen Member, gas transport is essentially restricted to the porosity associated with the fracture systems, whereas the pore space of the intact rock matrix is not accessible for gas. The complexity of the fracture systems in terms of geometry and hydraulic characteristics prevents deterministic approaches and favors stochastic representations of the fracture systems. In the context of the Wellenberg programme (Nagra 1997), a stochastic fracture network model of the Helvetic Marls at the Wellenberg site was elaborated. The model was conditioned with logging data and packer test results from the site investigation programme and served as a tool for converting fracture transmissivities at the scale of the borehole investigations into effective hydraulic conductivity values on the block scale with typical block sizes $\geq (50 \text{ m})^3$. Eventually, the block conductivities fed in a stochastic groundwater flow model for simulating pore water flow on the repository scale.

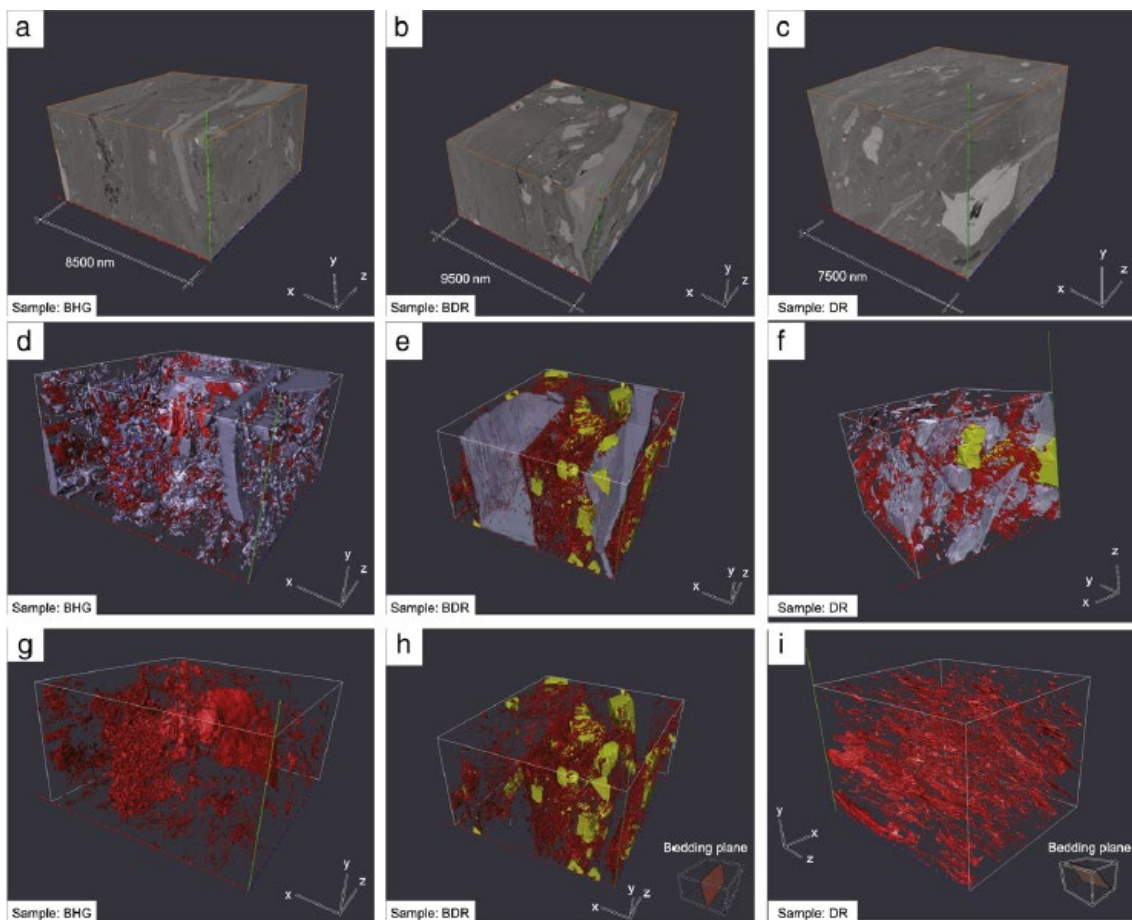


Fig. 2-5: Stages of FIB-nt data processing of three rock samples recovered from the Mont Terri URL (BHG - left, BDR - middle and DR - right) from Keller et al. (2011): Pictures (a), (b) and (c) show the 3D reconstruction of the analyzed volume. Pictures (d), (e) and (f) present the 3D visualization of the segmented microstructure. The volume is separated into four categories: (i) pores (red), (ii) calcite (yellow), (iii) large mineral grains (gray) and (iv) matrix (transparent). Pictures (g), (h) and (i) display the 3D microstructure of the pore space. Note the strong preferred orientation of elongated pore objects in sample DR. The cubes in (h) and (i) indicate the orientation of the bedding plane.

Wettstein et al. (2011) made use of the aforementioned stochastic fracture network model (Fig. 2-6) for the derivation of a representative water retention behavior of the Helvetic Marls as input for repository scale modeling of gas release at the Wellenberg site. They adopted an Invasion-Percolation algorithm (IP) for invading the fracture network with a non-wetting fluid. Fluid invasion was controlled by the gas entry pressure of the individual fractures, derived from fracture transmissivity according to equations 2-7 and 2-8:

$$P_{ae} = 4 \cdot \sigma_{gw} \cdot (12\mu T)^{-1/3} \cdot \cos \alpha \quad 2-21$$

Multiple stochastic realisations of WLB fracture network model were subjected to the IP analysis by stepwise increase of the fluid pressure and determination of the corresponding fluid volume. Thus pressure-saturation curves were derived for each stochastic realization of the fracture network. Finally, the ensemble average of the derived pressure-saturation curves was calculated, representing the effective water retention curve of the Helvetic Marls at the block scale (Fig. 2-6).

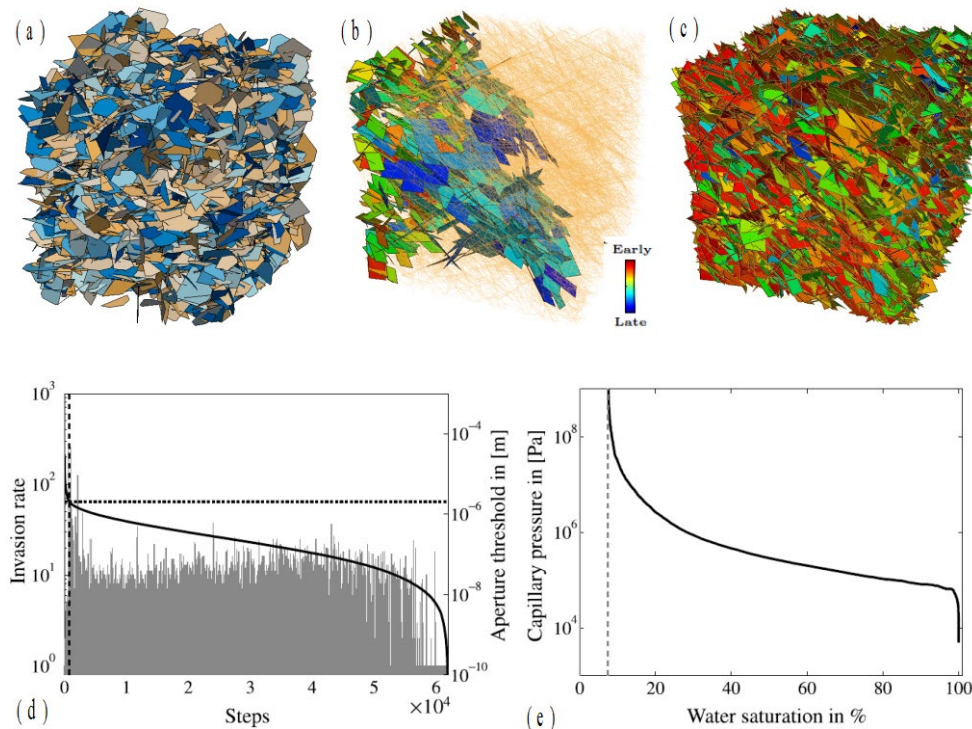


Fig. 2-6: Characterisation of the water retention behaviour of fractured rock after Wettstein et al. (2011): (a) stochastic fracture network representation of the Helvetic Marls at the Wellenberg site after Nagra (1997). Colour coding of fractures reflects fracture transmissivities in relative units. (b) Invaded fractures at breakthrough marked from early to late invasion. (c) Invaded fractures after full invasion. (d) + (e) Invasion rate and derived capillary pressure-saturation relationship.

The stochastic realizations of the discrete fracture network (DFN, Fig. 2-6a) were transformed into equivalent representations of a continuous porous medium (CPM), following basically the approach of the so-called Wellenberg K-model (Nagra 1997). Equivalent properties of CPM elements were calculated from each DFN realization using the upscaling method of Jackson et al. (2000), which is implemented in the CONNECTFLOW code (Hartley & Holton 2004). This method calculates the equivalent permeability tensor for sub-regions of the DFN by fitting to the flow (as calculated in the DFN model) across the sub-region for different hydraulic gradients. In the current application, an equivalent tensor has been calculated for each cell in the CPM model. The CONNECTFLOW CPM representation was converted into a TOUGH2 model as described in Lanyon & Senger (2011).

2.3.3 Gas transport in porous media with stochastic property distributions

In the regime of capillary fingering, the spatial variability of porosity and permeability has a strong impact on the invasion of the non-wetting fluid (see Chapter 2.2.2). Gas release from the backfilled repository structures through the host rock with typical capillary numbers $\log C_a < -10$ and a mobility ratio $\log M \approx -2$ takes place in the regime of capillary fingering. Therefore, the impact of spatial variability of the rock properties has to be addressed when gas transport processes are simulated in the host rock around the repository.

Papafotiou et al. (2011) conducted generic modeling studies, aimed at quantifying the impact of spatial variability of rock properties on gas release through the host rock on a deca- to hectometer scale (Fig. 2-7). For this purpose, generic 2-D models were elaborated, representing (i) a L/ILW emplacement cavern embedded in a sequence of limestones and marls with distinct lithological variability (Effingen Beds) and (ii) a SF/HLW emplacement tunnel in a claystone of moderate spatial variability (Opalinus Clay). Gas transport processes in the geosphere were simulated with a composite structural model of the host rock formation, comprising stochastic representations of the fracture systems and the facies distributions, respectively. The fracture model accounted for the flow processes in the discrete water conducting features of the host rock, while the facies model was dedicated to porewater flow in the porous matrix of the intact rock.

The facies model displayed spatial variations in clay content, porosity and permeability within the different facies. Representative distributions of clay content and porosity of the intact rock matrix were derived by the analysis of experimental variograms (clay logs, petrophysical tests on core samples). Matrix permeability was inferred from the measured clay content and porosity by the empirical relationships (Kozeny-Carman and Yang-Aplin relationship, respectively).

The Kozeny-Carman relationship is a well-established semi-empirical permeability indicator for porous materials. Even though the relationship was initially developed for high-porosity granular materials, it is adopted frequently for inferring the hydraulic conductivity of low-porosity rocks such as mudstones, shales and claystones (Horseman et al. 1996; Dewhurst 1999):

$$K = \frac{\phi^3}{(1-\phi)^2} \cdot \frac{\rho_w \cdot g}{\tau^2 \cdot (\rho_s \cdot S) \cdot C_s \cdot \eta_w}$$

where ρ_s , ρ_w and η_w are grain density, fluid density and fluid viscosity. ϕ is the porosity, S is the specific surface, τ is a tortuosity factor (usually: $\tau = \sqrt{2}$ in the absence of independent experimental evidence) and C_s is a shape factor, ranging between $C_s = 2$ (circular cross-section capillary) and $C_s = 3$ (parallel plate flow). Olson (1962) assumed $C_s = 2.5$ for the pore channels of a saturated clay-rich medium.

More recently, Yang & Aplin (2010) proposed an empirical relationship for the hydraulic conductivity of shales:

$$K = \frac{\rho_w g}{\mu} \exp(b)$$

$$b = -69.59 - 26.79 f_{clay} + 44.07 f_{clay}^{0.5} +$$

$$(-53.61 - 80.03 f_{clay} + 132.78 f_{clay}^{0.5})e +$$

$$(86.61 + 81.91 f_{clay} - 136.61 f_{clay}^{0.5})e^{0.5}$$
2-23

where f_{clay} is the clay fraction and e represents the void ratio: $e = \phi/(1-\phi)$.

Fig. 2-7a presents stochastic realisations of the geostatistical distributions of porosity and permeability distribution for a 2D model domain based on the geostatistical characteristic of the Opalinus Clay. The model was used for the simulation of gas release from an SF/HLW repository in the Opalinus Clay. The corresponding distribution of the capillary strength $P_{o,i}$ was generated based on the average value P_o , assuming Leverett scaling of the permeability field k_i normalized by its harmonic mean k_{harm} (and a variation of the porosity much lower as that of the permeability):

$$\eta_i = \frac{k_i}{k_{harm}} \Rightarrow P_{o,i} = \frac{P_o}{\sqrt{\eta_i}}$$
2-24

Figure 2-7b shows exemplarily the results of the 2-D gas release simulations from a gallery of SF/HLW emplacement tunnels in terms of the spatial distribution of gas saturations at different times. Gas saturation distribution at different times is dominated by three radial fronts around the gas-generating tunnels that converge sometime before 10³000 years. Gas saturation barely exceeds the value of 1% locally, depending on the distribution of the host rock heterogeneous field. Gas breakthrough at the top boundary occurs sometime after 25000 years and gas remains trapped for a long time in the regions which exhibit higher permeability and lower capillary pressure.

Comparisons of the modelling results were carried out for the stochastic property distributions and for the corresponding homogeneous property models. A good agreement of the calculated distributions of pressure and saturation was achieved for those cases with moderate property variability (i.e.; Opalinus Clay), whereas significant differences were seen for the Effingen Member. In all cases, the stochastic simulations provided a more realistic picture of the gas release processes around the disposal systems in that they account for phenomena such as gas entrapment and gas flow localization (capillary fingering).

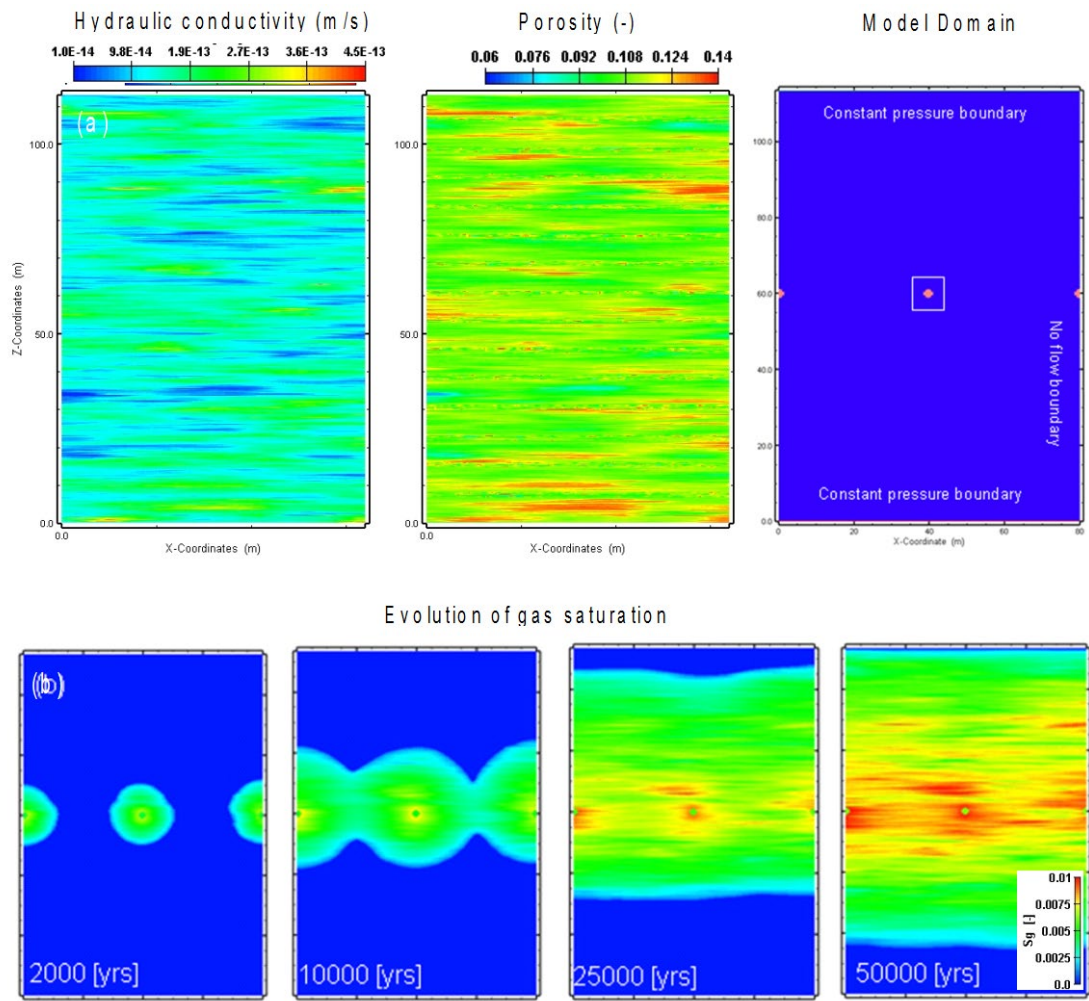


Fig. 2-7: Heterogeneous 2-D model for generic simulations of gas release from an SF/HLW repository in the Opalinus Clay: (a) Model domain and geostatistical distributions of permeability and porosity; (b) Spatial distribution of gas saturations at different times.

3 Gas-related properties of the potential host rocks

3.1 Relevant rock properties and constitutive relationships

A comprehensive set of geotechnical rock properties and constitutive relationships is required for numerical simulation of gas transport processes in the host rock formations. Chapter 3 provides an overview of the rock properties of concern, the underlying data sources and the derived reference parameters, required for the numerical simulations of gas release through the candidate host rocks.

The following parameters are required for modelling gas transport processes in the host rock formations:

- Total porosity and the associated microstructural features of the pore structure (e.g.; pore size distribution), governing both the gas storage and the gas transport capacity
- Intrinsic permeability, characterising the transport capacity of the host rock independent of the fluid
- Capillary pressure, characterising the coupling between gas and water pressure as a function of saturation
- Relative permeability, characterising the mobility of the different phases as a function of saturation
- Critical pressure for the on-set of pathway dilation, separating the regimes of reversible and irreversible deformation.

3.2 Opalinus Clay

3.2.1 Basic geological characteristics of the Opalinus Clay formation

The Opalinus Clay is part of a thick Mesozoic - Tertiary sedimentary sequence in the Molasse Basin of Northern Switzerland. It was deposited about 180 Ma ago in a shallow marine environment. Geological investigations on the regional scale confirmed the remarkable homogeneity of the formation. In the candidate siting regions of Northern Switzerland the Mesozoic sediments reveal uniform thickness over a distance of several tens of kilometres, dipping gently to the south-east, and are hardly affected by faulting.

The Opalinus Clay is a moderately over-consolidated claystone that has been formed by a complex burial and compaction history with two distinct periods of subsidence during the Cretaceous and late Tertiary, respectively. In the Molasse Basin the greatest burial depth of the Opalinus Clay was about 1000 m below the present depth. From about 10 Ma ago, alpine uplift and erosion brought the Opalinus Clay progressively up to its present burial depth. At Mont Terri, the Opalinus Clay reached a maximum depth of about 1000 m and the present burial depth is about 200 - 300 m.

On a regional scale, the mineralogical composition of the Opalinus Clay exhibits moderate lateral variability and a slight increase in clay content with depth. Quantitative laboratory analyses of core samples from Benken, Schlattingen and Mont Terri provide a total mass fraction of clay minerals of 40 - 80%, a quartz content of 15 - 35% and 5 - 25% calcite. The fraction of swelling clay minerals, with 10 - 15% illite / smectite mixed layers, is of particular

interest for the gas-related studies. Further minerals are siderite, pyrite and feldspar. The mass fraction of organic carbon is < 1%.

Porosity depends on clay content and burial depth; average values of 10%, 12% and 16% are reported for Schlattingen, Benken and Mont Terri Rock laboratory, respectively. Figure 3-1 depicts a compilation of porosity measurements from various locations in Northern Switzerland as a function of the burial depth; a clear decrease of porosity with depth is observed. Further geotechnical characteristics of the Opalinus Clay have been determined as part of comprehensive laboratory programmes, revealing moderate stiffness (Young’s modulus in the range 5 – 15 GPa), moderate strength (UCS values of the intact rock matrix between 10 and 35 MPa) and distinct swelling pressures (0.5 – 2 MPa).

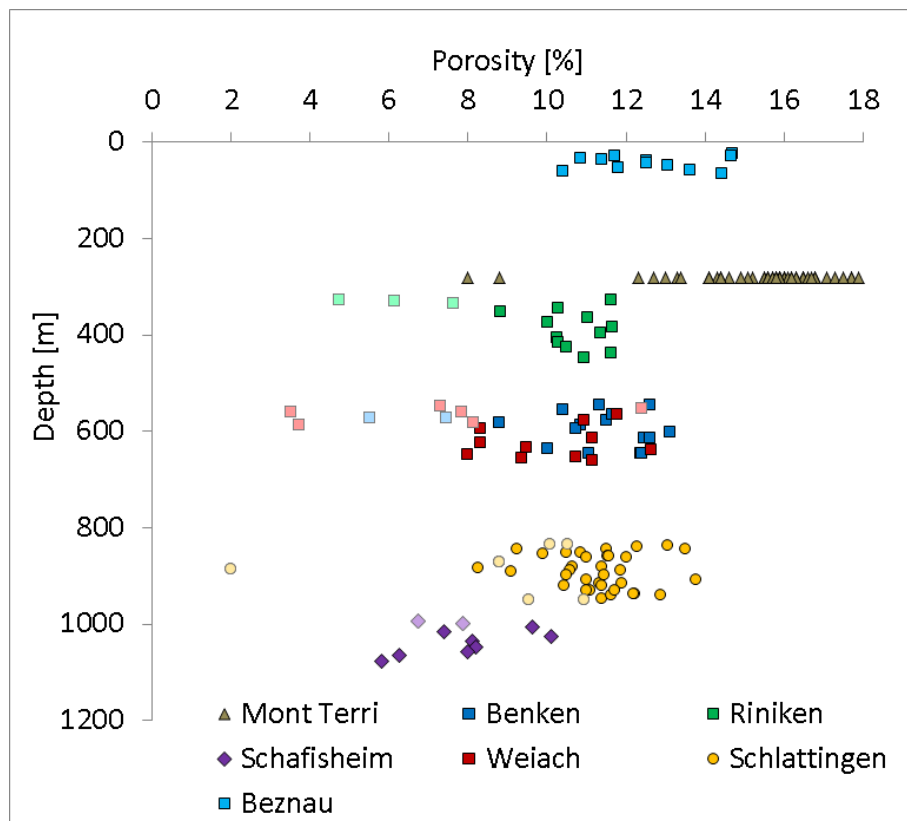


Fig. 3-1: Depth dependency of porosity measured in Opalinus Clay core samples recovered from different depths, from Mazurek (2011, 2013b), Ferrari et al. (2013) and Sarout et al (2013). Light colors denote core samples with exceptionally low clay content and/or high carbonates content.

Hydraulic tests have been performed in the Opalinus Clay in the Riniken, Schafisheim and Benken boreholes. Beauheim (2013) carried out a detailed review of the packer test data, applied methods and associated uncertainty providing an evaluation of the test interpretations quality. Field investigations suggest a hydraulic conductivity of the Opalinus Clay in the order of 10^{-13} to 10^{-14} m/s.

Over the course of the Mont Terri research programme, a comprehensive hydrogeological investigation programme has been conducted. Some of the key achievements on porewater flow in the Opalinus Clay were summarized in Bossart & Thury (2008):

- The highest packer tests transmissivities recorded for the Opalinus Clay at Mont Terri, which cannot be explained by EDZ phenomena are $< 1\text{E-}10 \text{ m}^2/\text{s}$. Hydraulic packer testing in boreholes and permeameter testing with drillcore specimen exhibit consistently low values for hydraulic conductivity, typically in the range between $5\text{E-}12$ and $1\text{E-}14 \text{ m/s}$ (see also Mettier et al. 2012). No significant variations in hydraulic conductivity are seen among the different facies. A reference value of $5\text{E-}13 \text{ m/s}$ has been reported for the Opalinus Clay at Mont Terri.
- No marked enhancement of hydraulic conductivity has been measured in the vicinity of tectonic features, indicating that fractures in the Opalinus Clay are tight. Extensive packer testing in the main fault did not reveal any correlation between hydraulic conductivity and fracture frequency along the boreholes.

3.2.2 Gas-related characteristics of the Opalinus Clay

Gas transport in low-permeability formations is largely controlled by the microstructure of the rock. A balanced assessment of gas transport processes in the Opalinus Clay therefore requires careful consideration of both structure and texture. Figure 3-2 illustrates the mineralogical and structural features of the Opalinus Clay in the ZNO area on various scales. Petrophysical logs in the Benken borehole indicate moderate variability and a slight increase of clay content with depth, suggesting a division of the Opalinus Clay into 5 lithostratigraphic sub-units (facies). Core inspection reveals a distinct anisotropy, made up of siderite concretions and silt and sandstone lenses, which are embedded in the clay-rich strata. The anisotropy due to bedding is largely a result of microscopic heterogeneity as seen in the thin sections, where diagenetic cementation of the pore space has been observed in the silty and sandy layers. Scanning electron microscope (SEM) images reveal that the size of the mineralogical components ($10^{-7} - 10^{-3} \text{ m}$) determines the microstructure of the rock. Quartz minerals may exhibit grain sizes in the range $0.01 - 1 \text{ mm}$, whereas the clay minerals form flake-like packages with typical sizes in the order of $100 \text{ nm} - 10 \text{ }\mu\text{m}$. The pore space of the rock is formed by a network of micro/meso- and macropores, which is too small (in the order $1 - 100 \text{ nm}$) to be shown by conventional SEM methods. This network of pores actually dominates the flow and transport properties of the rock (see also Appendix A).

Tab. 3-1: Volume fractions of the different pore classes, determined by adsorption and desorption isotherms (H_2O , N_2) after Nagra (2002). Complementary experimental evidence suggests that at least 20% of the total porewater can be attributed to the interlayer water.

Equivalent radius (nm)	Micropores < 1	Mesopores 1-25	Macropores > 25
Assumption: fraction of micropores is 20% (interlayers)			
N_2 -Isotherm	20	46-56	24-35
H_2O -Isotherm	20	54-63	17-26

Complementary methods were used to characterize the pore space of the Opalinus Clay, such as the measurement of the adsorption / desorption isotherms and mercury porosimetry (Nagra 2002). To obtain nitrogen and water isotherms, the powder samples were dried at temperatures of at least 120°C and degassed under vacuum. Nitrogen isotherms were measured at 77 K, water isotherms at 303 K by gravimetry in quasi-equilibrium mode, where water vapour was introduced at a constant, low flow rate. The pore size distributions were obtained by incremental saturation of the sample. Table 3-1 depicts the volume fractions of the different pore classes (definition according to IUPAC 1997), indicating that the majority of pores can be classified as mesopores (1 – 25 nm). The inferred macropore fraction in the order of 20 - 30% represents the pore space which is relevant for gas transport, because these pores are accessible to gases at moderate gas pressures (cf. Young's Equation 2-8).

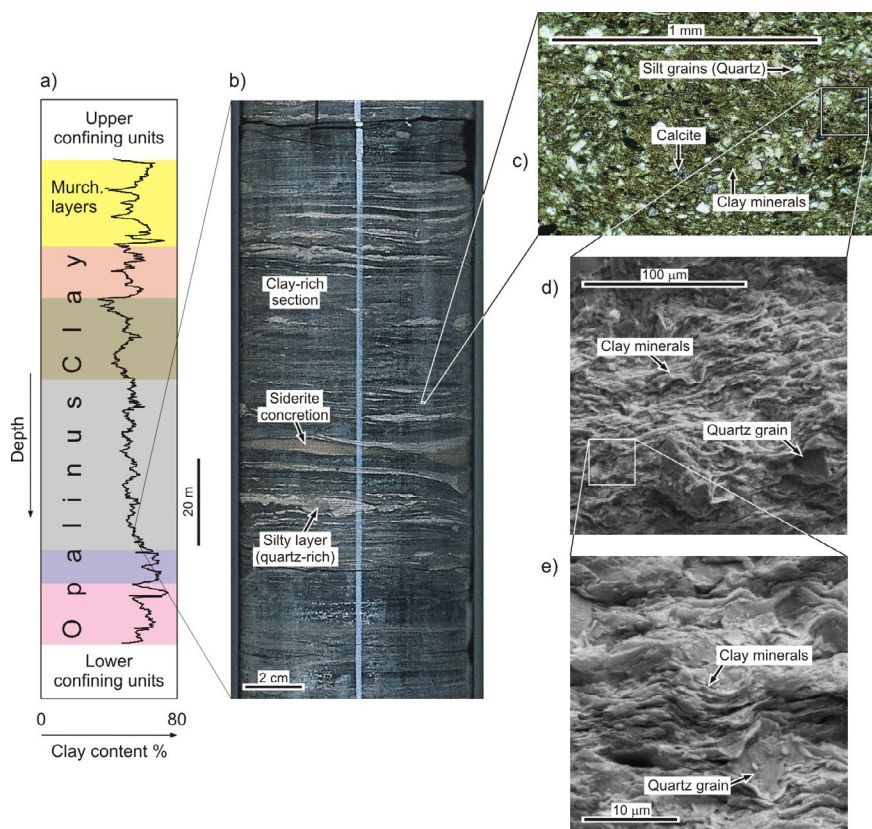


Fig. 3-2: Illustration of the mineralogy and structure of the Opalinus Clay at different scales, based on data from the Benken borehole in the ZNO siting area: (a) vertical profile of clay content determined by petrophysical logging, (b) core sample, (c) thin sections and (d+e) SEM images (after Nagra 2002).

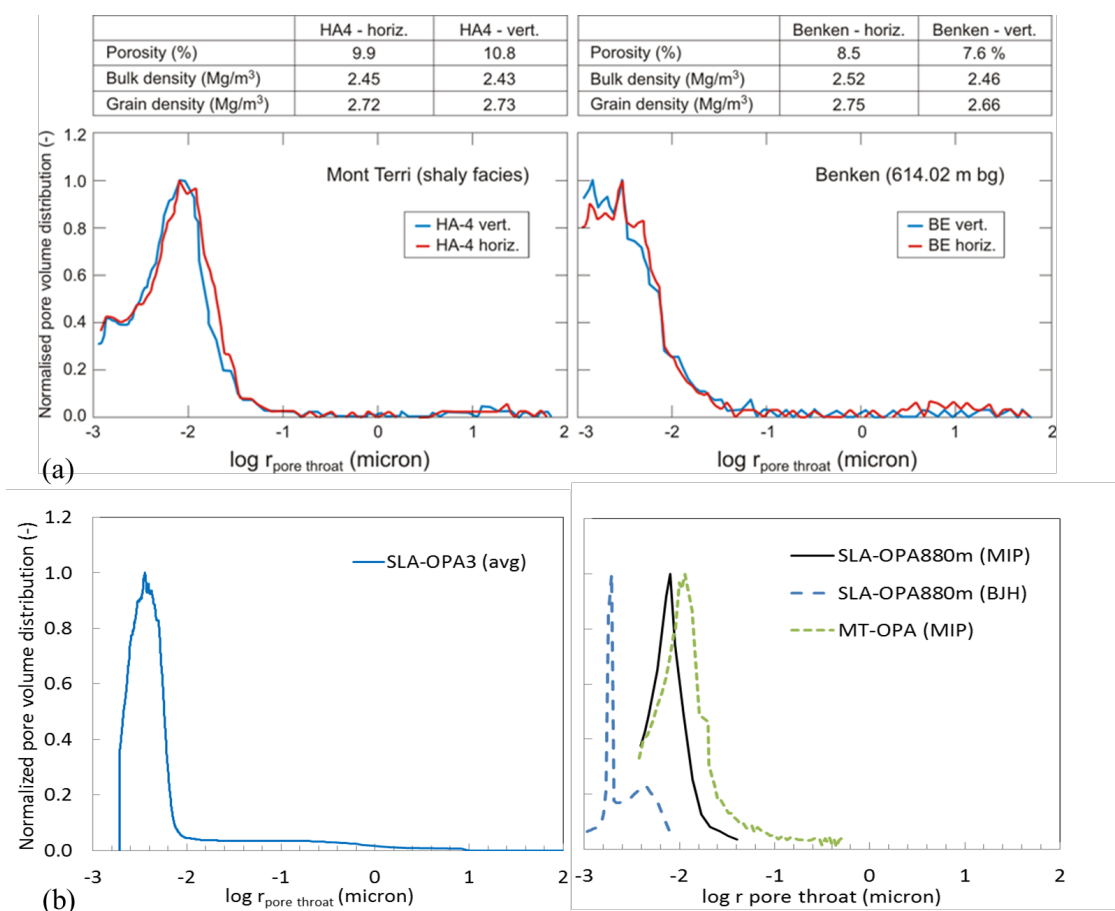


Fig. 3-3: Equivalent pore size distributions of drillcore samples: (a) from Benken (sampling depth 614.82 m below ground) and Mont Terri (shaly facies), determined by mercury intrusion methods at Chevron's laboratories in Houston (by courtesy of Philip Mariotti); (b) from Schlattingen (sampling depth 880 m below ground), determined by mercury intrusion methods at EPFL (left) and UPC (right), that was complemented by BJH method.

For mercury porosimetry, Hg was injected at increasing pressures into crushed, dried and degassed samples. In the context of the Project Entsorgungsnachweis (Nagra 2002) the maximum injection pressure was 200 MPa, and thus only pores with a radius larger than 3.7 nm could be detected. As part of Nagra's collaboration with the oil & gas industry, new mercury intrusion experiments were conducted in 2004 at the geotechnical laboratories of Chevron in Houston by Philip Mariotti using injection pressures up to 420 MPa. Two core samples from Benken and Mont Terri were tested - the equivalent pore size distributions are shown in Figure 3-3a. The general distributions are consistent with the results of the adsorption / desorption measurements, indicating that the majority of pores in the Opalinus Clay can be classified as mesopores. The more detailed comparison of the cores from Benken and Mont Terri reveals that the pore size distributions of the core samples from Benken are shifted towards the lower pore radii. This is a clear indication for the higher degree compaction of the samples from Benken, corresponding to the higher burial depth. More recent analyses were performed on core samples from a depth of 880m in the Schlattingen borehole by EPFL and UPC, shown in Figure 3-3b. UPC complemented the MIP analyses by the BJH method (Barrett, Joyner and Halenda) using the desorption information from the nitrogen adsorption tests. This

provides a wider range of pore size, whereby the spike around 0.004 micron is an artefact due to evaporation of metastable pore fluid (Romero et al. 2012).

Water retention functions describe the capacity of a porous medium to retain water at a given suction head. Thus, the water retention function is in principle identical to the water adsorption isotherm. The main differences are the experimental procedure and the preparation of the samples. Water retention curves of the Opalinus Clay were determined at the geotechnical laboratories of UPC (Universitat Politècnica de Catalunya, Barcelona / Spain), by stepwise desaturation and resaturation of core samples under controlled humidity (Nagra 2002, Muñoz et al. 2003). A comprehensive experimental programme was accomplished by the laboratories of GRS (Braunschweig), aimed at comparing the capillary pressure – saturation relationships of different clay formations. More recently, the Laboratory for Soil Mechanics at EPFL (École Polytechnique Fédérale de Lausanne) and the Department of Geotechnical Engineering and Geosciences at UPC determined water retention curves as well hydraulic and geomechanical properties of core samples from Mont Terri and from a deep borehole (Ferrari and Laloui 2012; Ferrari et al. 2013; Romero and Gomez 2013). Figure 3-4 depicts a compilation of water retention curves of Opalinus Clay samples from Mont Terri, determined by GRS (Zhang and Rothfuchs 2007), by UPC (Munoz et al. 2003, Romero and Gomez 2013), and by EPFL (Ferrari et al. 2013). Water retention curves of deep Opalinus core samples (880 m depth in Schlattingen borehole) are shown in Figure 3-5 using the FDT (Fluid Displacement Technique with Kerdane) for the volumetric determination of the specimen and for the determination of the suction as a function of water content and void ratio. The water retention curves in Figure 3-6 were based on the progressive method (Ferrari et al. 2013), where the wetting and drying paths of the retention curve are obtained on a single specimen from a core. This method better reproduces the hysteretic behaviour compared to the FDT method where the data points are from different specimens, resulting in greater scatter (Fig. 3.6).

Characteristic features of the Opalinus Clay are the high capillary pressures in the order of 10 MPa even at high water saturation > 90% and the marked hysteresis between wetting and drying path. The water retention measurements are fitted with the van Genuchten model according to Equation 2-10. The fitted parameters in terms of the capillary strength parameter P_0 and the shape parameter n and the corresponding water retention curve, shown in Figure 3-6, represent the reference value (RV) and alternative value (AV) for the shallow Opalinus Clay in Table 3-2. The corresponding van Genuchten parameters for the deep Opalinus Clay are given in Table 3-3 with the corresponding fitted curves shown in Figures 3-5 and 3-6.

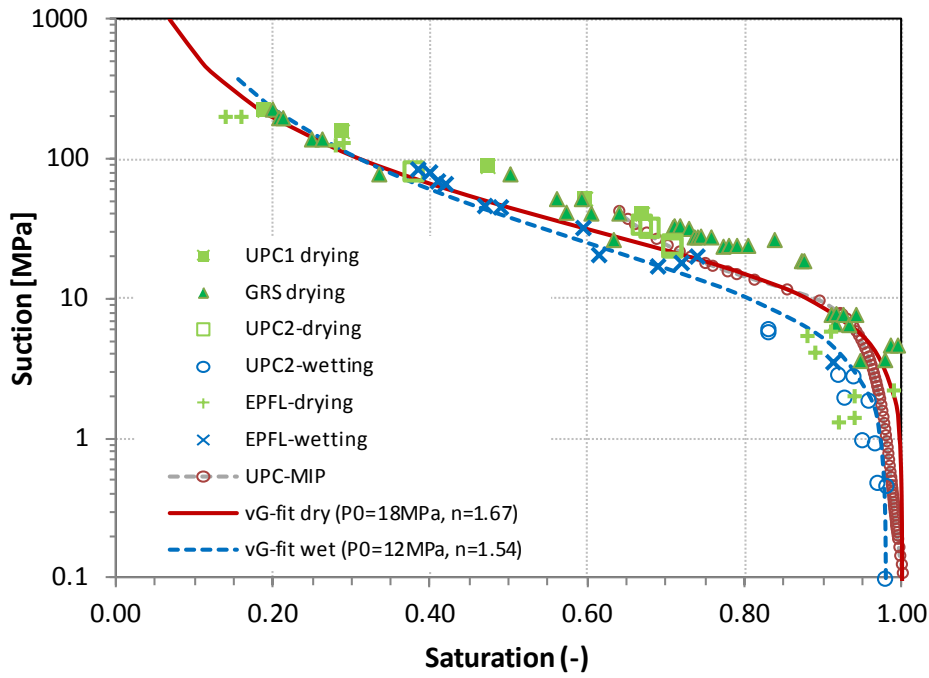


Fig. 3-4: Capillary pressure measurements (water retention curves) by stepwise desaturation and resaturation in a desiccator (photo). The experiments were conducted by GRS (Zhang & Rothfuchs 2007) and UPC (Muñoz et al. 2003, Romero and Gomez 2013) and by EPFL (Ferrari and Laloui 2012).

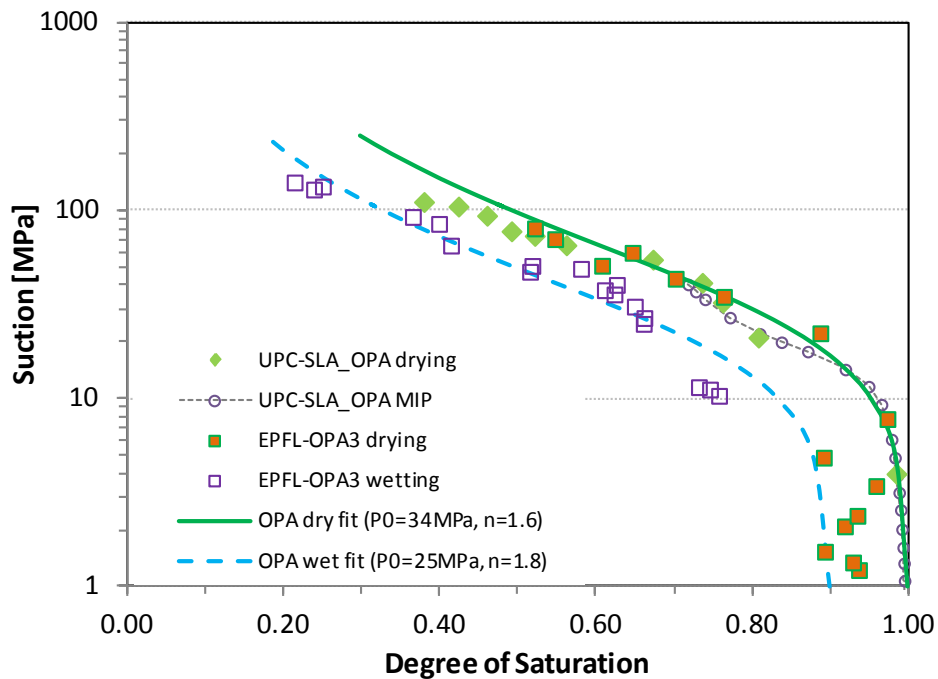


Fig. 3-5: Capillary pressure measurements (water retention curves) by stepwise desaturation and resaturation using a WP4c dew-point psychrometer and volumetric measurements using the Kerdane method on deep core samples from the Schlattingen borehole (Ferrari et al. 2013; Romero and Gomez 2013).

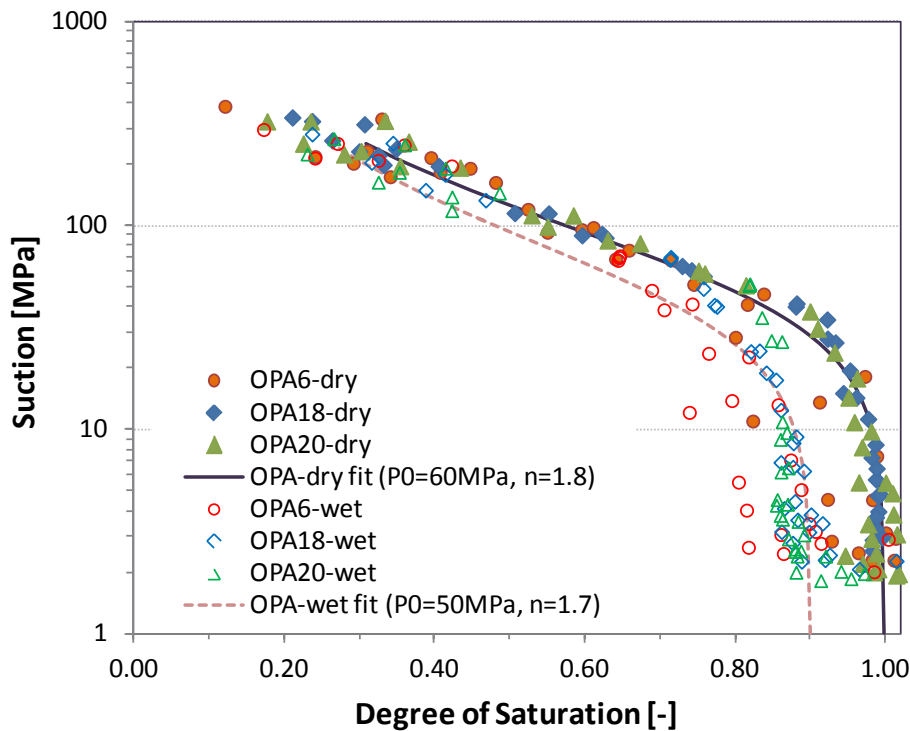


Fig. 3-6: Capillary pressure measurements (water retention curves) by stepwise desaturation and resaturation using a WP4c dew-point psychrometer and volumetric measurements using the progressive method on a deep core sample from the Schlattingen borehole (Ferrari et al. 2013).

The mobility of the gas in the intact Opalinus Clay (expressed in terms of a relative permeability relationship) can be determined by water and gas permeameter experiments in the laboratory and by in-situ gas injection tests in boreholes. An experimental data base for the derivation of relative permeabilities of the intact Opalinus Clay was elaborated in the context of the Project Entsorgungsnachweis. The key references of previous experiments are given in Nagra (2002) and in Marschall et al. (2005). Further experiments and data analyses have been conducted since then as part of the Mont Terri Project (Poller et al. 2007, Croisé et al. 2006) and in the context of the EU-funded integrated project NF-PRO (<http://www.nf-pro.org/>).

In the context of SGT / Stage 2, a complementary test programme was initiated, drawing on Opalinus Clay core samples from Mont Terri ("shallow samples") and from the Schlattingen borehole ("deep samples"). The tests were conducted in a triaxial cell with flow direction parallel (shallow samples only) and perpendicular to bedding at isotropic stress levels of 15 and 19 MPa, respectively (Romero and Gomez 2013). The corresponding gas injection pressures (14 and 18 MPa, respectively) remained below the confining stress. Figure 3-7 presents the results of gas injection tests on the core sample from Schlattingen SLA-1 in terms of gas pressures at the injection and outflow sides together with outflow volume and axial displacements.

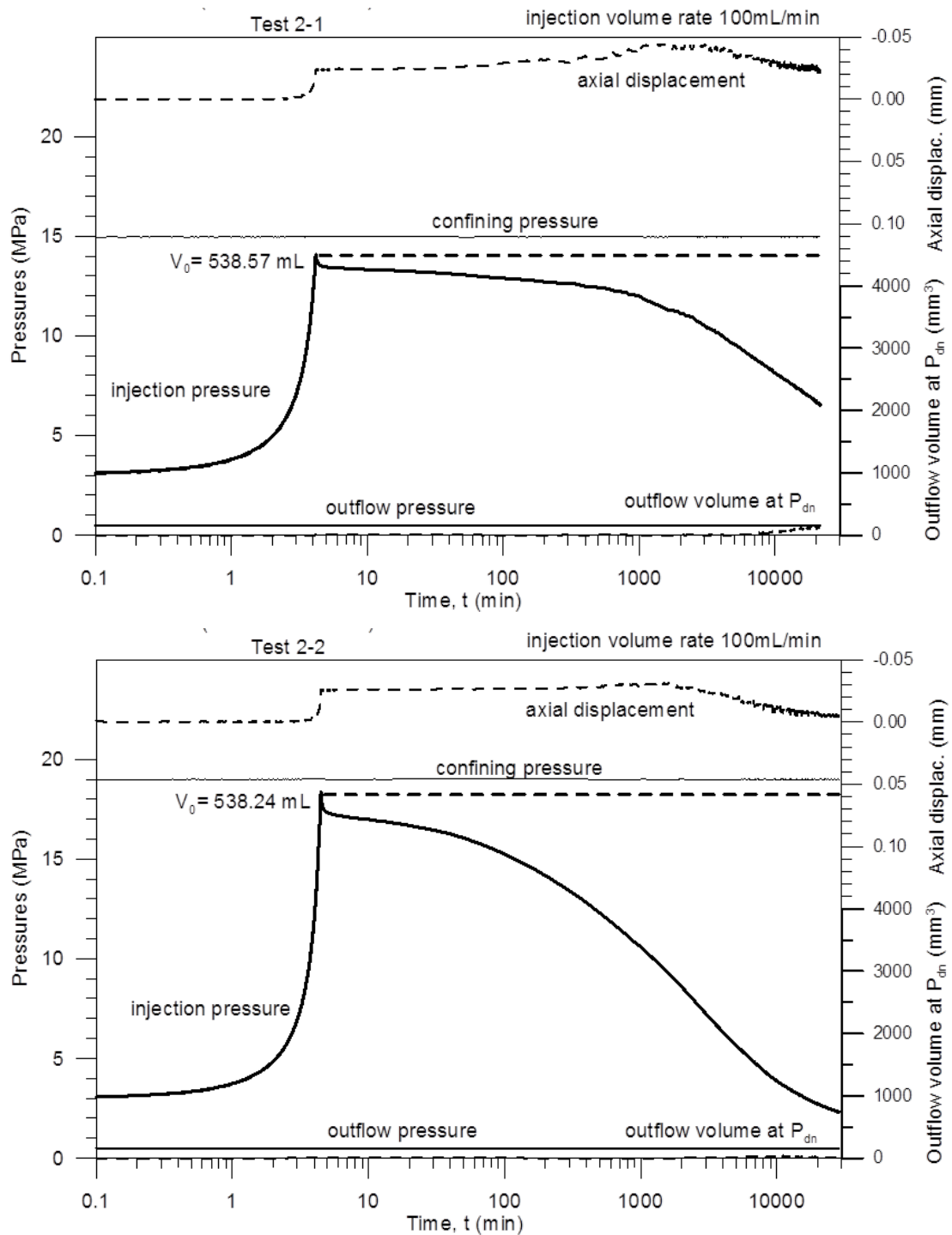


Fig. 3-7: Gas injection experiments on core sample OED/Opalinus Clay (879.79 - 880.01 m) from the SLA-1 borehole with isotastic stress conditions and flow orthogonal to bedding (from Romero and Gomez 2013). Measured time evolution of pressures at the injection and outflow sides together with outflow volume and axial displacements at confining pressures of (a) $p = 15 \text{ MPa}$ and (b) $p = 19 \text{ MPa}$.

The water/air permeability experiments on the Opalinus Clay sample show clear evidence for the dependency of water permeability on void ratio and thus on constitutive stress (estimated as the isotropic stress minus the air pressure at the injection point). Furthermore, a marked dependency of gas dissipation was observed on the direction of gas flow with respect to bedding orientation. Significantly higher gas flow rates were observed for the flow direction parallel to bedding. Another important observation is the marked dependency of volumetric strain on the constitutive stress changes during air injection / dissipation tests. The samples displayed expansion at the early fast air injection stage in response to constitutive stress decrease, and dominant compression on air pressure dissipation. During the early period after shut-in, the axial strain continued to expand despite the slight increase in constitutive stress due to air dissipation. This phenomenon occurred under increasing amount of air stored in the sample before the development of air-driven opening of discontinuities. Higher bulk moduli were consistently obtained in the air dissipation phases compared to bulk moduli from loading and unloading stages.

Detailed numerical analyses of the gas tests on both the shallow and the deep samples were conducted by Romero et al. (2013) and Senger et al. (2014). For this, a conceptual model for simulating two-phase flow of gas through a low-permeability clay formation was developed and implemented in the numerical two-phase flow simulator TOUGH2. Relevant information from the laboratory experiments in terms of the stress dependence of void ratios and associated changes in permeability were taken into consideration. These phenomena were implemented in the numerical model by relating the stress dependency through the corresponding effect of pore compressibility on porosity/permeability as a function of pore pressure through the effective stress concept at fixed total stress. In terms of two-phase flow properties, the laboratory experiments on the water retention behaviour were used, whereby the changes in porosity/permeability and corresponding effect on capillary pressure were accounted for by scaling the capillary strength parameter P_0 with permeability through the Leverett function.

The numerical simulation of the fast controlled-volume air injection experiments produced a significant improvement in terms of reproducing the observed injection pressure and outflow pressure responses for both the test with flow parallel to bedding and for the test with flow normal to bedding (Fig. 3-8). The experiments for normal to bedding indicated a significant delay on the outflow response after full injection of air volume from the injection chamber as compared to the experiment with flow parallel to bedding that indicated a relatively rapid outflow pressure response. The injection pressure response suggests that preferential gas paths were developed as gas was migrating into the expanding pores of the samples at increasing injection pressures resulting in a higher mobility gas behaviour resulting in a rapid pressure recovery following gas breakthrough. This delay in the outflow pressure response is also observed in core samples from a deep borehole in the Opalinus Clay, on which similar laboratory experiments have been conducted (Romero et al. 2012).

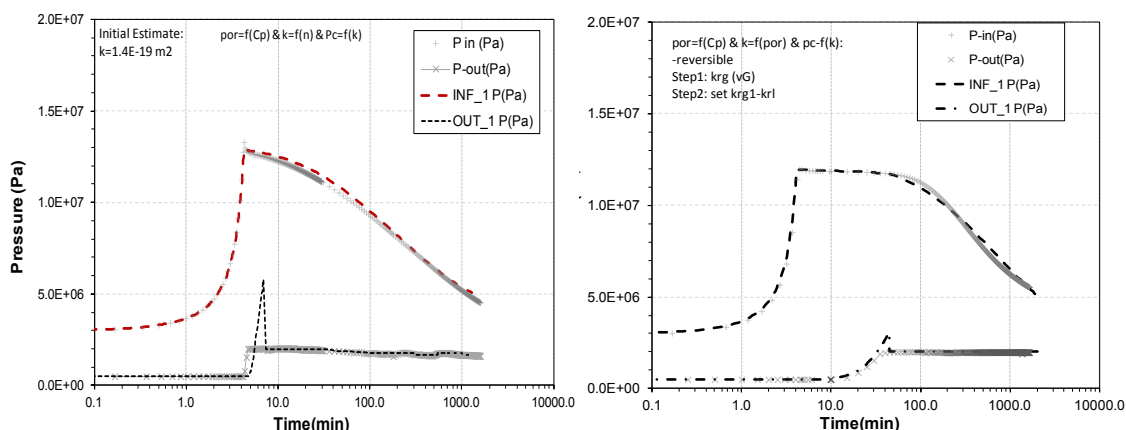


Fig. 3-8: Simulated and measured pressures for air-pulse injection tests on core samples from Mont Terri ("shallow samples") for flow parallel (left) and perpendicular (right) to bedding after Senger et al. (2014).

3.2.3 Reference parameters of the Opalinus Clay

Flow and transport processes in the Opalinus Clay are largely linked to the connectivity of the microscopic pore network of the rock matrix. Fractures tend to self-seal, when the effective normal stress (mean normal stress minus pore pressure) exceeds the magnitude of the swelling pressure of the rock. Consequently, it can be assumed that gas transport in the Opalinus Clay occurs mainly in the intact rock matrix as long as the gas pressures are significantly lower than the confining rock stress. The subsequent reference parameters of the Opalinus Clay are referring to the gas transport parameters of the intact rock matrix.

Representative hydraulic data bases were compiled as part of SGT stage 2 and the corresponding hydraulic reference parameters have been derived for all host rocks in the candidate siting regions. For the Opalinus Clay two different sets of reference parameters were specified, namely for the shallow and deep repository configurations (shallow: 300 - 500 m bg.; deep: 500 - 900 m bg). Accordingly, two sets of gas related reference parameters have been elaborated (Table 3-2 and 3-3, respectively). The parametric models used for the capillary-saturation relationship and the relative permeability of the shallow Opalinus Clay are shown in Figure 3-9 (reference values according to Table 3-2). For the deep Opalinus Clay, the reference values are compiled in Table 3-3, with the corresponding two-phase parameter curves shown in Figure 3-10.

Tab. 3-2: Reference values for the gas-related parameters of the undisturbed Opalinus Clay for a shallow repository in Northern Switzerland (RV – reference value; AV – alternative value).

Parameter	RV	AV	Remarks
Opalinus Clay – shallow (300 – 500 m bg)			
Intrinsic permeability normal to bedding k_{\perp} [m ²]	1×10^{-20}	2×10^{-21} (1) 5×10^{-20} (2)	RV: corresponds to the reference value for hydraulic conductivity at Mont Terri. AV ⁽¹⁾ : corresponds to the reference value for hydraulic conductivity in the ZNO. AV ⁽²⁾ : corresponds to the upper range for hydraulic conductivity at Mont Terri.
Anisotropy coefficient k_{\parallel}/k_{\perp}	5	1	RV: according to Nagra (2002), Romero and Gomez (2013). AV: no significant anisotropy
Capillary pressure - saturation relationship			van Genuchten parametric model (Equ. 2-10)
Capillary strength P_0 [MPa] Shallow (< 500 m)	18	12^1 4.6^2	RV: derived from capillary pressure measurements (drying path) AV1: derived from capillary pressure measurements (wetting path) AV2: Estimates from field tests (Marschall et al. 2005)
Shape Parameter n	1.67	1.54	RV: derived from capillary pressure measurements (drying path) AV: derived from capillary pressure measurements (wetting path)
Relative permeability – saturation relationship			van Genuchten/Mualem parametric model (Equ. 2-14 & 2-15) using the shape parameter n from the P_c - S curve
Residual water saturation S_{wr} [-]	0.5	0.1	RV: according to the results of adsorption / desorption measurements, suggesting that 50% of the total pore space can be classified as micro- and mesopores. AV: assuming that most of the pore water is mobile (not supported by experimental data)
Residual gas saturation S_{gr} [-]	0.00	0.003	RV: effective gas entry pressure of the rock is infinitesimal AV: the residual gas saturation determines the effective gas entry value. Effective gas entry values were determined by gas permeability testing at Mont Terri and Benken (cf. Marschall et al. 2005)
Total porosity [%]	12%	16%	AV: Porosity of the shaly facies at Mont Terri: 16%. RV: corresponds to the reference value for the porosity of the ZNO area. At Mont Terri, the sandy facies exhibits typical porosity values of about 12%
Lower bound of fracture pressure [MPa]	$\sigma_v = \rho_{rock} \cdot g \cdot z$	-	RV: lithostatic pressure σ_v at repository level ($\rho_{rock} = 2.5 \text{ Mg/m}^3$, overburden z in m bg) AV: -

Parameter	RV	AV	Remarks
Threshold pressure for pathway dilation [% of σ_v]	80%	-	RV: the on-set of pathway dilation is assumed at about 80% of the lithostatic pressure. AV: -
Relationship between intrinsic permeability and hydraulic conductivity (20°C):			
$k \left[m^2 \right] = \frac{\eta_w}{\rho_w \cdot g} \cdot K \approx 1 \times 10^{-7} \cdot K \left[m/s \right]$			
η_w - dynamic viscosity of water, [Pa·s] ρ_w - density of water, [kg m ⁻³] g - gravitational acceleration, [m s ⁻²]			

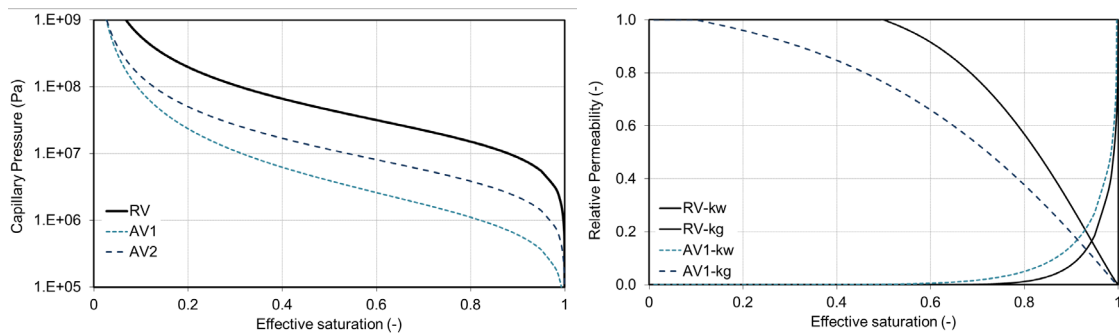


Fig. 3-9: Parametric models of capillary pressure and relative permeability k_r for water (w) and gas (g), representative for the shallow (undisturbed) Opalinus Clay formation in Northern Switzerland (reference parameter values RV and alternative values AV).

Tab. 3-3: Reference values for the gas-related parameters of the undisturbed Opalinus Clay for a deep repository in Northern Switzerland (RV – reference value; AV – alternative value).

Parameter	RV	AV	Remarks
Opalinus Clay – deep (500 – 900 m bg)			
Intrinsic permeability normal to bedding k_{\perp} [m ²]	2×10^{-21}	1×10^{-21}	RV: corresponds to the reference value for hydraulic conductivity at Benken (Nagra 2002). AV: corresponds to the lower range for hydraulic conductivity at Benken.
Anisotropy coefficient k_{\parallel}/k_{\perp}	5	1	RV: according to Nagra (2002). AV: no significant anisotropy
Capillary pressure - saturation relationship			Parametric model according to van Genuchten (Equ. 2-10)
Capillary strength P_0 [MPa] Deep (> 500 m)	34	60^1 18^2	RV: derived from capillary pressure measurements (drying path) (Romero and Gomez 2013) AV1: derived from capillary pressure measurements (drying path) (Ferrari et al. 2013) AV2: from shallow OPA
Shape Parameter n	1.6	1.8	RV: derived from capillary pressure measurements (drying path) AV: derived from capillary pressure measurements (drying path – high P_0)
Relative permeability – saturation relationship			Parametric model according to van Genuchten/Mualem (Equ. 2-14 & 2-15) using the shape parameter n from the Pc-S curve
Residual water saturation S_{wr} [-]	0.5	0.1	RV: according to the results of adsorption / desorption measurements, suggesting that 50% of the total pore space can be classified as micro- and mesopores. AV: assuming that most of the pore water is mobile
Residual gas saturation S_{gr} [-]	0.00	0.003	RV: effective gas entry pressure of the rock is infinitesimal AV: the residual gas saturation determines the effective gas entry value. Effective gas entry values were determined by gas permeability testing at Mont Terri and Benken (cf. Marschall et al. 2005)
Total porosity [%]	12%	10%	RV: Porosity measurements from Schlattingen core (OPA-20) (avg. Value between different core samples) 16%. AV: corresponds to the lower value in OPA-of about 10%
Lower bound of fracture pressure [MPa]	$\sigma_v = \rho_{rock} \cdot g \cdot z$	-	RV: lithostatic pressure σ_v at repository level ($\rho_{rock} = 2.5 \text{ Mg/m}^3$, overburden z in m bg) AV: -
Threshold pressure for pathway dilation [% of σ_v]	80%	-	RV: the on-set of pathway dilation is assumed at about 80% of the lithostatic pressure. AV: -

Parameter	RV	AV	Remarks
Relationship between intrinsic permeability and hydraulic conductivity (20°C):			
$k [m^2] = \frac{\eta_w}{\rho_w \cdot g} \cdot K \approx 1 \times 10^{-7} \cdot K [m/s]$			
η_w			- dynamic viscosity of water, [Pa·s]
ρ_w			- density of water, [kg m ⁻³]
g			- gravitational acceleration, [m s ⁻²]

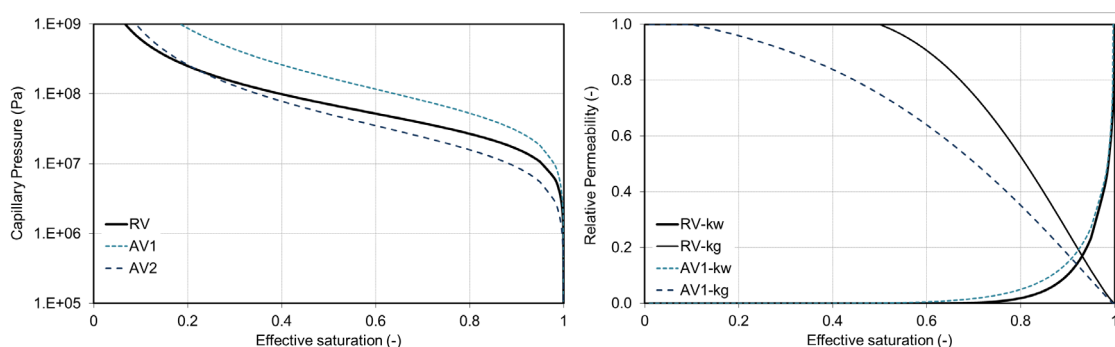


Fig. 3-10: Parametric models of capillary pressure and relative permeability k_r for water (w) and gas (g), representative for the "deep" Opalinus Clay formation (reference parameter values RV and alternative values AV)

3.3 'Brown Dogger'

3.3.1 Basic geological characteristics of the 'Brown Dogger'

The informal term 'Brown Dogger' relates to the suite of generally clay-rich rock units stratigraphically located between the Opalinus Clay and the Malm. The rocks range from claystones to calcareous marls. The rocks of the 'Brown Dogger' are considered as potential host rocks for the geological disposal of L/ILW in the ZNO and NL geological siting regions in Northern Switzerland.

A comprehensive survey of the available stratigraphic and lithologic data base on the 'Brown Dogger' sequence is given in Bläsi et al. (2013) together with an evaluation of the depositional environment in the context of the general basin evolution. The detailed lithologic and stratigraphic characterisation of the 'Brown Dogger' in Nagra's investigation boreholes Weiach and Benken and in the geothermal well Schlattingen-1 suggests that the host rock formation is dominated by rather homogeneous sequences of claystones and clay-rich marls with intermitted thin layers of limestones and sandy-calcareous marls ("harte Bänke") with a typical thickness of decimeters. With regard to the evaluation of porewater flow in the microscopic pore system of the intact rock matrix, two types of heterogeneous sedimentary structures are of special interest, namely (a) oolitic ironstones and (b) calcareous sandstones and limestone beds. In the area of interest (siting regions NL, ZNO, SR) the stratigraphic sequence comprises the following units:

- Wutach Formation, a heterogeneous succession of marly to calcareous oolitic ironstones.
- Variansmergel-Formation, a sequence of limestones with fossils and calcareous marls.

- Parkinsoni-Württembergica layers, a sequence of thick and uniform claystones and marls with thin oolitic beds
- Humphriesiolith-Formation, a heterogeneous succession of thin oolitic ironstones and limestones
- Wedelsandstein-Formation, a rather uniform sequence of silty and clayey marls with intercalations of bioturbites. The lower Wedelsandstein-Formation exhibits a succession of calcareous sandstones and sandy claystones.
- Murchisonae-Oolith-Formation, a sequence of oolitic ironstones and sandstones.

The mineralogical database of 'Brown Dogger' core samples provides insights into the dependency of porosity with depth and contents of mineralogical components. In Fig. 3-11 the combined porosity data from Mazurek (2011, 2013a), Ferrari et al. (2013) and Sarout et al. (2013) are plotted versus depth from where the core sample was recovered. The data points are distinguished based on clay content, with light colors denoting core samples with low clay content below a threshold of 30%, and darker colors with clay content above 30%. Porosities in the 'Brown Dogger' span a wide range of values from 1% to 18% with 71% of the data having porosities ranging between 8% and 14%. The data exhibits a distinct dependency on mineralogy with the majority of porosities below 10% corresponding to cores with low clay content. Due to the wide range of porosities associated with changes in mineralogy, a distinct depth-dependency cannot be identified in these core data. In general, porosities from Schlattingen exhibit a larger variation compared to Benken. Core samples from Schafisheim exhibit significantly decreased porosities (1% to 8%) that possibly relate to mineralogy as well as compaction from greater overburden. In the candidate siting regions ZNO and NL, the representative mean porosity value of the 'Brown Dogger' is 10%. Further geotechnical characteristics of the 'Brown Dogger' have been determined as part of recent laboratory programmes, revealing similar stiffness as the Opalinus Clay (Young's modulus in the range 5 – 15 GPa), but higher strength (UCS values of the intact rock matrix between 30 and 70 MPa) and lower swelling pressures (0.2 – 1 MPa).

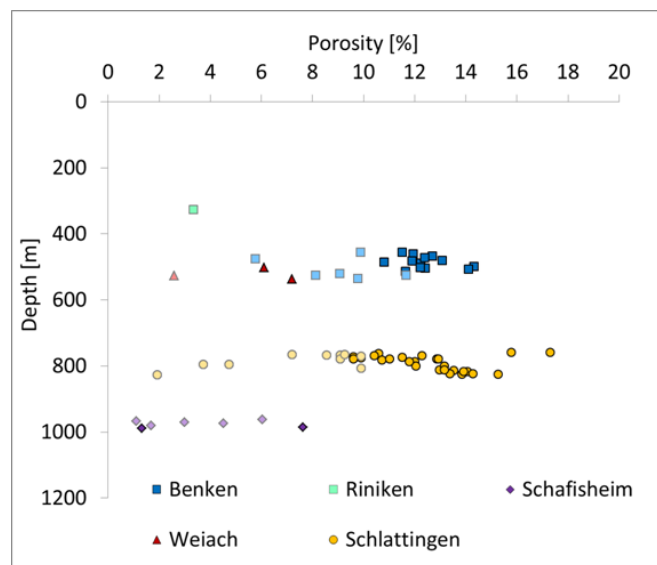


Fig. 3-11: Depth dependency of porosity measured in 'Brown Dogger' core samples recovered from different depths (from Mazurek 2011, 2013, Ferrari et al 2013, and Sarout et al 2013). Light colors denote core samples with exceptionally low clay content and/or high carbonates content.

Hydraulic conductivity was obtained from the packer tests, indicating typical values in the range between $1\text{E-}11$ and $1\text{E-}13$ m/s (Beauheim 2013). In general, the largest conductivities correspond to packer tests spanning across the Wedelsandstein sequence with the highest value of $1.4\text{E-}9$ m/s observed in Schlattingen. The hydraulic conductivity of the Wedelsandstein Formation in Benken is lower, despite the more abundant presence of brittle structures (see also Mazurek 2013a). On the other hand, packer tests spanning the Parkinsoni-Württembergica and Ifenthal Formations show that hydraulic conductivity in Schlattingen is almost two orders of magnitude larger compared to Benken where brittle structures in the carbonate facies are practically absent. Fracture transmissivities from packer tests in the 'Brown Dogger' are ranging between $1\text{E-}12$ and $5\text{E-}8$ m²/s. The distinct clustering of brittle structures observed by Mazurek (2013a) suggests a high spatial variability of pore water flow in the fracture systems of the 'Brown Dogger'.

3.3.2 Gas-related characteristics of the 'Brown Dogger'

Geophysical logging and core inspection in the boreholes Weiach, Benken und Schlattingen reveal a significant variability in lithological and mineralogical parameters of the stratigraphic sequence of the 'Brown Dogger'. The lithological facies inventory comprises sequences of two rock types: (1) clay-rich marls and marly claystones alternating with thin layers of sandy-calcareous marls, and (2) carbonate-rich iron-oolitic limestones (Fig. 3-12a&b). Complementary microstructural investigations on core samples from the borehole SLA-1 display further scales of internal variability of mineralogical and petrophysical parameters within the different facies (Fig. 3-12c). Appendix B presents a study of microstructural features of the 'Brown Dogger' and compares its pore connectivity with the Opalinus Clay.

Brittle structures in the layers of limestones and sandy-calcareous marls are of high significance for fluid flow and gas transport in the 'Brown Dogger' as they represent potential water conducting features (WCF). Mazurek (2013a) identified 6 classes of discrete water conducting features in the boreholes Benken and Schlattingen SLA-1. The WCF distribution indicates a pronounced clustering, which is however observed differently in each borehole. In Benken, 37 WCFs were observed. Of these, 31 are observed in the Wedelsandstein formation with some WCFs distributed across the formation and a large cluster forming near the top of the formation below the boundary to the limestones of the Humphriesi formation. WCFs are absent in the Parkinsoni-Württembergica formation. In Schlattingen 85 WCFs were observed. The Ifenthal formation appears to be severely fractured with 44 WCFs distributed across the entire formation. The Parkinsoni-Württembergica formation is characterized by distinct clustering of 33 WCFs, whereas only 5 WCFs are observed in the Wedelsandstein Formation.

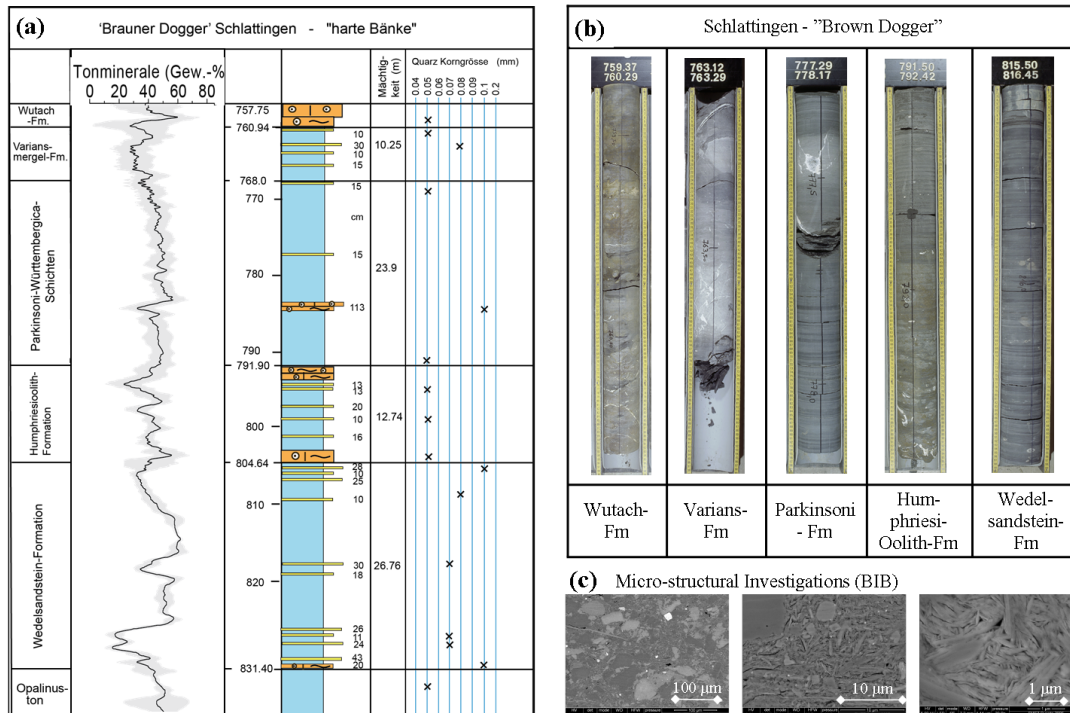


Fig. 3-12: The 'Brown Dogger' in Schlattingen (after Bläsi et al. 2013): (a) Stratigraphy and rock mineralogical compositions indicate the correlation between carbonate-rich limestone facies (brown) and clay-rich facies (blue) alternating with sandy-calcareous marls (yellow); (b) photos of core samples, representing the main lithostratigraphic units in the 'Brown Dogger'; (c) SEM images with different magnification of a core sample from the Parkinsoni-Württembergica section (781.5 m bg) recovered from the Schlattingen SLA-1 borehole. The samples were polished with a Broad-Ion-Beam technique (BIB) perpendicular to bedding.

EPFL (Ferrari et al. 2013) and UPC (Romero and Gomez 2013) performed mercury intrusion porosimetry (MIP) on several core samples of the 'Brown Dogger' (BD) sequence recovered from the Schlattingen borehole. The normalized pore-size distributions (PSD) from the MIP measurements of the different samples are shown in Fig. 3-13. Generally, the modes of the pore-size distributions of the BD core samples tend to be somewhat greater than those from the Opalinus Clay (Fig. 3-4). For the calcareous zones of the 'Brown Dogger' the PSD curves are even smaller than those in the clay-rich sequences.

Water retention curves (WRC) were measured on several core samples from the Schlattingen borehole (Ferrari et al. 2013; Romero and Gomez 2013). The water retention data of the 'Brown Dogger' along the drying and wetting path are plotted in Fig. 3-14. However, the fitted WRCs indicate a relatively high capillary strength parameter compared to those data from the Opalinus Clay. Similar to the Opalinus Clay, some hysteresis is indicated particularly for the WRCs based on the progressive method (see Ferrari et al. 2013). The WRC curves are representative of the unfractured rock matrix and do not take into account the expected decrease in capillary pressure in fractures.

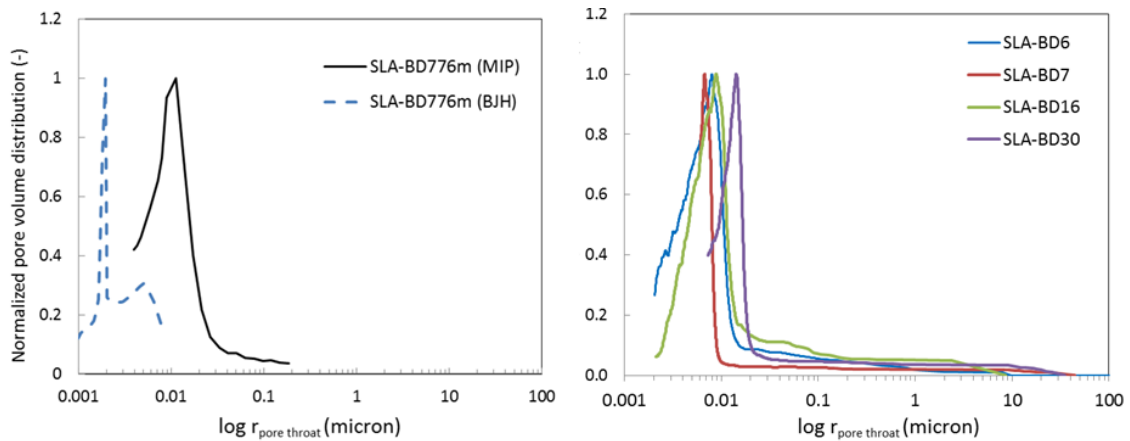


Fig. 3-13: Equivalent pore size distributions (normalised) of drillcore samples from Schlattigen (sampling depth ranging from 766.7 to 807.4 m bg), determined by mercury intrusion methods at EPFL (left) and UPC (right), that was complemented by BJH method.

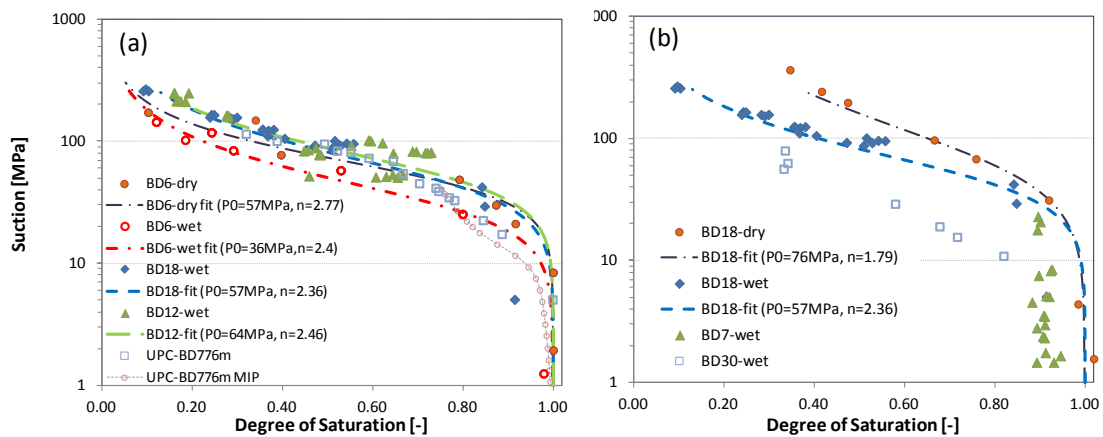


Fig. 3-14: Capillary pressure measurements (water retention curves) on a deep BD core samples from the Schlattigen borehole. Test are performed by stepwise desaturation and resaturation using a WP4c dew-point psychrometer and volumetric measurements (Ferrari et al. 2013; Romero and Gomez 2013): (a) using the Kerdane method; (b) using the progressive method for volume measurements.

Similar to the Opalinus Clay core samples from the Schlattigen borehole, two gas injection tests were performed for a core sample from the 'Brown Dogger' sequence (sample OED 20 / 776.51 - 776.72 m bg; Parkinsoni-Württembergica Fm.). The tests were conducted with flow direction perpendicular to bedding at isotropic stress levels of 15 and 19 MPa, respectively. The corresponding gas injection pressures (14 and 18 MPa, respectively) remained below the confining stress. Figure 3-15 presents the results of the tests in terms of gas pressures at the injection and outflow sides together with outflow volume and axial displacements.

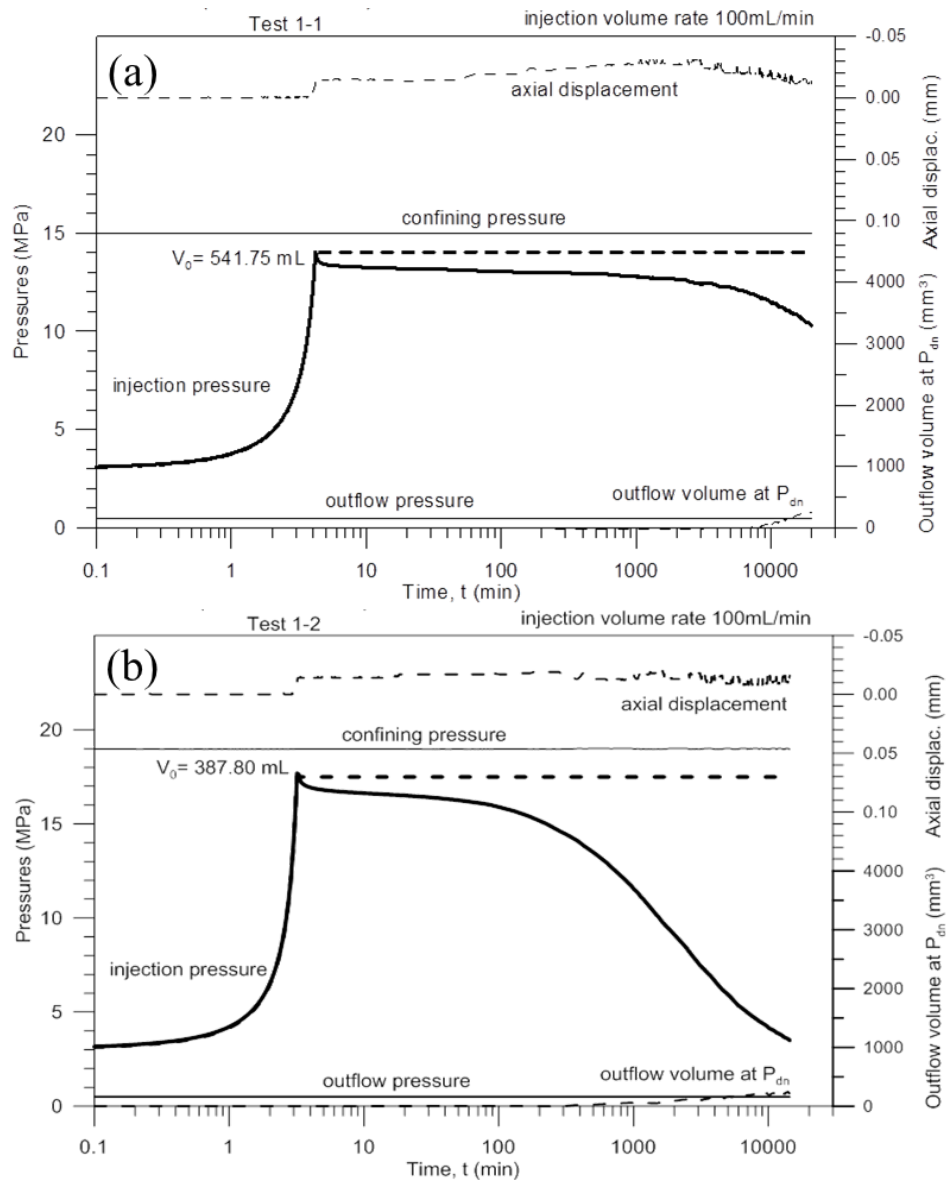


Fig. 3-15: Gas injection experiments on core sample OED 20/'Brown Dogger' (776.51 - 776.72 m) from the SLA-1 borehole with isostatic stress conditions and flow orthogonal to bedding (from Romero and Gomez 2013). Measured time evolution of pressures at the injection and outflow sides together with outflow volume and axial displacements at confining pressures of (a) $p = 15$ MPa and (b) $p = 19$ MPa.

The water/air permeability experiments on the 'Brown Dogger' sample shows evidence for stress dependency of void ratio and water permeability. Despite its slightly higher intrinsic permeability, the 'Brown Dogger' samples underwent slightly lower air dissipation rates during the recovery stage compared to the equivalent tests performed on Opalinus Clay. As the Opalinus Clay samples did, the 'Brown Dogger' sample displayed expansion at the early fast air injection stage in response to constitutive stress decrease, and dominant compression on air pressure dissipation. Overall, the 'Brown Dogger' exhibits a less distinct stress coupling of hydro-mechanical properties than the Opalinus Clay.

3.3.3 Reference parameters

In the 'Brown Dogger' hydrogeologic evidence suggests that brittle (tectonic) structures in the layers of limestones and sandy-calcareous marls can form discrete water conducting features with non-negligible fracture transmissivity, contributing substantially to the overall pore water flow in the formation ("fracture flow"). The distinct clustering of the observed brittle structures implies a rather high spatial variability of pore water flow in the hydraulic fracture network. Furthermore, the geometric characteristics of the fracture network (fracture frequencies, fracture size, aperture) are more a site specific rather than a rock specific feature. In this report, emphasis is on rock specific characteristics of the candidate host rocks. Consequently, the subsequent reference parameters of the 'Brown Dogger' are referring to the gas transport parameters of the intact rock matrix. Complementary analyses of gas transport in the discrete water conducting features of the 'Brown Dogger' would need a site specific assessment of the discrete water conducting features in the candidate siting areas which is beyond the focus of this report.

Representative hydraulic data bases were compiled as part of SGT stage 2 and the corresponding hydraulic reference parameters for the 'Brown Dogger' have been derived. Different sets of reference parameters were specified for the clay-rich marls (KMA) and the sandy-calcareous sequences (SKA), respectively. Accordingly, two sets of gas related reference parameters have been elaborated (Table 3-4). The parametric models used for the capillary-saturation relationship and the relative permeability of the 'Brown Dogger' are shown in Figure 3-16 (reference values according to Table 3-4).

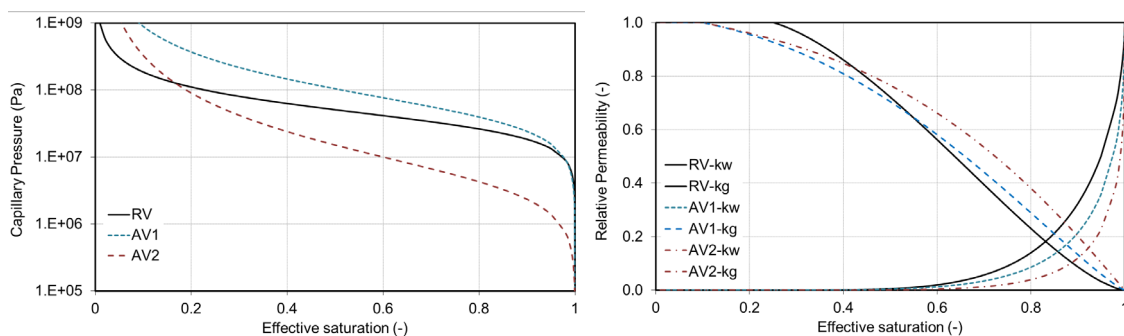


Fig. 3-16: Parametric models of capillary pressure and relative permeability k_r for water (w) and gas (g), representative for the 'Brown Dogger' formation (reference parameter values RV and alternative values AV1 and AV2).

Tab. 3-4: Reference values for the gas-related parameters of the clay-rich sequences of the 'Brown Dogger' in Northern Switzerland (RV – reference value; AV – alternative value).

Parameter	RV	AV	Remarks
Undisturbed host rock			
Intrinsic permeability (KMA ⁽¹⁾ , SKA ⁽²⁾) k_{\perp} [m ²]	1×10^{-20} (1) 1×10^{-19} (2)	1×10^{-18} (1) 1×10^{-19} (2)	RV: corresponds to the reference value of hydraulic conductivity for KMA, SKA AV: representation of the 'Brown Dogger' as a homogeneous and anisotropic porous medium
Anisotropy coefficient k_{\parallel}/k_{\perp}	1	10	RV: AV: -
Capillary pressure - saturation relationship			Parametric model according to van Genuchten (Equ. 2-10)
Capillary strength P_0 [MPa] (no distinction between KBA and SKA)	36	50^{1*} 4.6^{2*}	RV: derived from WRCs (lowest wetting path), (Ferrari et al. 2013), accounting for fractures AV ^{1*} : derived from WRCs by EPFL and UPC (representative of matrix) AV ^{2*} : assumed value, derived from field tests in sandy facies of the Opalinus Clay (Marschall et al. 2005)
Shape Parameter n (no distinction between KBA and SKA)	2.4	1.8^{1*} 1.54^{2*}	RV: derived from WRCs AV ^{1*} : lowest value from WRC fits AV ^{2*} : assumed value, derived from field tests in sandy facies of the Opalinus Clay (Marschall et al. 2005)
Relative permeability – saturation relationship			Parametric model according to van Genuchten/Mualem (Equ. 2-14 & 2-15) using the shape parameter n from the P_c - S curve
Residual water saturation S_{wr} [-]	0.25	0.1	RV: reduced from MIP data to account for fracture effect AV: assuming that most pore water is mobile
Residual gas saturation S_{gr} [-]	0.00	0.00	RV: effective gas entry pressure of the rock is infinitesimal AV: -
Total porosity [%]	10%	8%	RV: Porosity measurements from Schlattingen cores (see Fig. 3-11) AV: corresponds to the lower value in BD at depth
Lower bound of fracture pressure [MPa]	$\sigma_v = \rho_{rock} \cdot g \cdot z$	-	RV: lithostatic pressure σ_v at repository level ($\rho_{rock} = 2.5 \text{ Mg/m}^3$, overburden z in m bg) AV: -
Threshold pressure for pathway dilation [% of σ_v]	80%	-	RV: the on-set of pathway dilation is assumed at about 80% of the lithostatic pressure. AV: -

3.4 Effingen Member

3.4.1 Basic geological characteristics of the Effingen Member

The Effingen Member of the Wildegg Formation comprises the majority of the Oxfordian strata (Malm, Upper Jurassic) in the candidate siting area Jura-Südfuss. In the area of interest, the Effingen Member is 170 to 260 m thick at depths of 410 to 720 m below ground (according to Nagra 2010, Appendix A3) and consists of interlayered calcareous marls to limestones, which are subdivided into three alternating sequences of (argillaceous) limestones and thinner (calcareous) marls (Kalkbankabfolgen, KBA 1 – 3). Based on the clay content from geophysical logs, Deplazes et al. (2013) have proposed the following lithostratigraphic facies for the Effingen Member (EFM), from top to bottom (Fig. 3-17):

- Gerstenhübel Beds sequence (GER): An alternating sequence of limestone layers and thin, clay-rich marls. Based on the proposed clay content correlation, the GER sequence has a regional extension with a thickness of 10 – 30 m in the eastern part of the siting region and not more than a few meters in the western part.
- Local alternating sequences of (argillaceous) limestones and thinner (calcareous) marls (KBax): There are several minor limestone sequences in the lower part of the EFF below the GER. The thickness is in the m range, the extension is quite uncertain.
- Sequences which are dominated by (calcareous) marls (Kalkmergelabfolgen) can be found between the KBAs. The KMAs above the GER show more similarities in the clay content pattern than the KMAs below the GER.

The characterization of hydrogeological properties of the Effingen Member is based on the hydrogeological interpretation of seismic investigations, geological mapping of outcrops, log interpretations and packer testing in the boreholes Schafisheim, Gösgen, Küttigen and Oftringen (Beauheim 2013). Log correlations suggest that the spatial variability of conductivity is governed (i) by the variability of porosity and clay content in the sedimentary structures (relevant for matrix flow) and (ii) by the occurrence of brittle tectonic features (relevant for fracture flow).

Brittle tectonic features such as fracture systems and faults represent potential water conducting features. In formations with very low matrix conductivity of the intact rock, the interconnected network of water conducting features exhibits the main body for pore water flow, controlling the effective hydraulic conductivity of the rock. The litho-stratigraphy of the Effingen Member, displaying alternating sequences of argillaceous limestones and calcareous marls, suggests very low hydraulic conductivity of the rock matrix. Hence, the density of the network of discrete tectonic features and the transmissivity of the individual fractures plays a predominant role in the assessment of the effective hydraulic properties of the formation as a whole.

Detailed structural interpretation of televiewer data, core inspections and complementary analyses of outcrop data from two quarries by Mazurek (2013b) provide an inventory of the discrete water conducting features (WCF) in the Effingen Member. A distinct clustering of the WCFs is observed in all boreholes, indicating high fracture frequencies along the KBA and GER sections. Furthermore, a comparison between the different boreholes reveals a general variability in fracture density. From televiewer analyses, Mazurek (2013b) reported only 10 structures in the cored borehole Gösgen KB5a (total length of cored borehole section in the Effingen Member: 89 m), whereas around 31 WCFs were identified in Oftringen, 45 in Gösgen SB2 and more than 130 in Küttigen (Table 3-4). Correspondingly the mean vertical distance between the discontinuities varies between 8.9 m (Gösgen KB5a) and 1.7 m (Küttigen).

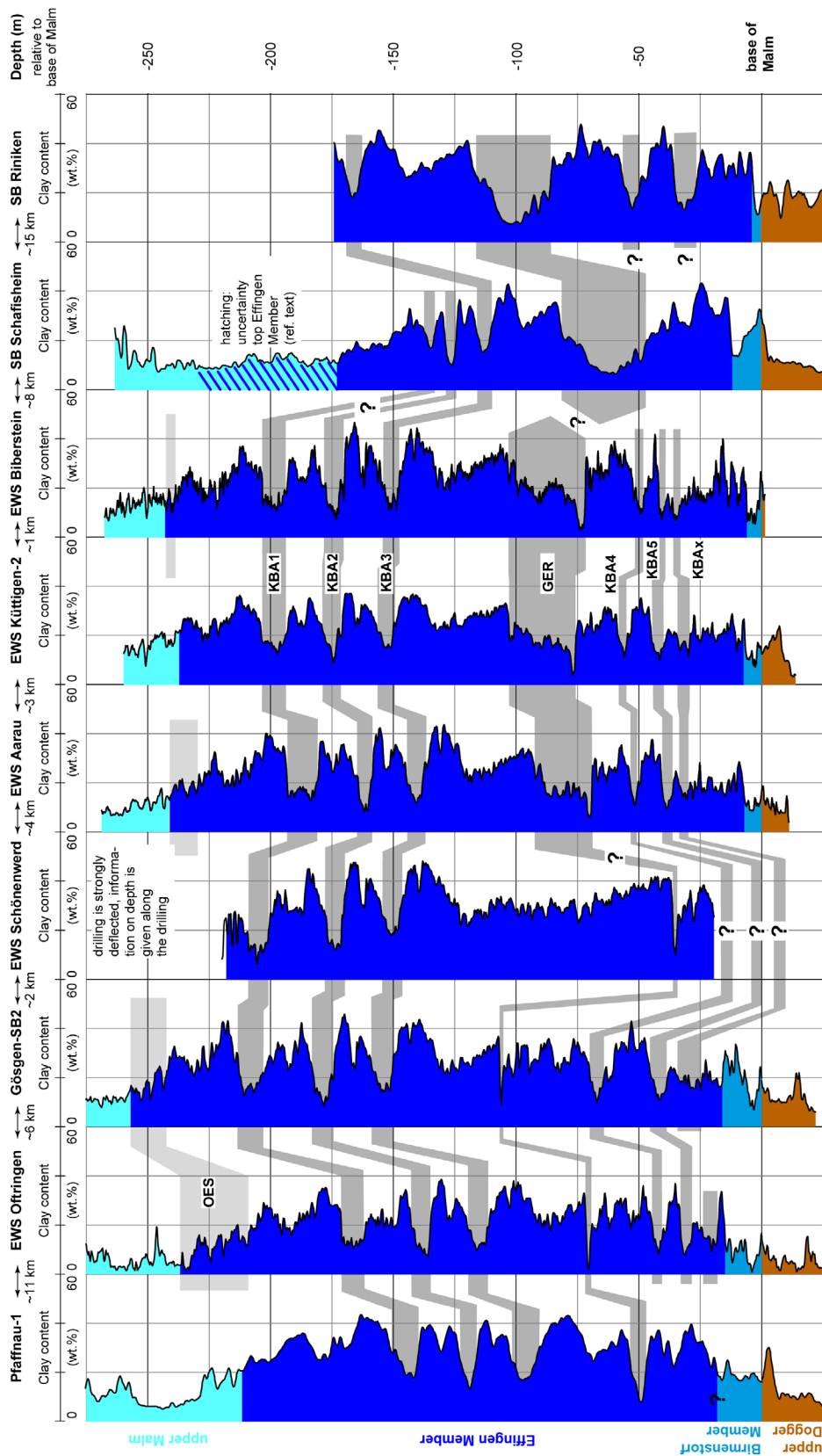


Fig. 3-17: Clay mineral contents of the Wildegge-Formation based on geophysical logs (Deplazes et al. 2013) between Pfaffnau and Riniken.

3.4.2 Gas-related characteristics of the Effingen Member

Gas transport in the Effingen Member is governed by sedimentological and structural features on scales ranging between kilometers and micrometers. Thus, geophysical logs in the Wildeggen-Formation (Fig. 3-17) indicate a distinct variability of clay content with large horizontal correlation lengths, suggesting a division of the Effingen Member into an alternating sequence of limestones (KBA) and calcareous marls (KMA). On the microscale, clear evidence is found for a distinct internal variability of the facies (Keller 2013, Appendix B). Structural analyses by Mazurek (2013b), drawing on core data from the boreholes Gösgen, Oftringen and Küttigen and outcrop mapping in the quarries Jakobsberg and Schümel, reveals a comprehensive inventory of discrete water conducting features. The regional field study by Madritsch & Hammer (2012) complements the structural data base with particular emphasis on large scale fault systems. The hydraulic significance of the sedimentary and structural features in the Effingen Member has been evaluated. Fig. 3-18 exhibits examples of property distributions in the Effingen Member on observation scales, ranging between hectometre and micrometer.

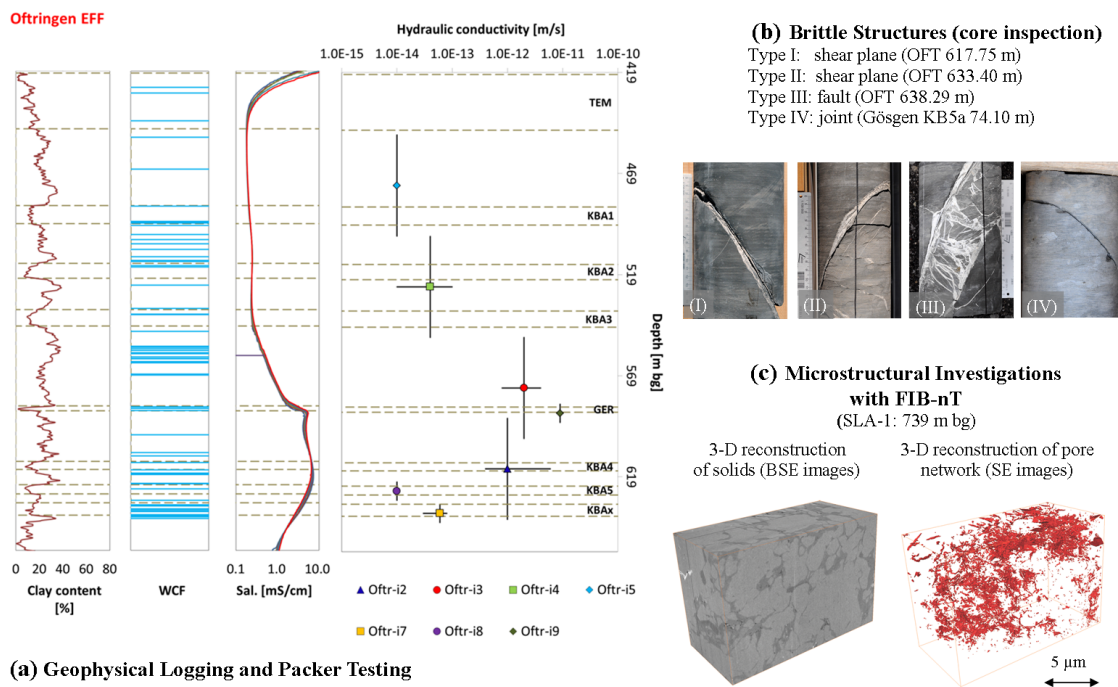


Fig. 3-18: Property distributions and relevant scales in the Effingen Member: (a) Clay profiles, structural logs, fluid logging and packer testing in the Oftringen borehole; (b) brittle structures derived from core inspection; (c) microstructural investigations on core samples from the SLA-1 borehole.

Keller (2013; Appendix B) performed microstructural analyses on a core sample from the Effingen Member in the Schlattigen 1 borehole (sample ID ZHAW; 738.70 – 739.02 m). The microstructural characterization was based on Focused Ion Beam nanotomography (FIB-nt) in combination with Broad Ion Beam imaging (BIB). Two sub-samples were subjected to a FIB-nt analysis by acquiring a sequence of cross sectional SEM images spaced evenly through a region of a bulk specimen, and reconstructing those two-dimensional images into a three-dimensional representation of the sampled volume. The spatial resolution of the reconstructed image was 20 nm (voxel size) and the investigated volume was $1275 \mu\text{m}^3$ (around $10 \times 10 \times 10 \mu\text{m}^3$). Fig. 3-19 displays the results of the microstructural analyses of sub-sample No. 2 by

decomposing the sample volume (Back scatter image in Fig. 3-19a) in a fraction of non-clayey grains (Fig. 3-19b), a clay fraction (Fig. 3-19c) and a pore network (Fig. 3-19d). The clay fraction fills the space between the non-clayey grains. The pore network displays only those pores with a pore radius > 20 nm, whereas smaller pores cannot be resolved (voxel size of the FIBnt analysis).

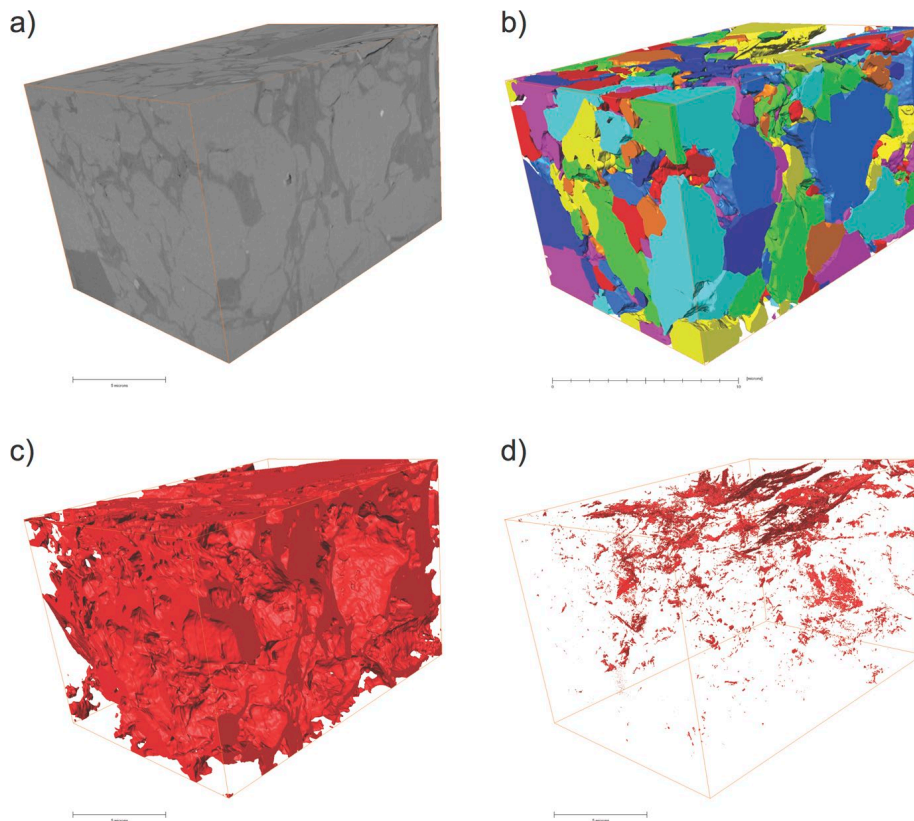


Fig. 3-19: Microstructural analysis of the rock matrix of Effingen Member by FIB-nt: (a) 3D reconstruction of the analyzed volume ($1270 \mu\text{m}^3$); (b) 3D reconstruction of the framework of the non-clayey grains. Colors are label colors of individual grains; (c) 3D structure of the clay matrix; (d) 3D reconstruction of the pore space with pore radii > 20 nm.

For the Effingen Member, mercury intrusion porosimetry (MIP) was performed on several a single core sample from the Schlattigen borehole (Ferrari et al. 2013), and on several samples from Oftringen and from Gösgen (Mazurek et al. (2013). The normalized pore-size distributions (PSD) from the MIP measurements of the different samples are shown in Fig. 3-20.

Water retention curves (WRC) were measured on a single core sample from the Schlattigen borehole (Ferrari et al. 2013). The water retention data of the Effingen Member along the drying and wetting path are plotted in Fig. 3-21, indicating significant hysteresis. The fitted WRCs indicate a relatively high capillary strength parameter, representative of the dominantly clay-silt matrix and not the potentially fracture KBA or KMA facies.

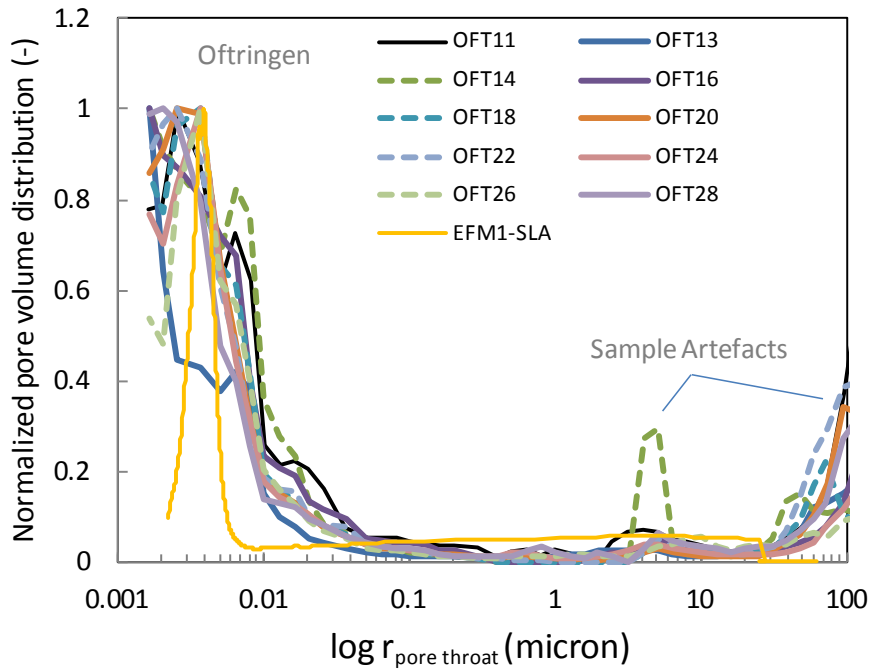


Fig. 3-20: Normalised pore size distributions of core samples from the Effingen Member determined by mercury intrusion methods. The drillcores were recovered from the Oftringen borehole (Mazurek et al. 2013) and from the Schlattigen borehole (Ferrari et al. 2013).

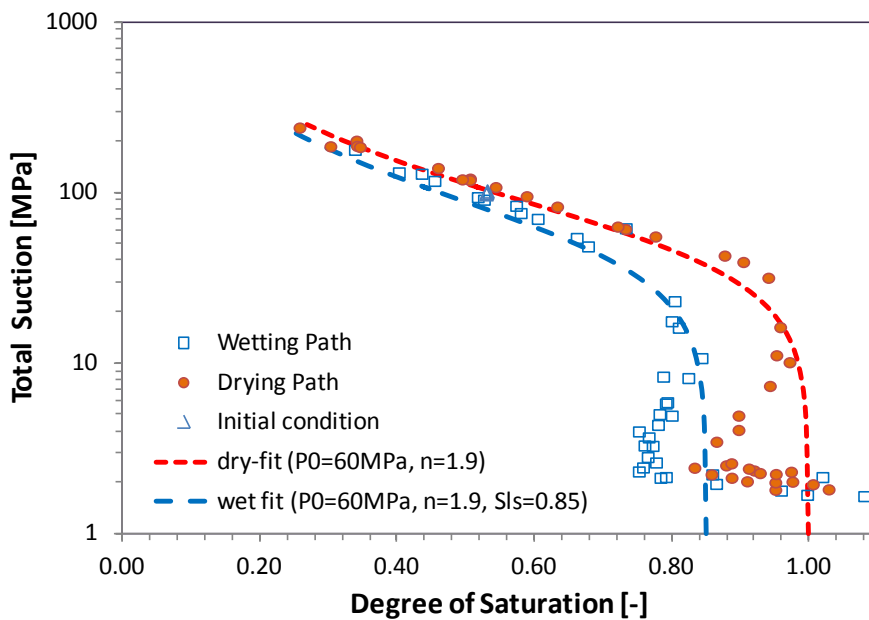


Fig. 3-21: Capillary pressure measurements (water retention curves) by stepwise desaturation and resaturation using a WP4c dew-point psychrometer and volumetric measurements using the progressive method on the deep Effingen Member core sample from the Schlattigen borehole measured by EPFL (Ferrari et al. 2013).

3.4.3 Reference parameters

Porewater flow in the Effingen Member is controlled by the spatial variability of hydraulic conductivity which is governed (i) by the variability of porosity and clay content in the sedimentary structures (relevant for matrix flow) and (ii) by the occurrence of brittle tectonic features (relevant for fracture flow). High interval transmissivities in packer tests are linked exclusively to test intervals in the argillaceous limestones (GER, KBA), suggesting that fracture flow dominates in those lithologies. In the calcareous marls (KMA), the interval transmissivities are generally low, which is regarded as a strong indication for matrix flow.

Different sets of reference parameters were specified for the clay-rich marls (KMA), the argillaceous limestones and calcareous marls (KBA), and the Gerstenhübel Beds (GER), based on the derived average hydraulic conductivities of the different sequences, which are summarized in Table 3-5. In terms of two-phase flow parameters, the WRC data are representative of the low-permeability KMA sequence, whereas the capillary-strength parameter is scaled to lower values for the higher permeable KBA and GER sequences.

Tab. 3-5: Reference values for the gas-related parameters of the Effingen Member in the siting region JS in Northern Switzerland (RV – reference value; AV – alternative value).

Parameter	RV	AV	Remarks
Undisturbed host rock			
Intrinsic permeability (KMA ⁽¹⁾ , KBA ⁽²⁾ , GER ⁽³⁾) k _⊥ [m ²]	1×10 ⁻²⁰ (1) 1×10 ⁻¹⁹ (2) 1×10 ⁻¹⁹ (3)	1×10 ⁻¹⁹ (1) 1×10 ⁻¹⁸ (2) 1×10 ⁻¹⁸ (3)	RV: corresponds to the reference value for hydraulic conductivity of Kalkmergelabfolgen (KMA), Kalkbankabfolgen (KBA) and Gerstenhübel-Schichten (GER). AV: corresponds to the value for hydraulic conductivity for the background fractures.
Anisotropy coefficient k /k _⊥	1	10	RV: no anisotropy assumed AV: effect of intermitted sand-beds expressed as anisotropic permeability
Capillary pressure - saturation relationship			Parametric model according to van Genuchten (Equ. 2-10)
Capillary strength 1/α [MPa] (no distinction between KBA ⁽¹⁾ , KMA ⁽²⁾ , GER ⁽³⁾)	60 ⁽¹⁾ 13 ^(2,3)	13	RV: derived from WRC measurements (EPFL) AV: mean value for 2D model used in Papafotiou et al. (2011); values for 2D heterogeneous field, scaled using Leverett)
Shape parameter <i>n</i> (no distinction between KBA, KMA and GER)	1.9	1.5	RV: derived from WRC measurements (EPFL) AV: value used in Papafotiou et al. (2011)
Relative permeability – saturation relationship			Parametric model according to van Genuchten/Mualem (Equ. 3-5 & 3-6) using the shape parameter <i>n</i> from the Pc-S curve
Residual water saturation S _{wr} [-]	0.25	0.1	RV: lower values than what expected based on MIP due to fracturing AV: assuming that nearly all pore water is mobile
Residual gas saturation S _{gr} [-]	0.00	-	RV: assuming all pore water is mobile
Water loss porosity [%]	8% ⁽¹⁾ 5% ⁽²⁾⁽³⁾	5%	RV: based on porosity measurements by Mazurek (2011) AV: corresponds to the lower value in matrix
Lower bound of fracture pressure [MPa]	σ _v = ρ _{rock} · g · z	-	RV: lithostatic pressure σ _v at repository level (ρ _{rock} = 2.5 Mg/m ³ , overburden z in m bg) AV: -
Threshold pressure for pathway dilation [% of σ _v]	80%	-	RV: the on-set of pathway dilation is assumed at about 80% of the lithostatic pressure. AV: -

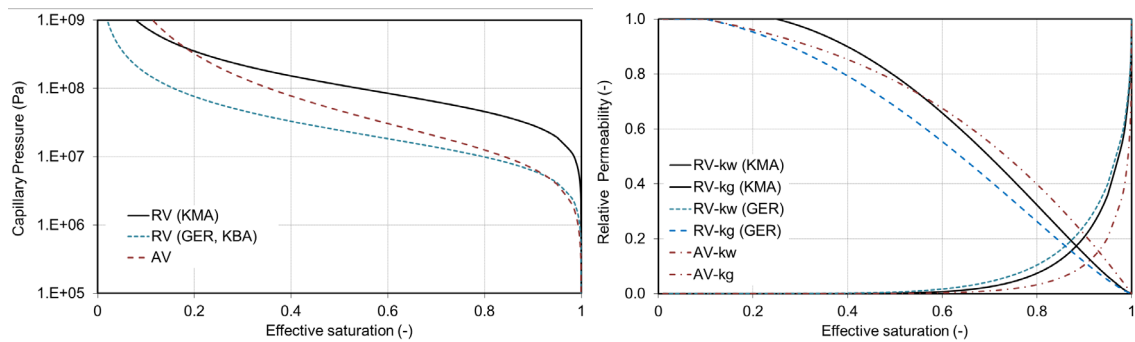


Fig. 3-22: Parametric models of capillary pressure and relative permeability k_r for water (w) and gas (g), representative for the Effingen Member (reference parameter values RV and alternative values AV).

3.5 Helvetic Marls

3.5.1 Basic geological characteristics of the Helvetic Marls

The Helvetic Marls in the Helvetic Zone of the Central Alps are being considered as a potential host rock for the geological disposal of L/ILW and the Wellenberg site in Kanton Nidwalden is the candidate siting region. The Wellenberg siting area is located in the contact zone between the Drusberg and Axen nappes, which were created by overthrusting during the Alpine orogeny. The Drusberg nappe is composed of Cretaceous and Cenozoic sediments (Palfris Formation and Vitznau marls, formerly designated as Valanginian Marls) and the Axen nappe of Jurassic, Cretaceous, and also Cenozoic sediments (Globigerina Marls and Schimberg Shales). Both tectonic units lie on top of a stack of parautochthonous and autochthonous sediments of Triassic and Jurassic age, themselves forming the cover of the crystalline basement of the Aare Massif.

The term "Helvetic Marls" refers to the Lower Cretaceous Palfris Formation and Vitznau Marls as well as the Tertiary Globigerina Marls and Schimberg Shales. The Palfris Formation consists of dark, silty-fine sandy, shaly clay marls, sometimes with isolated light limestone and lime marl beds and sometimes with such beds as interstratifications (limestone bed sequences). The Vitznau Marls consist of a clay-rich limestone/marl interstratification, with an upward transition into sand-rich limestones and marls. The Palfris Formation and Vitznau Marls form part of the base of the Drusberg nappe in Canton Nidwalden. The Globigerina Marls and Schimberg Shales are the uppermost Tertiary formations of the Axen nappe. The Globigerina Marls are dark, mica-bearing, silty clay marls, sometimes with lime marls. The Schimberg Shales are made up of grey, fine-sandy clay and lime marls.

In addition to the tectonic activities producing these nappes and associated disturbances, the Wellenberg siting region was also affected by valley cutting, notably through glacial erosion. Due to tectonic accumulation, the marl formations have a vertical thickness of more than 1000 m within the Wellenberg siting area.

Seven deep boreholes were drilled to investigate conditions at Wellenberg from 1990 to 1995. Hydraulic testing of portions of the Helvetic Marls was performed in all seven of the boreholes, wherein gas injection tests were performed in five boreholes for the determination of two-phase flow properties (Enachescu et al. 1995). Nagra (1997) provides an overall synthesis of all of the investigations undertaken in the Wellenberg siting area.

3.5.2 Gas-related characteristics of the Helvetic Marls

During the drawdown phase of packer testing in the Palfris formation, methane gas was observed quite frequently at the wellhead. With regard to the characterization of groundwater flow systems in the host rock, it is very important to know whether this gas is dissolved in groundwater under natural formation pressure or occurs as free gas phase. A classification of the packer tests was performed to assess the validity of the test results on the existence of a free gas phase in the host rock (Nagra 1997 and references therein). The evaluations revealed that only a few packer tests in the Palfris formation indicated the possibility of a free gas phase (12 of 141). For a quarter of tests it can be assumed that single-phase (water) conditions occur under natural formation pressure. The majority of the tests allowed no conclusive evidence for the presence of a free gas phase. This is essentially due to the fact that the packer tests were conducted primarily to determine transmissivity and hydraulic potentials.

Due to the limitation of the existing packer tests in determination of the occurrence of a free gas phase, a so-called gas-evidence test was performed in borehole SB4a (SB4a/s-VM11). The aim of this test was to assess the volume fraction of free gas in water-conducting features (WCFs) under local two-phase flow conditions, which is to be expected under in-situ pressure conditions in the system. For this purpose a borehole interval was selected, where a significant amount of gas was observed on previous packer tests (SB4a/s: 448 - 457.5 m along hole). A special sequence of hydrotests was conducted, which allows the identification and quantification of a free gas phase (Nagra 1997 and references therein). The detailed analyses of this test indicated the existence of a free gas phase in the test interval. However, the amount of free gas is very low and is probably only a small percentage (estimated about 3% of the pore space), and a value of more than 9% can practically be excluded.

In two test intervals in borehole SB4a/s gas threshold pressure tests were conducted (Test interval VM14 and VM16), which were used for the analysis of the two-phase parameter model and associated gas threshold pressure (Enachescu et al. 1995). Additional gas tests were performed in boreholes SB4 and SB2, the results of which are summarized in Table 3-6. The estimated two-phase flow parameters were based on the Brooks-Corey model together with the Grant model for the gas relative permeability.

Tab. 3-6: Results of two-phase analysis of hydrotests and gas threshold pressure tests in the investigation boreholes Wellenberg.

Bore-hole	Tests ²	Entry pressure P _d (MPa)	Parametric model	Residual saturation	
				gas	water
SB2	VM10	2.9	Grant	0 ¹	0.25 ¹
SB3	VM26, VM27, VM28	3.8 - 4.8	n.d.	n.d.	n.d.
SB4	VM2	n.d.	Grant, Brooks&Corey	0 ¹	0.34 - 0.79
SB4a/v	VM13, VM14	0.022 - 0.13	Brooks&Corey, Grant (VM13), Grant (VM14)	0 ¹	0.25 ¹
SB4a/s	VM11, VM14, VM16	0.1 - 2.6	Grant (VM11, VM16), Brooks&Corey (VM14)	0 - 0.03	0.07 - 0.25

n.d. - not determined
¹ - assumed values
² - Test intervals according to Nagra (1997) / Appendix A3-3.1 to A3-3.6
 Assumed pore size factor λ = 2

The derived entry pressures P_d were cross-plotted with the permeability values from conventional packer test sequences. Thus, a characteristic P_d-k correlation could be established for the WLB site (Nagra 1997):

$$P_o [Pa] = 1.31 \cdot 10^{-6} \cdot k^{-0.351} [m^2]$$

The cross-plotted data together with the empirical Wellenberg entry pressure – permeability relationship are presented in Fig. 3-23.

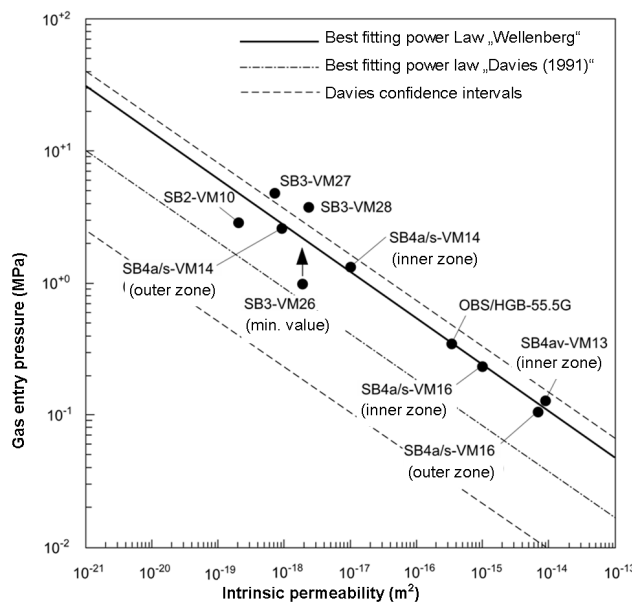


Fig. 3-23: Wellenberg relationship between air-entry pressure (P_d) and intrinsic permeability.

In the context of the Wellenberg geosynthesis project (Nagra 1997), the so-called Wellenberg K-model was developed, aimed at stochastic representation of the hydraulic conductivity distribution of the host rock on the scale of the siting area (Fig. 3-24). The Wellenberg K-model consists of the kriged K distribution and conditional realisations, leading to a realistic description of the distribution of hydraulic conductivity in the host rock and ensuring consistency with the results of the site investigations. Upscaling of the hydraulic properties for each borehole was quite critical for the final results. The volume for the effective hydraulic conductivity calculations was chosen as a cube with sides of 100 m and this was verified as a valid assumption, based on the conceptual model of the water-conducting features (block model) of the site (Fig. 3-24b). A fracture network approach ("Wellenberg DFN model") was applied to estimate K profiles along the boreholes, which allowed realistic assumptions about the size and distribution of the water-conducting features to be made (Fig. 3-24a). Further details of the Wellenberg K-model are found in Nagra (1997) and in the references therein.

An invasion-percolation approach (Wettstein et al. 2011) was applied to derive the effective water retention behaviour of the WLB fracture network on the block scale. For this, an entry pressure was assigned to each fracture of the stochastic fracture network by cubic scaling of the fracture transmissivities according to Eq. (2-23). A capillary pressure-saturation relationship was calculated by means of multiple Modified Invasion Percolation simulations of a gas phase invading $100 \times 100 \times 100 \text{ m}^3$ discrete fracture network realizations of the Wellenberg DFN model. The reference capillary pressure-saturation relationship was obtained by fitting Brooks-Corey functional relationship. Further details on the applied approach are found in Section 2.3.2 (see also Fig. 2-6).

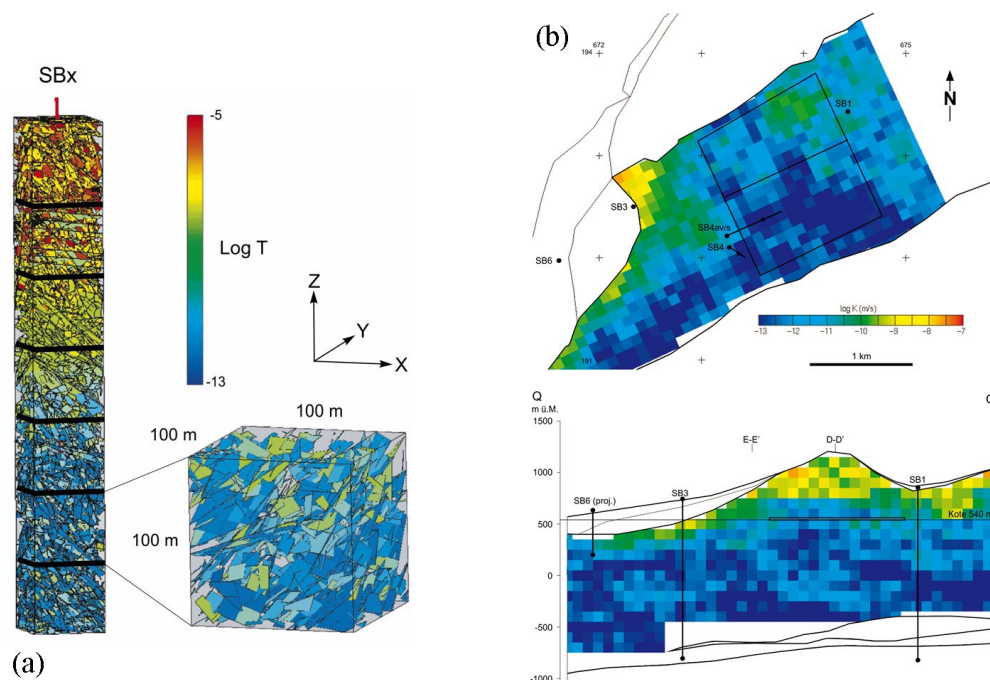


Fig. 3-24: The Wellenberg K-model: (a) Approach for the conversion of measured fracture transmissivities into effective hydraulic conductivities on the block scale ("T→K conversion") and (b) stochastic realisation of the K-distribution of the Helvetic Marls in the siting region Wellenberg (after Nagra 1997).

The assignment of Brooks-Corey air-entry pressure values $P_{d,i}$ to the individual blocks of the Wellenberg K-model was achieved through the application of well-established scaling laws, namely Leverett scaling (Eq. 2-19 / 2-24) and cubic scaling (Eq. 2-20), respectively. In Fig. 3-25 the corresponding P_d - k -relationships are presented and compared with the results of the in-situ tests (Table 3-6, Fig. 3-23), indicating that the slope of the cubic scaling matches the data better than the Leverett scaling. However, the cubic law may overestimate the gas transport capacity of the rock in the low permeability range, because the role of fracture flow decreases and matrix flow starts to take control. For this reason, the Leverett scaling has been selected for the definition of the gas related reference values of the Helvetic Marls.

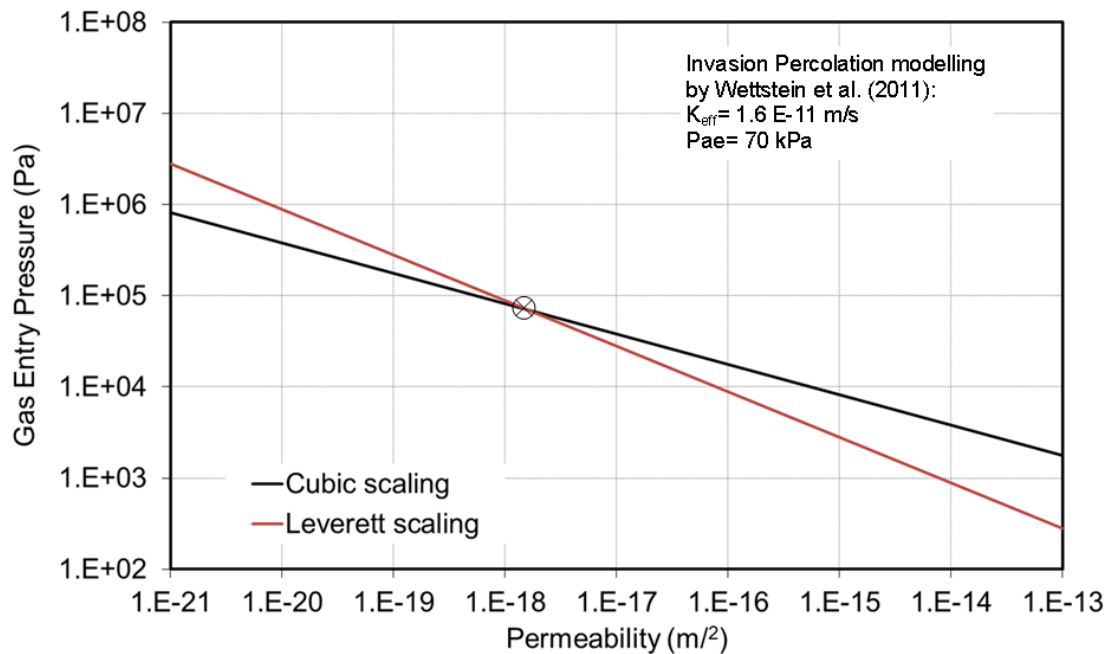


Fig. 3-25: Helvetic marl: P_d - k -relationships based on Leverett and cubic scaling and comparison with the results of the in-situ tests (see Table 3-6, Fig. 3-23). The relationships are based on the results of the Invasion Percolation simulations by Wettstein et al. (2011), using a DFN model of the WLB site with an effective block conductivity of $1.6E-11$ m/s and an effective entry pressure of 40 kPa.

3.5.3 Reference parameters

The Wellenberg K-model serves as a basis for the derivation of the gas related reference parameters of the Helvetic Marls in the siting region WLB. In summary, the approach consists of the following steps:

- Derivation of intrinsic permeability distributions from the Wellenberg K-model
- Derivation of the effective water retention behaviour of the WLB fracture network by an invasion-percolation approach (Wettstein et al. 2011).
- Derivation of the relative permeability functions for gas and water from the Brooks-Corey / Mualem functional relationship (Eq. 2-14a). The Grant model was used for the relative gas permeability (Eq. 2-17).

- Derivation of spatial variability of capillary pressure - saturation relationship from the Wellenberg K-model through Leverett and cubic scaling, respectively (Eq. 2-19 / 2-24).

Accordingly, two sets of gas related reference parameters have been elaborated (Table 3-7). The parametric models used for the capillary-saturation relationship and the relative permeability of the Helvetic Marls are shown in Figure 3-26.

Tab. 3-7: Reference values for the gas-related parameters of the Helvetic Marls for a L/ILW repository at the Wellenberg siting area in Central Switzerland (RV – reference value; AV – alternative value).

Parameter	RV	AV	Remarks
Helvetic Marls			
Effective permeability distribution k_i [m ²]	K-model WLB (Nagra 1997)		RV: corresponds to a repository depth 200 m below the regional discharge. AV: stochastic realisations of K distribution
Capillary pressure - saturation relationship			Parametric model according to Brooks-Corey Model
Capillary strength P_o [MPa]	derived via Leverett (RV) and cubic scaling (AV) from WLB K-model		RV, AV: Reference value P_o derived from WLB relationship ($k_o \rightarrow P_o$) according to Fig. 3-25.
Shape Parameter λ	0.7	-	RV: fitted curve for discrete fracture IP (Wettstein 2011)
Relative permeability – saturation relationship	B-C (Grant)	B-C	Parametric model according to van Brooks-Corey: RV: k_{rg} – Grant (high gas mobility in fractures) AV: K_{rg} – B-C (reduced gas mobility)
Residual water saturation S_{wr} [-]	0.5	0.1	RV: according to Nagra (1997) AV: assuming that most pore water is mobile
Residual gas saturation S_{gr} [-]	0.09	-	RV: according to Nagra (1997) AV: -
Water loss porosity [%]	8%	5%	RV: according to Nagra (1997) AV: assuming reduced porosity at the new repository level (200 m below regional discharge level)
Lower bound of fracture pressure [MPa]	20	-	RV: according to Nagra (1997) and considering the new repository level ($\rho_{rock} = 2.5 \text{ Mg/m}^3$) AV: -
Threshold pressure for pathway dilation [MPa]	16	-	RV: the on-set of pathway dilation is assumed at about 80% of fracture pressure. AV: -

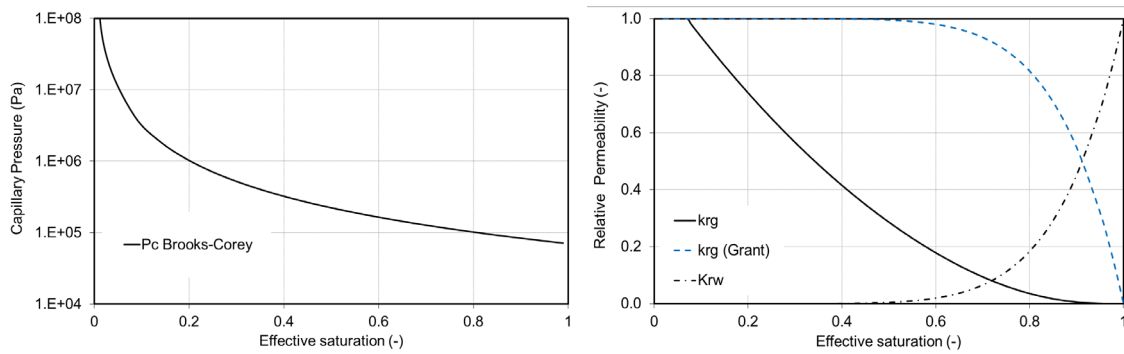


Fig. 3-26: Parametric models of capillary pressure and relative permeability k_r for water (w) and gas (g), representative for the Helvetic Marls in the siting region Wellenberg (reference parameter values only; the gas entry pressure corresponds to an effective block permeability of $k_{\text{mean}} = 1\text{E-}20 \text{ m}^2$).

3.6 Evidence from elsewhere

3.6.1 Additional evidence for Opalinus Clay and similar rocks from the EURATOM 7th Framework Project – FORGE (2010 – 2013)

The FORGE project (2010 – 2013) was a European project with links to international radioactive waste management organisations, regulators and academia, specifically designed to tackle the key research issues associated with the generation and movement of repository gasses. Of particular importance were the long-term performance of bentonite buffers, plastic clays, indurated mudrocks and crystalline formations. Comprehensive experimental data were acquired to reduce uncertainty relating to the quantitative treatment of gas in performance assessment. FORGE addressed these issues through a series of laboratory and field-scale experiments, including the development of new methods for up-scaling allowing the optimisation of concepts through detailed scenario analysis (Norris et al. 2013). Further details on the FORGE project and its outcomes can be accessed at <http://www/FORGEproject.org>.

Work packages 4 and 5 of the FORGE project were dedicated to the investigation of gas transport processes in the disturbed and intact host rock, respectively. New experimental data bases were derived from gas-related laboratory and in-situ experiments in Opalinus Clay, Calovo-Oxfordian, and Boom Clay. The experiments were modelled with numerical codes with advanced THM features. A brief summary of the experimental achievements is given below.

Water retention measurements

Villar & Romero (2012) derived water retention curves of Opalinus Clay samples from Mont Terri (boreholes BHT-1, BHG-D1) and compared their results with previous studies (Mont Terri: boreholes BVE-1, BE-99 to 102). The WRCs were determined under different conditions: total and matric suction, free volume or confined volume, wetting and drying paths. The data were matched with a van Genuchten parameter model. Results of the study are presented in Fig. 3-27. Overall, a good agreement is seen with the water retention curves, which were determined by EPFL and UPC (see Fig. 3-4).

Eventually, the authors drew the following conclusions:

- The marked scatter in the WRCs is partly attributed to difficulties in precise determination of the samples' dry density and degree of saturation evolution during the tests. As a consequence the derived degrees of saturation are characterized by relatively large uncertainty ranges. The delicate handling of the Opalinus Clay specimen was identified as the source of uncertainties in dry density determination.
- The tested core samples were recovered from different locations in the shaly facies of the Opalinus Clay. The scatter of the WRCs cannot be attributed to the internal variability of the shaly facies (e.g. variability in mineral content).
- Along the drying paths, the degrees of saturation tended to be higher when total suction was applied, however the reverse trend was observed for the water contents reached in the wetting paths. No clear difference was observed in the water retention curves obtained in oedometers under matric and total suctions, which indicates that the osmotic component of suction in Opalinus clay is not significant.
- Overall, the degrees of saturation were higher when suction was applied under vertical stress, which indicates that the water retention capacity was lower under 8 MPa vertical stress than under free volume conditions. Also, the samples showed hysteresis, i.e. the degree of saturation for a given suction was higher during a drying path than during a wetting path. The air entry values obtained (P_0 parameter) were between 6 and 34 MPa, and tended to be higher for the samples tested under stress, in drying paths and when total suction was used.

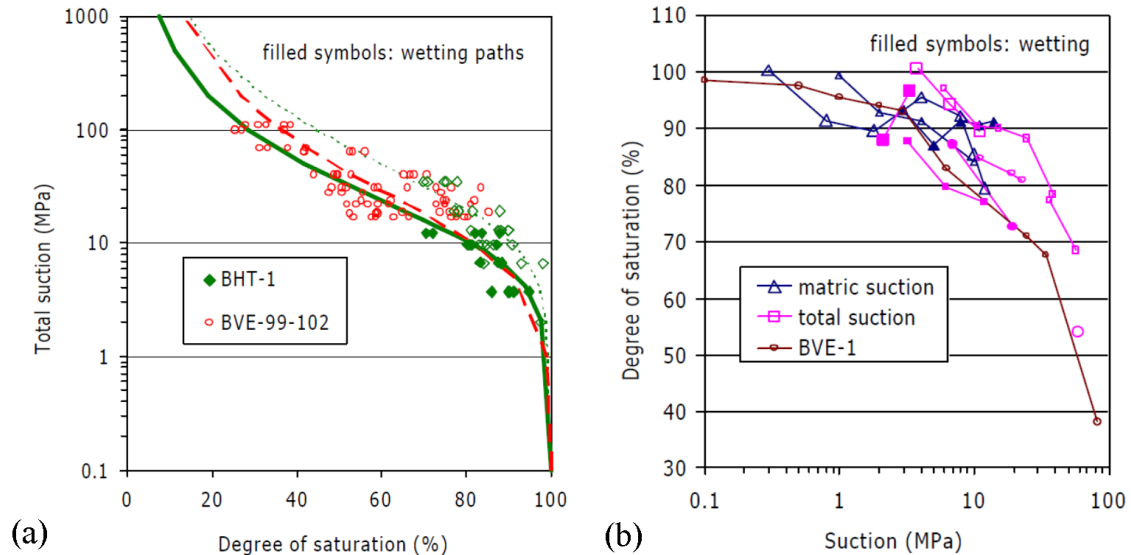


Fig. 3-27: Water retention measurements on core samples from Mont Terri (Villar and Romero 2012): (a) WRC along wetting/drying paths obtained under free volume conditions; van Genuchten curves are fitted to the different data sets. (b) WRC obtained under confinement (oedometric cell, 8 MPa vertical stress for samples from boreholes BHG-D1 and BHT-D1; constant volume conditions for samples BVE-1). The samples from borehole BVE-1 were subjected to drying paths applying total suction (for suctions above 3 MPa) or matric suction (for suctions below 3 MPa) while keeping their volume constant in the oedometer.

Gas/water permeability measurements

Villar et al. (2013) designed an experimental setup to measure gas permeability and gas breakthrough pressures in highly confined Opalinus Clay samples. The maximum gas injection pressures and confining pressures were 20 MPa and 30 MPa, respectively. Gas outflow was measured with a resolution of about 0.04 cm³/min (STP). A series of water/gas permeability tests was performed on rock samples from Mont Terri (borehole BDR-1) perpendicularly to the bedding plane. The authors derived an intrinsic permeability of 1E-20 m² from water injection tests. Furthermore, the breakthrough pressure of samples of degree of saturation 84±15% was higher than 18 MPa. The air entry value calculated from the mercury intrusion porosimetry tests was 28 MPa. The reported effective gas permeabilities (i.e. intrinsic permeability times relative gas permeability) ranged from 1E-20 to 1E-24 m². These results are broadly consistent with the results reported in Chapter 3.2.2. Nevertheless, it should be noted, that the authors point out the pilot character of experiments, particularly raising questions on mass flow resolution of the gas flowmeter.

Long-term water / gas injection tests have been performed by the British Geological Survey on the two rock samples (COx-1 and -2) from the Callovo Oxfordian, the proposed host rock for the French repository (Harrington et al. 2012, Harrington 2013). A pore water backpressure of 4.5 MPa was continuously imposed at the top of the sample through the central filter and an isotropic confining stress of 12.5 MPa was maintained during the entire experiment. The core specimen had an initial diameter of 54.4 mm and a height of 53.9 mm. The orientation of the sample was perpendicular to the bedding. More details about the experiment conditions can be found in Harrington et al. (2012). Hydraulic testing of sample COx-1 revealed a specific storage of ~ 6E-6 m⁻¹ and axial / radial permeabilities of ~ 2E-21 m² and ~ 5E-21 m², respectively. Helium injection occurred through the base of the sample by slowly increasing gas pressure in a series of steps (from 6.5 to 12 MPa) and then decreasing stages (from 12 to 7 MPa), while outflow evolution was measured at the top. Fig. 3-28 displays the slow, stepwise increase of gas pressure gradient across sample COx-1 from 6.5 to 12.0 MPa over a 600 day period. A first small emergent flux during the early stages of testing is observed before a spontaneous increase of discharge rate after 170 days, which is interpreted as evidences of major breakthrough. The breakthrough is signified by a spontaneous increase in discharge rate, ultimately leading to a quasi steady state flow rate.

Analysis of flux and pressure data indicates dynamic flow behaviour and time-dependent propagation of gas pathways across the specimen, signified by spontaneous changes in flux and guard ring pressure (Fig 3-28). Based on these observations, the excess gas breakthrough pressure for sample COx-1 was estimated to be ~ 2 MPa. In stark contrast, test COx-2 exhibits a gas entry pressure in excess of 6 MPa, which may suggest a marked variability of gas entry pressures in the Callovo-Oxfordian. Nevertheless, both tests reveal gas entry pressures of the rock, which are significantly below the confining stress of 12.5 MPa.

The test results of the laboratory experiments were modelled with an anisotropic hydro-mechanical model to take into account of couplings between the pathways aperture, permeability and air entry pressure and to explain the development of gas localised pathways (Harrington 2013). Following the idea of the "embedded fracture model" of Olivella & Alonso (2008), permeability and air entry pressure evolve in this model with strain in order to give an appropriate representation of single fractures embedded in a continuous finite element matrix. According to Harrington (2013) the use of the "embedded fracture model" allows to simulate the gas breakthrough phase with high gas fluxes and the pressure recovery phase in a more convincing manner than classical two-phase flow codes would do. However, the definition of the pre-existing fracture geometry is based on experimental evidences and remains arbitrary. Modelling with other geometry of the pre-existing fracture have shown the ability of the model

to reproduce localised pathways, but the set of parameters used must be adapted (Harrington 2013).

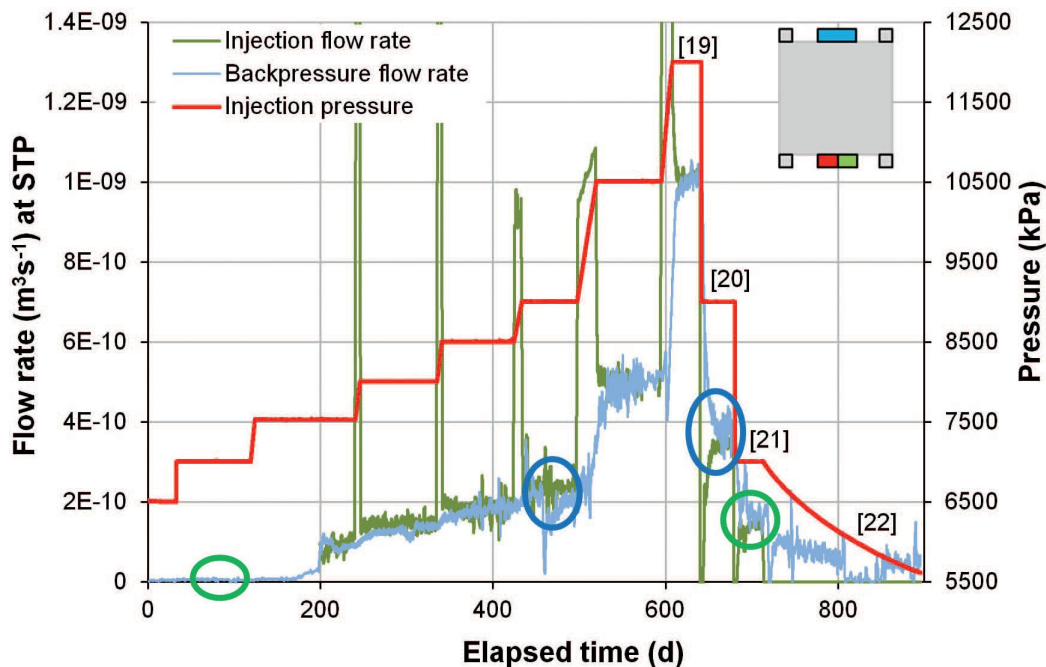


Fig. 3-28: Long-term gas injection test on the rock samples from the Callovo Oxfordian (Harrington et al. 2012): Gas flow rates at the injection and backpressure filters during the gas injection test COx-1. The large spikes in injection flux relate to the compression of the gas phase during constant flow rate tests. The blue and green circles highlight hysteresis in the flow response.

3.6.2 Complementary evidence from oil & gas industry

Argillaceous formations such as shales and claystones represent the major constituents of sedimentary basins (e.g. Hildenbrand & Urai 2003). They form seals for hydrocarbon accumulations, aquitards and chemical barriers. A detailed knowledge about the sealing characteristics is of particular interest in petroleum science (e.g. Ingram et al. 1997; Ingram & Urai 1999). Further evidence for gas transport in clay rich formations has been found in other areas such as natural gas storage and CO₂ sequestration. Benson et al. (2002) reviewed the safety results of underground storage in the United States as part of a comprehensive study considering CO₂ storage in deep geological formations. Another comprehensive literature study on gas storage and gas transport phenomena is given in Evans (2008).

Empirical investigations and phenomenological descriptions of gas flow through clay-rich seals were the subject of many geoscientific papers in the field of reservoir engineering (e.g. Clayton & Hay 1994, Zweigel et al. 2004). The extremely low intrinsic permeabilities of natural clay barriers (e.g. Neuzil 1994) and their high sealing capacity (Harrington & Horseman 1999) are controlled by the rock microstructure (a network of very small interconnected capillaries with pore neck radii down to the nm-range) and chemical interactions between minerals (e.g. smectite) and the permeating fluid.

The following paragraphs provide a brief survey of laboratory investigations on gas transport in low permeability formations from other geoscientific disciplines.

Water retention measurements / mercury porosimetry

In oil&gas industry mercury intrusion porosimetry (MIP) is the standard method for characterizing the capillary strength of rocks. A multitude of papers have been published, presenting the results of MIP for a variety of shales, claystones and tight sandstone formations. In the subsequent paragraph example results from a comprehensive study of the Mesaverde Tight Gas Sandstones from Western U.S. Basins are discussed. The corresponding test protocols and the interpretation procedures are described in great detail in a scientific report by Byrnes et al. (2009).

Fig. 3-29a presents the capillary pressure curves for selected samples with permeabilities in the range $2.5E-19 \text{ m}^2 - 2.24E-15 \text{ m}^2$. Only the tightest samples exhibit a permeability comparable to the reference permeabilities of the candidate host rock formations of the Effingen Member and 'Brown Dogger', which were 1 to 2 orders higher than the Opalinus Clay. The capillary pressure curve of the tightest sample ($2.5E-19 \text{ m}^2$) is comparable in shape and magnitude to the retention curves derived for the Opalinus Clay at Mont Terri (Fig. 3-4). Fig. 3-29b displays repeated drainage/imbibition curves for a low permeability sandstone ($7E-19 \text{ m}^2$) with a porosity of 5.9%. The capillary strength of the sample is in the order of several MPa. Furthermore, a distinct trapping of the invaded mercury is observed during the successive drainage/imbibition cycles, which can be seen as an indication for the poor connectivity of the pore network.

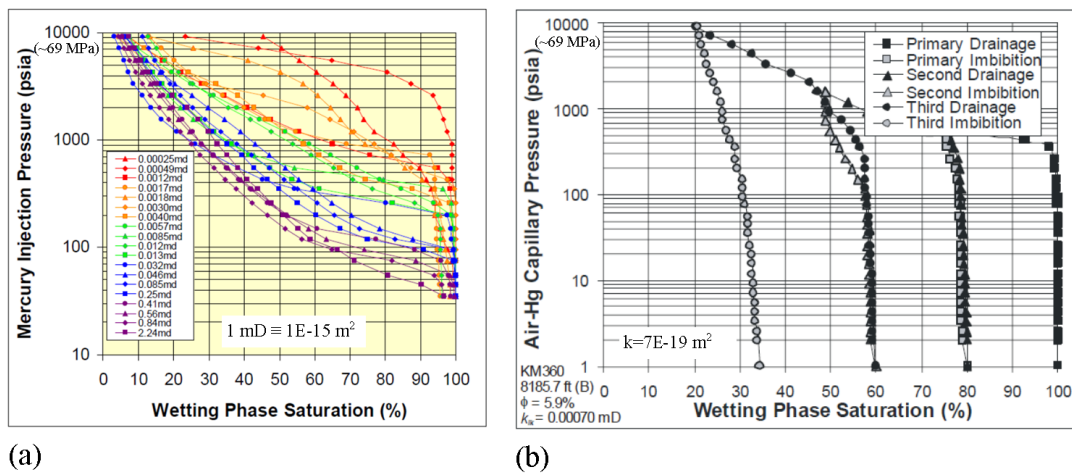


Fig. 3-29: Mesaverde Tight Gas Sandstones project (after Byrnes et al. 2009): (a) Air-mercury capillary pressure curves for selected samples ranging in permeability from 0.00025 mD to 2.24 mD (corresponding to $2.5E-19 \text{ m}^2 - 2.24E-15 \text{ m}^2$). The curves exhibit increasing threshold entry pressure and increasing "irreducible" wetting-phase saturation with decreasing permeability. (b) Example air-mercury successive drainage and imbibition capillary pressure curves.

The observed low mobility of both the wetting and the non-wetting phase leads Cluff & Byrnes (2010) to postulate the "Permeability Jail" concept for explaining typical two-phase (gas-water) relative permeability behavior in tight gas sandstone reservoirs. Although the basic behavior is typical of any two-phase flow system, where one fluid phase interferes with the ability of the other phase to flow freely, the combination of small pore throats in tight gas reservoirs with a reactive, polar, liquid phase (water) leads to unexpected behavior. The phenomena are observed only in very low permeability formations, typically with absolute gas permeabilities less than 50 micro-Darcies ($< 5E-17 \text{ m}^2$). According to Cluff & Byrnes the mobility reduction varies by rock type and specifics of the pore geometry, but roughly occurs typically in the 55%-80% S_w range. Tighter rocks tend to have broader S_w range in "Jail". Jail occurs because water is tightly held by capillary forces in the small pore throats of a tight gas sandstone, blocking the flow of gas through those throats, while at the same time the amount of free water connected through those same throats is extremely low and discontinuous over more than a few pore lengths. It is the absence of larger pore throats that are not completely blocked by pendular water that prevents the flow of gas through a rock in "Jail".

Gas entry pressure – permeability relationships

In petroleum engineering, the gas transport capacity of rock formations is often expressed in terms of gas entry pressure – permeability relationships. The gas entry pressure is usually derived from mercury intrusion porosimetry whereas permeabilities are derived from gas permeation experiments on dried samples. Corrections are made for slip flow of the compressible gas (Klinkenberg correction). A survey of data bases from different lithologies is given in the following section.

In the framework of the Mesaverde Tight Gas Sandstones project, Byrnes et al. (2009) cross-plotted a comprehensive data set of lithic sandstones and gas shales (Fig. 3-30a) and derived a characteristic power law relationship for the investigated formations:

$$P_{te}[psia] = 8.6 \cdot k^{-0.424} [mD] \quad \text{respectively} \quad P_{te}[Pa] = 0.026 \cdot k^{-0.424} [m^2]$$

Similar power law relationships have been derived for other lithologies. Davies (1991) compiled the results of two-phase flow laboratory experiments for shales, sandstones, anhydrites and carbonates in New Mexico and derived a functional relationship between the gas threshold pressure and the intrinsic permeability of the test samples:

$$P_{te}[Pa] = 0.56 \cdot k^{-0.346} [m^2]$$

Ibrahim et al. (1970) and Ingram et al. (1997) compiled oil industry data on the threshold capillary displacement pressure of low permeability rocks (see Fig. 3-30b), suggesting that the required gas pressure is often so large that it can approach the lithostatic stress (see also Horseman 2001). Their data set has been matched manually to the power law relationship with the following coefficients:

$$P_{te}[Pa] = 6.0 \cdot k^{-0.333} [m^2]$$

Pusch et al. (2006) provide a relationship for the low-permeability Rotliegend sandstones in Northern Germany:

$$P_{te}[MPa] = 10.6 \cdot k^{-0.693}[\mu D] \text{ respectively } P_{te}[Pa] = 4E - 6 \cdot k^{-0.693}[m^2]$$

The data sets by Byrnes et al. (2009), Davies (1991) and Pusch et al. (2006) suggest, that consistent and reliable relationships can be established for a given geological setting when the studied rock formations exhibit a comparable mineralogical and lithological composition. However, the comparison of different entry pressure – permeability relationships shown in Fig. 3-30 displays a huge spread, revealing a strong dependence of the entry pressures on mineralogy, lithology and other site specific characteristics, such as burial depth. It can be concluded, that the transferability of such empirical relationships is limited and cannot substitute site specific data compilations.

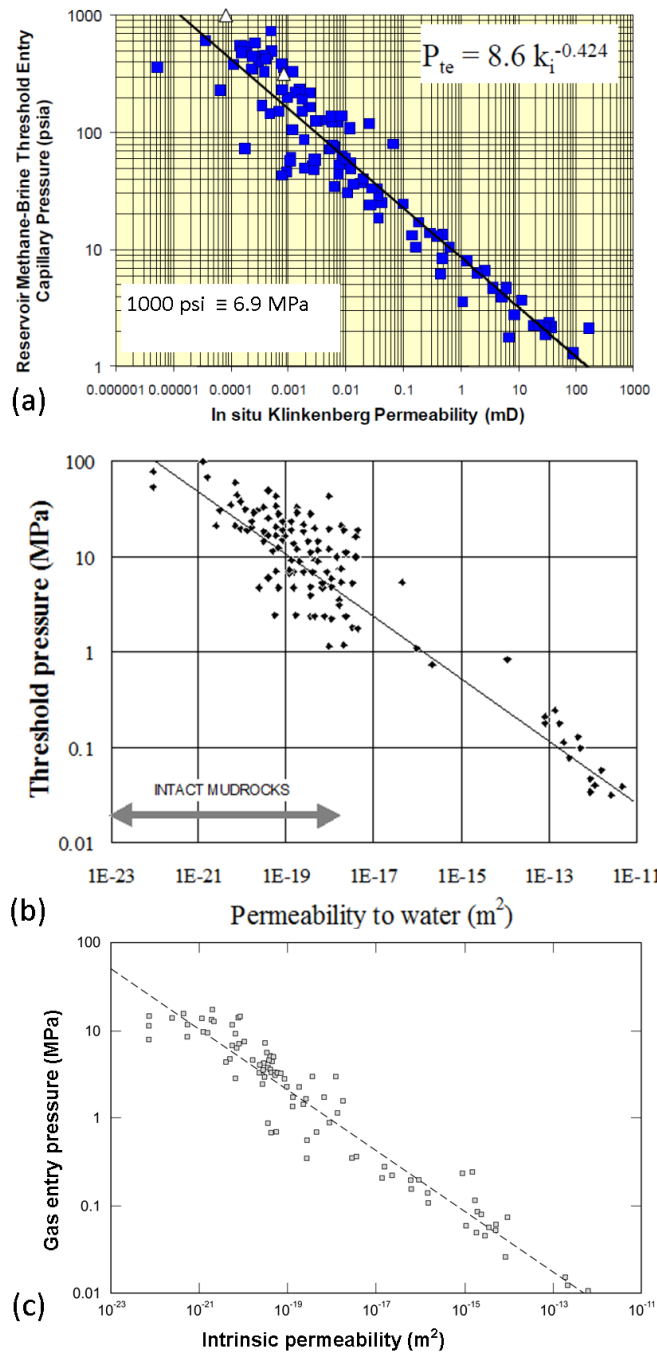


Fig. 3-30: Empirical threshold entry pressure – permeability relationships for various lithologies: (a) lithic sandstones (blue squares) and gas shales (open triangles) collected within the Mesaverde Tight Gas Sandstones project (from Byrnes et al. 2009). (b) wide range of undifferentiated lithologies, including shale, limestone and anhydrite, based on in situ measurements [from: Ibrahim et al. 1970; Ingram et al. 1997]. (c) shales, sandstones, anhydrites and carbonates in New Mexico (From: Davies [1991]).

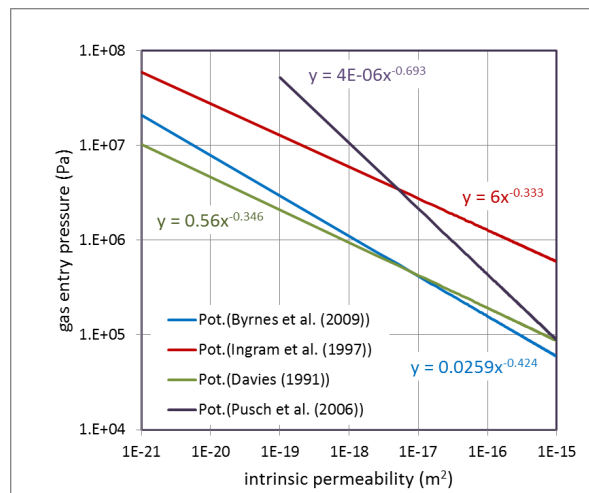


Fig. 3-31: Comparison of entry pressure – permeability relationships from different lithologies and different geological settings (Byrnes et al. 2009, Ingram et al. 1997, Davies et al. 1991 and Pusch et al. 2006).

4 Summary and Conclusions

For the provisional safety analyses as part of SGT - Stage 2 it is assessed how gas pressures develop in the backfilled underground structures of the geological repositories for SF/HLW and L/ILW due to material degradation/corrosion for different situations and if the gas pressures could affect the repository system. The assessment of the gas issue for safety requires a sufficient understanding of the gas related phenomena and processes in the geosphere and in the backfilled underground structures. Numerical simulations of gas pressure build-up and gas release after repository closure can provide valuable insight in role of gas generation. A key input for such model analyses of gas release from geological repositories in the candidate siting regions are estimates of gas related properties (and the uncertainty thereof), such as porosity, intrinsic permeability, relative permeability and capillary pressure. This report provides a synopsis of relevant gas related processes and phenomena together with gas related reference data sets for all host rock formations in the candidate siting regions.

4.1 Phenomenology of gas transport in the proposed host rock formations

Gas release paths through the host rock

The phenomenological description of flow and transport processes in porous media is closely tied to their fabric and the inventory of textural and structural features. In claystone formations such as the Opalinus Clay and the clay-rich sequences of the 'Brown Dogger' with clay contents > 40%, the swelling capacity of the rock ensures that brittle features (fractures) are tight, when burial depth exceeds several decameters. Thus, flow and transport processes are restricted to intrinsic porosity of the rock matrix (as long as pore pressure is significantly below lithostatic pressure; see also next section on gas transport mechanisms). Essentially, a network of connected pores in the range of micro- to nanometer defines the space, where flow of immiscible fluids can happen. As a consequence, gas transport processes in claystones are controlled by the spatial variability of their mineralogical and petrophysical properties. Laboratory investigations on undisturbed rock samples can provide reliable estimates of gas related properties.

In fractured, low-porosity rocks such as the Helvetic Marls and the calcareous sequences of the Effingen Member and the 'Brown Dogger', gas transport processes are limited to the more permeable fracture systems, whereas the rock matrix is essentially impermeable to gas (relative to the much larger gas flow rates in the fractures systems). Consequently, gas transport in fractured rock is essentially controlled by site specific characteristics such the density and connectivity of the fracture systems, the prevailing tectonic regime, in-situ stress and pore pressure conditions rather than by the intrinsic rock properties. Laboratory investigations on undisturbed rock samples may not be representative for the effective gas transport parameters on the repository scale; instead, they provide a lower bound for the gas transport capacity of the rock.

Gas transport mechanisms

Advection and diffusion of dissolved species represent the simplest transport mechanisms in a water-saturated porous medium. The propagation of the dissolved species is controlled by the water velocity and its extent is controlled by the hydrodynamic dispersion – a well-known aggregate representation of the mixing processes due to diffusion, Taylor dispersion and tortuosity. The dissolution of a gaseous species in water is described by Henry's law, the

diffusion of the dissolved gas is represented by Fick's law and the viscous losses of the pore water flow in the pore network are expressed by Darcy's law. Advection, diffusion and dissolution are well-established transport and retention mechanisms and corresponding parameter sets (intrinsic permeability, effective diffusion coefficients, solubility) with the corresponding uncertainty ranges have been elaborated for all host rock formations.

Two-phase flow conditions occur, when gas invades as a separate phase a water-saturated porous medium. The propagation of the gas front is controlled by the interaction of gravity, viscous forces and capillary forces. In fluid mechanics, flow of immiscible fluids is often described in terms of dimensionless numbers, namely the capillary number, the mobility ratio and - if gravity plays a role - the Bond number. Thus, scale dependence of the transport processes can be expressed in a universal way by introducing dimensionless length scales, which allows the transfer of the basic flow laws to other scales of interest. Broad experimental evidence has been established in experimental fluid mechanics with regard to the analysis and classification of immiscible fluid flow processes in porous media. Within the classification schemes of fluid mechanics gas transport processes in claystones and shales are characterized by very low capillary numbers and thus can be assigned to the flow regime of capillary fingering. Capillary fingering is associated with instable displacement of the wetting fluid (water) by the non-wetting fluid (gas), giving rise to phenomena such as migration, fragmentation and coalescence of the non-wetting fluid. The basic principles of two-phase flow and the corresponding equations of motion (water, gas) are well-established as well as the associated parametric models for the capillary pressure - saturation relationship and relative permeability. Reference values for the two-phase flow parameters (i.e. capillary strength / gas entry pressure, pore size factor, residual water / gas saturation) have been elaborated for all host rock formations together with the corresponding uncertainty ranges.

The degree of complexity increases, when two-phase flow processes occur in a deformable porous medium. Porosity is no more an intrinsic characteristics of the porous medium but depends on the total stress and the applied gas pressures. Thus the state of deformation, the porosity evolution and the corresponding change in permeability are defined by the actual stress path, acting on the porous medium. From a phenomenological point of view, gas transport in deformable porous media can be divided in two regimes, namely dilatancy-controlled gas flow ("pathway dilation") and gas fracturing.

Pathway dilation is associated with ductile fracturing. Gas-driven microfracturing leads to an increase of the porosity, which is accompanied by a detectable increase in intrinsic permeability and a change in the capillary pressure-saturation relationship. In the terminology of multiphase flow concepts, gas flow is yet controlled by visco-capillary forces - the main difference with respect to conventional two-phase flow is that the transport properties of the solid phase (rock permeability, relative permeability, capillary pressure relationship) can no longer be viewed as invariants since they depend on the state of deformation of the rock. Theoretical frameworks have been established in the fields of fracture mechanics and material research to conceptualize and model ductile fracturing in porous media. However, the application of such concepts on gas transport in shales and claystones is yet a subject of ongoing research. For simple stress paths, pragmatic solutions have been proposed in reservoir engineering literature, representing the functional relationship between deformation and permeability by pressure dependent permeability multipliers. The permeability multiplier approach has been adopted for modelling gas release in the geosphere, when gas pressure exceeds the threshold pressure for pathway dilation.

Gas fracturing is associated with the creation of brittle fractures. A brittle fracture is initiated quasi-instantaneously without precursory plastic deformation and propagates at about the velocity of a shear wave. Gas flow in such a macroscopic tensile fracture can be seen as a single-phase flow process. In a rock with low tensile strength (e.g., claystones), a macroscopic fracture develops only when the gas pressure build-up is rapid, i.e. when the combined effect of porewater displacement and formation of small-scale fractures (i.e. dilatancy) no longer counterbalances the gas production rate. The conceptual, theoretical and experimental framework for fracture propagation is well documented in standard reservoir engineering literature.

4.2 Reference parameters of the candidate host rock formations

A comprehensive set of geotechnical rock properties and constitutive relationships is needed for modelling gas transport processes in the host rock formations, comprising total porosity, intrinsic permeability, capillary pressure, relative permeability and the critical pressure for the on-set of pathway dilation. In the clay-rich host rock formations with typical clay contents > 40% (Opalinus Clay, clay-rich sequences of the 'Brown Dogger'), representative property estimates can be derived from laboratory tests on core samples. For the host rocks with low and moderate clay-content (Effingen Member, Helvetic Marls, sandy-calcareous sequences of the 'Brown Dogger'), laboratory tests on core samples can provide lower bounds for their gas transport capacity; as detailed in Chapter 4.1, complementary site specific knowledge is required concerning the hydraulic significance of the fracture systems to derive representative estimates of their effective gas transport properties. '

In the context of SGT – Stage 2, the experimental data base on gas related properties has been considerably expanded, particularly addressing the water retention behavior of the Opalinus Clay and the clay-rich sequences of the 'Brown Dogger'. Furthermore, advanced water/gas permeability test set-ups were developed, providing new insight in the hydro-mechanical coupled processes associated with transport and providing high quality data sets for benchmarking two-phase flow modelling approaches. '

Opalinus Clay

Two different sets of gas related reference parameters have been specified for the Opalinus Clay, namely for the shallow and deep repository configurations (shallow: 300 - 500 m bg.; deep: 500 – 900 m bg). The two reference parameter sets account for the fact, that the Opalinus Clay exhibits a depth dependence of porosity, permeability and capillary strength. The reference values for the shallow Opalinus Clay are given in Table 3-2, those of the deep Opalinus Clay are presented in Table 3-3. The reference parameters and the corresponding uncertainty ranges ("alternative values") are well-supported by the latest experimental data base from Mont Terri and from the Schlattingen SLA-1 borehole.

'Brown Dogger'

A set of reference parameters has been elaborated for the 'Brown Dogger', drawing mainly on laboratory tests with core samples from the clay-rich sequences (KMA) in the Schlattingen SLA-1 borehole. As expected, the derived two-phase flow properties are similar to those from the deep Opalinus Clay. The lower clay content of the sandy-calcareous sequences (SKA) gives rise to an enhanced permeability, which is evidenced by in-situ packer testing. No distinction between KMA and SKA is made with regard to the capillary strength and the pore size factor due to the lack of site specific experimental evidence. In this context, the comparison with evidence from elsewhere (Mesaverde gas shales, Rotliegendes sandstones; see Chapter 3.6) suggests a decrease of capillary strength with increasing permeability, implying that the capillary strength of the SKA could be slightly overestimated. The reference values and the corresponding uncertainty ranges ("alternative values") for the 'Brown Dogger' are given in Table 3-4.

Effingen Member

Gas transport in the Effingen Member of the siting area JS is not only controlled by the spatial variability of intrinsic permeability of the sedimentary structures, but also by the occurrence of brittle tectonic features and their site specific characteristics. High interval transmissivities in packer tests are linked exclusively to test intervals in the calcareous sequences (GER, KBA), suggesting that fracture flow dominates in those lithologies. In the calcareous marls (KMA), the interval transmissivities are generally low, which is regarded as a strong indication for matrix flow.

Thus, different sets of reference parameters were specified for the clay-rich marls (KMA), the argillaceous limestones and calcareous marls (KBA), and the Gerstenhübel Beds (GER), based on the derived average hydraulic conductivities of the different sequences, which are summarized in Table 3-5. In terms of two-phase flow parameters, the WRC data are representative of the low-permeability KMA sequence, whereas the capillary-strength parameter is scaled to lower values for the higher permeable KBA and GER sequences.

According to the acquired structural data bases from the siting area JS, the role of the fracture systems depends significantly on the local conditions. The high spatial variability of the fracture frequency with a distinct clustering suggests a high variability in the gas transport capacity of the fracture systems in the Effingen Member.

Helvetic Marls

Gas transport processes in the Helvetic Marls are largely restricted to the discrete water conducting features of the host rock, whereas the intact rock matrix is largely impermeable to gas (relative to the much larger gas flow rates in the fractures systems). A comprehensive characterization of the gas transport capacity of the Helvetic Marls in the Wellenberg siting area was carried out as part of the former Wellenberg site investigation programme. The determination of effective two-phase flow parameters was based exclusively on in-situ packer tests, accounting for the fact that laboratory experiments would represent the matrix properties only, whereas the dominating impact of the fracture networks can exclusively be addressed by in-situ tests. No complementary rock characterization programmes have been initiated since those former site investigations. The reference values for the gas related properties of the Helvetic Marls are given in Table 3-7.

5 References

- Artus, V., Noetinger, B. (2004): Up-scaling of two-phase flow in heterogeneous reservoirs: current trends. *Oil&Gas Sci – Rev. IFP* 59/2, pp. 185-195.
- Barenblatt, G.I., Entov, V.M. & Ryzhik, V.M. (1990): *Theory of fluids through natural rocks*. Kluwer Academic Publishing, Dordrecht.
- Bear, J. (1972): *Dynamics of fluids in porous media*. American Elsevier Pub., New York.
- Beauheim (2013): Hydraulic conductivity and head distributions in the host rock formations of the proposed siting regions. Nagra Arbeitsbericht NAB 13-13. Nagra, Wettingen, Switzerland.
- Benson, S.M., Hepple, R., Apps, J., Tsang, C.F. & Lippmann, M. (2002): *Lessons Learned from Natural and Industrial Analogues for Storage of Carbon Dioxide in Deep Geological Formations*. Lawrence Berkeley National Laboratory, Report No. LBNL-51170, Berkeley, United States.
- Biswal, B., C. Manwart, and R. Hilfer (1998), Three-dimensional local porosity analysis of porous media, *Physica A*, 255, 221-241.
- Bläsi, H.R., Deplazes, G., Schnellmann, M. & Traber, D. (2013): *Sedimentologie und Stratigraphie des 'Braunen Doggers' und seiner westlichen Äquivalente*. Nagra Arbeitsbericht NAB 12-51. Nagra, Wettingen, Switzerland.
- Bossart, P., Thury, M. (eds) (2008): *Mont Terri Rock Laboratory – Project, Programme 1996 to 2007 and Results*. Reports of the Swiss Geological Survey No. 3 – Swiss Geological Survey, Wabern, 2008.
- Bourg, I.C., Bourg, A.C.M. & Sposito, G. (2003): Modeling diffusion and adsorption in compacted bentonite: a critical review. *Journal of Contaminant Hydrology* 2003, 61, 293-302.
- Christensen, H. & Sunder, S. (2000): Current state of knowledge of water radiolysis effects on spent nuclear fuel corrosion. *Nucl. Tech.* 131, pp. 102-123.
- Bourgeat, A., Panfilov, M. (1998): Effective two-phase flow through highly heterogeneous media: capillary non-equilibrium effects. *Comput. Geosci.* 2, 191-215.
- Byrnes, A.P., R.M. Cluff, and J.C. Webb, 2009, *Analysis of Critical Permeability, Capillary and Electrical Properties for Mesaverde Tight Gas Sandstones from Western U.S. Basins*, U.S. Department of Energy Final Report Project # DE-FC26-05NT42660; 355 pgs, <http://www.kgs.ku.edu/mesaverde/reports.html>.
- Cluff, R.M., Byrnes, A.P. (2010): Relative permeability in tight gas sandstone reservoirs – the "permeability jail" model. SPWLA 51st Annual Logging Symposium, June 19-23, 2010.
- CSA (2006): *Storage of Hydrocarbons in Underground Formations Z341 Series-06*. Canadian Standards Association, Ontario, Canada.

- Clayton, C.J. & Hay, S.L. (1994): Gas migration mechanisms from accumulation to surface. *Bull. Geol. Soc. Denmark* 41, 12-23.
- Cole, T., Bidoglio, G., Soupioni, M., O’Gorman, M. & Gibson, N. (2000): Diffusion mechanisms of multiple strontium species in clay. *Geochim Cosmochim Acta* 2000, 63, 385-396.
- Coussy, O. (2004): *Poromechanics*, John Wiley, England.
- Croisé, J., Mayer, G., Marschall, P., Matray, J.-M., Tanaka, T. & Vogel, P. (2006): Gas Threshold Pressure Test Performed at the Mont Terri Rock Laboratory (Switzerland): Experimental Data and Data Analysis. *Revue de l’Institut Français du Pétrole*, 61 (No. 5, 2006).
- Davies, P. B. (1991): Evaluation of the role of threshold pressure in controlling flow of waste-generated gas into bedded salt at the Waste Isolation Pilot Plant (WIPP). Sandia Rep. SAND 90-3246.
- De Marsily, G. (1986): *Quantitative hydrogeology*. Academic Press, New York.
- Deplazes, G., Bläsi, H.R., Traber, D. & Schnellmann, M. (2013): *Sedimentologie und Stratigraphie Effinger Schichten*. Nagra Arbeitsbericht NAB 13-16, Nagra, Wettingen, Schweiz.
- Dewhurst, D.N., Yang Y. & Aplin A.C. (1999): Permeability and fluid flow in natural mudstones. In: Aplin et al. (Eds.): *Muds and mudstones. Physical and fluid properties*. Geol. Soc. Spec. Publ. 158.
- Didier M, Leone L, Greneche JM, Giffaut E, Charlet L. (2012): Adsorption of hydrogen gas and redox processes in clays. *Environ Sci Technol*. 2012 Mar 20;46(6).
- Domenico, P.A., Schwartz, F.W., (1990): *Physical and Chemical Hydrogeology*. John Wiley & Sons, New York.
- Dury, O. Fischer, U. & Schulin, R. (1999): A comparison of relative nonwetting-phase permeability models. *Water Resour. Res.* 35/5, 1481-1493.
- Evans, D.J. (2008): An appraisal of underground gas storage technologies and incidents, for the development of risk assessment methodology. BGS research report RR605, British Geological Survey, United Kingdom.
- Enachescu, C., Lavanchy, J.-M., Ostrowski, L., Senger, R., Wozniwicz, J. (1997): *Hydrological Investigations at Wellenberg: Hydraulic Packer Testing in Boreholes SB4a/v and SB4a/s - Methods and Field Results*. NTB 95-02, Nagra, Wettingen, Switzerland.
- Enachescu, C., Blümling, P., Castelao, A. & Steffen, P. (2002): *Mont Terri/GP-A and GS Experiments - Synth. Rep. Unpubl. Nagra Int. Rep. Nagra, Wettingen, Switzerland*.
- Felmy, A.R., Weare, J.H., (1991): Calculation of multicomponent ionic diffusion from zero to high concentration: 1. The system Na-K-Ca-Mg-Cl-SO₄-H₂O at 25° C. *Geochim. Cosmochim. Acta* 55, 113-131.

- Ferrari, A., Laloui, L. (2012): Advances in testing the hydro-mechanical behaviour of shales. In L. Laloui and A. Ferrari editors. *Multiphysical Testing of Soils and Shales*, pages 57-68, Springer, 2012.
- Ferrari, A., Favero, V., Manca, D., Laloui, L. (2013): Geotechnical characterization of core samples from the geothermal well Schlattingen SLA-1. Nagra Arbeitsbericht NAB 12-50, Nagra, Wettingen, Schweiz.
- Glass, R.J., Conrad, S.H., Yarrington, L. (2001): Gravity-destabilized non-wetting phase invasion in macro-heterogeneous porous media: Near-pore-scale macro modified percolation simulation of experiments. *WRR* 77(5), pp. 1197-1207.
- Glass, R.J., Yarrington, L. (2003): Mechanistic modeling of fingering, nonmonotonicity, fragmentation, and pulsation within gravity/buoyant destabilized two-phase/unsaturated flow. *WRR* 39(3).
- Grant, M.A. (1977): Permeability reduction factors at Wairakei. Proc. of the ASME/AICHE Heat Transfer Conference, paper 77-HT-52, Salt Lake City, Utah, USA.
- Gross, D., Seelig, Th. (2007): *Bruchmechanik*. Springer Verlag.
- Greenkorn, R.A., Kessler, D.P., 1972. *Transfer Operations*. McGraw-Hill, New York.
- Harrington, J. F., & Horseman, S. T. (1999): Gas transport properties of clays and mudrocks. In A. C. Aplin, A. J. Fleet, & J. H. S. Macquaker (Eds.), (158) (pp. 107–124). *Muds and mudrocks: Physical and fluid-flow properties*, London: Geological Society, Special Publications.
- Harrington, J.F., De La Vaissiere, R., Noy, Cuss, D.J., Talandier, J. (2012). Gas flow in Callovo-Oxfordian Clay (COx): *Mineralogical Magazine*, 76 (8) . 3303-3318.
- Harrington, J.F. (2013, ed): FORGE Milestone D4.24-R Summary report: Experiments and modelling of excavation damage zone (EDZ) behaviour in argillaceous and crystalline rocks (Work Package 4)1.
- Hartley, L.J., Holton, D. (2004): *CONNECTFLOW (Release 8.0) Technical Summary Document*, Serco Assurance Report (2004).
- Hassanizadeh, S.M., Celia, M.A., Dahle, H.K. (2002): Dynamic effect in the capillary pressure-saturation relationship and its impacts on unsaturated flow. *Vadose Zone J.* 1, 38-57.
- Hassanizadeh, S.M. and Gray, W.G. (1990): Mechanics and thermodynamics of multiphase flow in porous media including interface boundaries. *Adv. Water Resources* 14, pp 169-186.
- Helmig, R. (1997): *Multiphase Flow and Transport Processes in the Subsurface*. Springer Verlag, Berlin.
- Hildenbrand, A., Urai, J.L. (2003): Investigation of the morphology of pore space in mudstones –first results. *Marine and Petroleum Geology* 20, 1185-1200.
- Honarpour, M., Koederitz, L., Harvey, A.H. (1986): *Relative Permeability of Petroleum Reservoirs*. CRC Press, Boca Raton, Florida, United States.

- Horseman, S.T., Higgo, J.J.W., Alexander, J. & Harrington, J.F. (1996): Water, gas and solute movement through argillaceous media. Nuclear Energy Agency Rep. CC-96/1, Paris, OECD.
- Horseman, S.T., Harrington, J.F. & Sellin, P. (1999): Gas migration in clay barriers. *Eng. Geol.* 54, 139-149.
- Horseman, S.T. (2001) Gas migration through indurated clays (mudrocks). In: *Gas Generation and Migration in Radioactive Waste Disposal. Proc. of the NEA Workshop in Reims 2000, France.*
- Ibrahim, M.A., Tek, M.R., Katz, D.L. (1970): Threshold Pressure in Gas Storage. American Gas Association. Arlington, United States.
- Ingram, G.M., Urai, J.L. & Naylor, M.A. (1997): Sealing and top seal assessment. *Hydrocarbon Seals: Importance for Exploration and Production. NPF Spec. Publ. 7, 165-174, Elsevier, Singapore.*
- Ingram, G.M. & Urai, J.L. (1999): Top-seal leakage through faults and fractures: the role of mudrock properties. In: Aplin, A.C., Fleet, A.J. & Macquaker, J.H.S. (Eds.): *Muds and mudstones: Physical and fluid-flow properties. Geol. Soc. London Spec. Publ. 158, 125-136.*
- IUPAC (1997): *Compendium of Chemical Terminology. The Gold Book, Second Edition, McNaught, A. D. & Wilkinson, A., Blackwell Science, London.*
- Jackson, C.P., Hoch, A.R., Todman, S. (2000): Self-consistency of a heterogeneous continuum porous medium representation of a fractured medium. *Water Resour. Res.* 36(1), 189 (2000).
- Jahns, E. (2012): Bohrung Gösgen KB-5A – Felsmechanische Untersuchungen an Kernen der Effinger Schichten. *Nagra Arb. Ber. Nagra NAB 11-08, Wettingen, Schweiz.*
- Jacobs, B., Gelhar, L.W. (2005): Effective properties of two-phase flow in heterogeneous aquifers. *WRR 41.*
- Juanes, R., Spiteri, E.J., Orr Jr., F.M., Blunt M.J. (2006): Impact of relative permeability hysteresis on geological CO₂ storage. *Water Res. Res.* 42.
- Keller, L. M., L. Holzer, R. Wepf, and P. Gasser (2011), 3D Geometry and topology of pore pathways in Opalinus clay: Implications for mass transport, *Appl. Clay Sci.*, 52, 85–95.
- Keller, L.M., Schütz, Ph., Erni, R., Rossell, M.D., Lucas, F., Gasser, Ph., Holzer, L. (2013a): Characterization of multi-scale microstructural features in Opalinus Clay. *Microporous and Mesoporous Materials* 170 (2013) 83–94.
- Keller, L.M., Holzer, L., Schütz, Ph., Gasser, Ph., (2013b): Pore space relevant for gas permeability in Opalinus clay: Statistical analysis of homogeneity, percolation, and representative volume element. *Journal of Geophys. Res.: Solid Earth, VOL. 118, 1–14.*
- Kervévan, C., Azaroual, M., Durst, P., (2005): Improvement of the calculation accuracy of acid gas solubility in deep reservoir brines: application to the geological storage of CO₂. *Oil & Gas Science and Technology* 60, 357-379.

- Krooss, B.M., Leythaeuser, D., Schaefer, R.G. (1992): The quantification of diffusive hydrocarbon losses through cap rocks of natural gas reservoirs – a reevaluation. *Am. Assoc. Pet. Geol. Bull.* 76(3), pp. 403-406.
- Lanyon, G.W., Senger, R. (2011): A Structured Approach to the Derivation of Effective Properties for Combined Water and Gas Flow in the EDZ. *Transport in Porous Media* 90, pp 95-112.
- Lide, D. (ed), (2000): *Handbook of Chemistry and Physics*, CRC Press. Boca Raton, Florida.
- Lenormand, R., Touboul, E., Zarcone, C. (1988): Numerical models and experiments on immiscible displacements in porous media. *J. Fluid Mech.* 189, pp. 165-187.
- Lenormand, R., Zarcone, C. (1989): Capillary fingering - percolation and fractal dimension. *TIPM* 4, pp. 599-612.
- Luckner, L., van Genuchten, M.Th., Nielsen, D. (1989): A consistent set of para-metric models for two-phase flow of immiscible fluids in the subsurface. *WRR*, 25(19).
- Madritsch, H. & Hammer, P. (2012): Characterisation of Cenozoic brittle deformation of potential geological siting regions for radioactive waste repositories in Northern Switzerland based on structural geological analysis of field outcrops. Nagra Arbeitsbericht NAB 12-41. Nagra, Wettingen, Switzerland.
- Marschall, P., Croisé, J., Schlickenrieder, L., Boisson, J.Y., Vogel, P. & Yamamoto, S. (2003): Synthesis of hydrogeological investigations at the Mont Terri site (Phases 1 - 5). *Mont Terri Techn. Rep.* (2001-02), Geotechn. Inst. Ltd., Bern.
- Marschall, P., Horseman, S., Gimmi T. (2005): Characterisation of gas transport properties of the Opalinus Clay, a potential host rock formation for radioactive waste disposal. *Revue de l'Institut Français du Pétrole*, 60 (No. 1&2, 2005).
- Marschall, P., Lunati, I. (eds. / 2006): Gas migration experiments in a heterogeneous shear zone of the Grimsel Test Site. Nagra Technical Report NTB 03-11, Wettingen, Switzerland.
- Marschall, P., Lanyon, B., Gaus, I., Rüedi, J. (2013): FORGE D4-16: Gas transport processes at Mont Terri Test Site (EDZ and host rock)-Field results and conceptual understanding of self sealing processes. www.FORGEproject.org.
- Mazurek, M. (2011): Aufbau und Auswertung der Gesteinsparameter-Datenbank für Opalinuston, den "Braunen Dogger", Effinger Schichten und Mergel-Formationen des Helvetikums. Nagra Arbeitsbericht NAB 11-20, Nagra, Wettingen, Schweiz.
- Mazurek, M., Waber, H.N., Mäder, U.K., Gimmi, T., de Haller, A., Koroleva, M. (2013): Geochemical Synthesis for the Effingen Member in Boreholes at Oftringen, Gösgen and Küttigen. Nagra Tech. Ber. NTB 12-07.
- Mazurek, M. (2013a): Wasserführende Systeme im 'Braunen Dogger'. Nagra Arbeitsbericht NAB 13-12, Nagra, Wettingen, Schweiz.
- Mazurek, M. (2013b): Wasserführende Systeme in den Effinger Schichten. Nagra Arbeitsbericht NAB 13-50, Nagra, Wettingen, Schweiz.

- Méheust, Y., Lovoll, G., Maloy, K., Schmittbuhl, J. (2002): Interface scaling in a two-dimensional porous medium under combined viscous, gravity, and capillary effects. *Phys. Rev. E*. 66051603.
- Millington, R.J. and J.P. Quirk. Permeability of Porous Solids, *Trans. Faraday Soc.*, 57, 1200-1207, 1961.
- Mualem, Y. (1976): A new model for predicting the hydraulic conductivity of unsaturated porous media. *Water Resour. Res.* 12, 513-522.
- Muñoz, J.J., Lloret, A., Alonso, E. (2003): "VE" Experiment - Laboratory Report: Characterization of hydraulic properties under saturated and non saturated conditions Project Deliverable 4, EC contract FIKW-CT2001-00126.
- Nagra (1997): Geosynthese Wellenberg 1996 – Ergebnisse der Untersuchungsphasen I und II. Nagra Tech. Rep. NTB 96-01. Nagra, Wettingen, Switzerland.
- Nagra (2002): Projekt Opalinuston – Synthese der geowissenschaftlichen Untersuchungsergebnisse. Entsorgungsnachweis für abgebrannte Brennelemente, verglaste hochaktive sowie langlebige mittelaktive Abfälle. Nagra Tech. Rep. NTB 02-03. Nagra, Wettingen, Switzerland.
- Nagra (2004): Effects of post-disposal gas generation in a repository for spent fuel, high-level waste and long-lived intermediate level waste sited in Opalinus Clay. Nagra Technical Report NTB 04-06, Nagra, Wettingen, Switzerland.
- Nagra (2008): Vorschlag geologischer Standortgebiete für ein SMA- und ein HAA-Lager: Begründung der Abfallzuteilung, der Barrierensysteme und der Anforderungen an die Geologie / Bericht zur Sicherheit und Machbarkeit. Nagra Tech. Rep. NTB 08-05. Nagra, Wettingen, Switzerland.
- Nagra (2010): Beurteilung der geologischen Unterlagen für die provisorischen Sicherheitsanalysen in SGT Etappe 2. Nagra Technischer Bericht NTB 10-01. Nagra, Wettingen, Switzerland.
- Neuweiler, I., Attinger, S., Kinzelbach, W., King, P. (2003): Large-scale Mixing for Immiscible Displacement in Porous Media. *Transp. In Porous Media* 51, 287-314.
- Neuweiler, I., Sorensen, I., Kinzelbach, W. (2004): Experimental and theoretical investigations of drainage in horizontal rough-walled fractures with different correlation structures. *Advances in Water Resources* 27, pp. 1217-1231.
- Neuweiler, I., Cirpka, O.A. (2005): Homogenisation of Richards equation in permeability fields with different connectivities. *Water Res. Res.* 41.
- Neuweiler, I., Papafiotiou, A., Class, H., Helmig, R. (2010): Estimation of effective parameters for a two-phase flow problem in non-Gaussian heterogeneous porous media. *J. Contam. Hydrol.*
- Neuzil, C. E. (1994). How permeable are clays and shales? *Water Resources Research*, 30(2), 145–150.

- Noetinger, B., Zargar, G. (2004): Multiscale Description and Upscaling of Fluid Flow in Sub-surface Reservoirs. *Oil & Gas Science and Technology - Rev. IFP*, Vol. 59(2), 119-139.
- Norris, S., Lemy, F., del Honeux, C.-A., Volckaert, G., Weetjens, E., Wouters, K., Wendling, J., Dymitrowski, M., Pellegrini, D., Sellin, P., Johnson, L., Sentis, M. and Harrington, J. (2013): Synthesis Report: Updated Treatment of Gas Generation and Migration in the Safety Case, EC FORGE Project Milestone M68, 2013. www.FORGEproject.org.
- Oelkers, E.H., Helgeson, H.C. (1988): Calculation of the thermodynamic and transport properties of aqueous species at high pressures and temperatures: aqueous tracer diffusion coefficients of ions to 1000 °C and 5 kb. *Geochim. Cosmochim. Acta* 52, 63-85.
- Olivella, S., Alonso, E.E. (2008) Gas flow through clay barriers. *Géotechnique* 58, No. 3, 157-176.
- Olson, H.W. (1969): Simultaneous fluxes of liquid and charge in saturated kaolinite. *Soil Science Society of America Journal*, 33(3), 338-344.
- Ortiz, L., Volckaert, G., de Cannière, P., Put, M., Sen, A., Horseman, S., Harrington, J., Impey, M. & Einchcomb, S. (1997): MEGAS - Modelling and experiments on gas migration in repository host rocks. Final report: Phase 2. EUR 17453 EN. European Commission, Brussels, Belgium.
- Papafotiou, A., Senger, R., Alcolea, A., Lanyon, G.W., Ewing, J. (2011): Modeling approaches for evaluating the effects of heterogeneity on two-phase flow associated with the migration of waste-generated gas low-permeability formations. *Proceedings of the 14th International Conference on Environmental Remediation and Radioactive Waste Management, ICEM2011*.
- Poller, A., Mayer, G., Croisé, J. (2007) : Two-phase Flow Analysis of Gas Tests in Opalinus Clay Core Specimen: Complementary Analysis. Mont Terri TN 2007-01.
- Pruess, K., Oldenburg, C. & Moridis, G. (1999): TOUGH2 user's guide, 2., LBNL Report, LBNL-43134, Berkeley, CA., 1999.
- Pusch, G., Reitenbach, V., Nami, P., Meyn, R. (2006): "Experimental Investigations of two-phase flow properties under stress conditions and determination of petrophysical parameters for tight gas reservoirs". DGMK Forschungsbericht 593-9, Phase 2 "Simulation of the production behaviour of the hydraulically fractured wells in Tight Gas Reservoirs". DGMK, Hamburg, 139-194 (2006).
- Romero, E., Senger, R., and Marschall, P. (2012): Air injection laboratory experiments on Opalinus Clay. *Experimental Techniques, Results and Analyses: 3rd EAGE Shale Workshop, Barcelona, 23-25 January 2012*.
- Romero, E., Gómez, R. (2013): Water and air permeability tests on deep core samples from Schlattingen SLA-1 borehole. *Nagra Arb. Ber. NAB 13-51*. Nagra, Wettingen, Switzerland.
- Sarout, J., Esteban, L., Josh, M. (2013): Laboratory Characterisation of Cores (Geothermal Well Schlattingen SLA-1, Switzerland): Petrophysics and rock mechanics / physics. *Nagra Arb. Ber. NAB 12-47*. Nagra, Wettingen, Switzerland.

- Schlömer, S., Krooss, B.M. (1997): Experimental characterisation of the hydrocarbon sealing efficiency of cap rocks. *Mar. Pet. Geol.* 14(5), pp. 565-580.
- Schembre, J.M., Kavscek, A.R. (2006): Estimation of Dynamic Relative Permeability and Capillary Pressure from Countercurrent Imbibition Experiments. *Transp. Porous Media* 65, 31-51.
- Senger, R., Lanyon, B., Marschall, P., Vomvoris, S., Fujiwara, A. (2008): Numerical Modelling of the Gas Migration Test at the Grimsel Test Site (Switzerland). *Nuclear Technology* Vol. 164, Nov. 2008.
- Senger R, Romero E, Ferrari A, Marschall P (2014). Characterization of gas flow through lowpermeability claystone. Laboratory experiments and two-phase flow analyses. *Clays in Natural and Engineered Barriers for Radioactive Waste Confinement*, Montpellier, France, October 22–25, 2012. 4th International Meeting Andra (France).
- SHARC (2013): Third Annual Report of the SHARC Consortium. Nagra Project Report NPB 13-13. Nagra, Wettingen, Switzerland.
- Stauffer, F., Kong, X.-Z., Kinzelbach, W. (2009): A stochastic approach for air injection into saturated porous media. *Advances in Water Resources* 32, pp1180-1186.
- Swiss Federal Office of Energy (SFOE) 2008: Sectoral Plan for Deep Geological Repositories, Conceptual Part. Swiss Federal Office of Energy, Bern, Switzerland.
- Silin, D.B., Patzek, T.W. (2003): On Barenblatts model of spontaneous countercurrent imbibition. *Transp. Porous Media* 54(3), 297-322.
- Thury, M. & Bossart, P., eds. (1999): *Mont Terri Rock Laboratory: Results of the Hydrogeological, Geochemical, and Geotectonical Experiments performed in 1996 and 1997*. Berne, Switzerland, *Landeshydrologie und -geologie, Geologische Berichte* Nr. 23.
- Valko, P. & Economides, M.J. (1997): *Hydraulic fracture mechanics*. John Wiley, New York.
- Vargaftik, N.B. (1975): *Tables on the Thermophysical Properties of Liquids and Gases*, 2nd Ed., John Wiley & Sons, New York, NY, 1975.
- Van Genuchten, M.Th. (1980): A closed-form equation for predicting the hydraulic conductivity of unsaturated soils. *Soil Sci. Soc. Am. J.*, Vol. 44.
- Villar, M.V., Romero, J.R. (2012): Opalinus clay 2-phase flow parameters. FORGE Deliverable D5-14. www.FORGEproject.org .
- Villar, M.V., Romero, J.R., Martin, P.L. (2013): Opalinus clay gas induced fracturing. FORGE Deliverable D5-11. www.FORGEproject.org.
- Wagner, G., Birovlev, A., Meakin, P., Feder, J., Jossang, T. (1997): Fragmentation and Migration of invasion percolation clusters: Experiments and simulations. *Phys. Rev. E* 55, 7015.
- Walker, W.R., Sabey, J.D., & Hampton, D.R. (1981): *Studies of Heat Transfer and Water Migration in Soils*, Final Report, Department of Agricultural and Chemical Engineering, Colorado State University, Fort Collins, CO, 80523, April 1981.

- Wettstein, S.J., Wittel, F.K., Araújo, N.A.M., Lanyon, B., Herrmann, H.J. (2011): From invasion percolation to flow in rock fracture networks. *Physica A* 391 (2012) 264-277.
- Yang, Y.L., Aplin, A.C. (2010). A permeability – porosity relationship for mudstones. *Marine and Petroleum Geology* 27(8): 1692-1697.
- Zhang, C.-L., Rothfuchs, T. (2007): Moisture Effects on Argillaceous Rocks. In: *Proceedings 2nd International Conference of Mechanics of Unsaturated Soils* (editor T. Schanz), Springer Proceedings in Physics 112, p. 319-326.
- Zweigel, P., Lindeberg, E., Moen, A., Wessel-Berg, D. (2004): Towards a methodology for top seal efficacy assessment for underground CO₂ storage. *Geofluids* 7 (2), 112-122.

A Pore-space in 'Brown Dogger' and Opalinus Clay: homogeneity, percolation and RVE of porosity

Lukas M. Keller

ZHAW, Zurich University of Applied Sciences, 8400 Winterthur, Switzerland

Background and motivation

The bulk porosity and permeability of clay rich rock such as Opalinus Clay and the clay rich sequences of the 'Brown Dogger' depends on the amount of non-clayey grains dispersed in the clay matrix and ideally, the bulk porosity and permeability of pure shales decreases with increasing content of non-clayey grains (Revil and Cathles 1999). Hence, on a larger scale, permeability is likely controlled by the microstructure of the clay matrix. Permeability models relate permeability to geometric factors, which in case of the above two-component shale model is in particular the clay content, the geometric tortuosity or even the critical clay content (i.e. percolation threshold). Quantifications of these geometric factors based on real shale microstructures are rare. Applying synchrotron XCT to a Callovo-Oxfordian clay-rich rock sample and on the base of resulting 3D reconstructions of the clay matrix, Robinet et al. (2012) investigated the influence of the presence of non-clayey grains on diffusion anisotropy and tortuosity.

Here, we jointly applied synchrotron X-ray computed tomography (XCT) and a broad ion beam (BIB/SEM) approach to characterize the microstructure of rock samples with different clay contents. 3D reconstruction of the clay matrix microstructures were then analyzed by different methods in order to quantify the influence of the clay content on geometric factors affecting material transport. Focus is on the homogeneity, connectivity and percolation as well as on geometric tortuosity. In addition, the representative volume element (RVE) of the clay matrix and its dependence on clay content is addressed. The study gives also an idea of the representativity of XCT when applied to shales.

At present, it is demonstrated that homogeneity and the size of the RVE of the clay matrix depend on clay content. This result is better understood from the perspective of non-clayey grains. An increase in the amount of non-clayey grains is associated with an increase in the grain size spectrum, which combination results in an increase of geometric complexity and an increase of the sample size that must be analyzed to capture the geometric complexity of the sample.

Samples

The two core samples analyzed in this study are from the Schlattingen borehole SLA-1. Specimen BD-7 is a calcareous marl taken at a depth of 781m. Sample OPA-3 is an argillaceous marlstone taken at depth of 837 m. For both samples BD-7 and OPA-3 mineral contents were determined by X-ray diffraction analysis at University of Bern, Switzerland (Table A-1).

Tab. A-1: Mineral contents determined on the base of different methods.

Method	Sample	Area / Volume mm ² /mm ³	Quartz, Feldspar wt. %	Carbonates wt. %	Heavy minerals wt. %	Organic wt. %	Sheet silicates wt. %
XRD (Univ. of Bern)	BD-7 OPA3		21	33	6.1	0.1	43
			19	16	1.7	0.4	63
	Vol. %		Vol. %	Vol. %		Vol. %	
	19.7		30.9	3.1	-	46.3	
BD-7 OPA3		17.8	15.0	0.9	-	67.8	
BIB/SEM	BD-7 OPA3	0.30x0.26 0.31x0.27	Quartz, Feldspar Area %	Carbonates & Micas Area %	Heavy minerals Area %	Organic Area %	Clay matrix Area %
			21.5	23.5	0.6	0.5	53.9
			14.3	13	2.1	2.2	68.4
XCT	BD-7 BD-7 OPA3 OPA3	1.0x0.8x0.3 1.0x0.8x0.3 0.8x0.8x0.3 0.8x0.8x0.3	Quartz, Feldspar Vol. %	Carbonates & Micas Vol. %	Heavy minerals Vol. %	Organic Vol. %	Clay matrix Vol. %
			17.6	34.6	2.8	0.3	44.7
			9.6	30.5	4.5	0.4	55
			14.4	10	0.6	0.7	74.3
			14.3	12.1	0.6	3	70

Imaging methods

(a) Broad ion beam polishing and scanning transmission electron imaging

Rock cubes with edge length of about 5 mm were cut with the help of a saw with a thin (thickness of saw blade = 200 µm) diamond blade. Afterwards the cubes were lightly sanded to remove material that was damaged during sawing. In order to manufacture a smooth polished surface a 50 µm thick glass disc was glued on one side of the cube. This avoids the propagation of edge roughness onto the polished surface. Then, a cross-section was cut with a diamond saw. The surface of this cross-section was polished locally by using a Hitachi IM 4000 broad ion beam (BIB) instrument. The polished area was subsequently investigated by SEM using a FEI Quanta 200 FEG. The SEM was operated at low vacuum conditions and a conductive material did not coat the polished surface. Scanning Electron Microscope (SEM) imaging of BIB polished rock samples is used for a material characterization on the mm-scale (for comparison: typical sample size of the FIB-nt analyzed volume is a cube of 10-30 µm edge length). BIB polishing occurred at 6keV for 1.5 – 2.0 h.

(b) Synchrotron X-ray imaging

The measurements were performed at the synchrotron X-ray imaging station of the Helmholtz Centre Berlin for Materials and Energy (HZB, BAMline, Germany). The X-ray detection system consists of an optical set-up (Optique Peter) and of a PCO4000 CCD area detector with 4008×2672 pixels. A CWO scintillator screen with a thickness of $50 \mu\text{m}$ was used. The obtained pixel size was 438 nm . A W-Si multilayer monochromator with an energy resolution of about $dE/E = 10^{-2}$ was used to obtain a monochromatic X-ray beam. An X-ray energy of 19 keV was chosen for optimal image contrast. 1800 radiographic projections were taken for the reconstruction of the tomographic 3D data set. The exposure time was 3 s . All images were dark field and flat field corrected. A filter back projection algorithm was used for mathematical data reconstruction.

Results

Micro- to macro- scale pore structures based on BIB and SEM imaging SEM images on the mm-scale and SEM images at higher magnifications of the prepared samples are shown in Figures A-1, A-2, and A-3. The polished cross-sections are depicted in Figs. A-1a and A-2a. When compared to Opalinus Clay, the samples from the 'Brown Dogger' contained a high fraction of non-clayey mineral grains with a grains size $> 4 \text{ microns}$ (i.e. carbonates, quartz, pyrite, micas, organic material). The diameter of the largest grains is about 40 microns (Fig. A-4). Larger non-clayey grains frequently contained internal pores but the majority of pores were observed within the fine-grained matrix (Fig. A-1c-d). Therein, pores are related to geometric incompatibilities between clay mineral grains as well as small non-clayey grains (i.e. $< 4 \text{ microns}$). Visual inspection revealed a rather inhomogeneous grains size distribution within the fine-grained matrix.

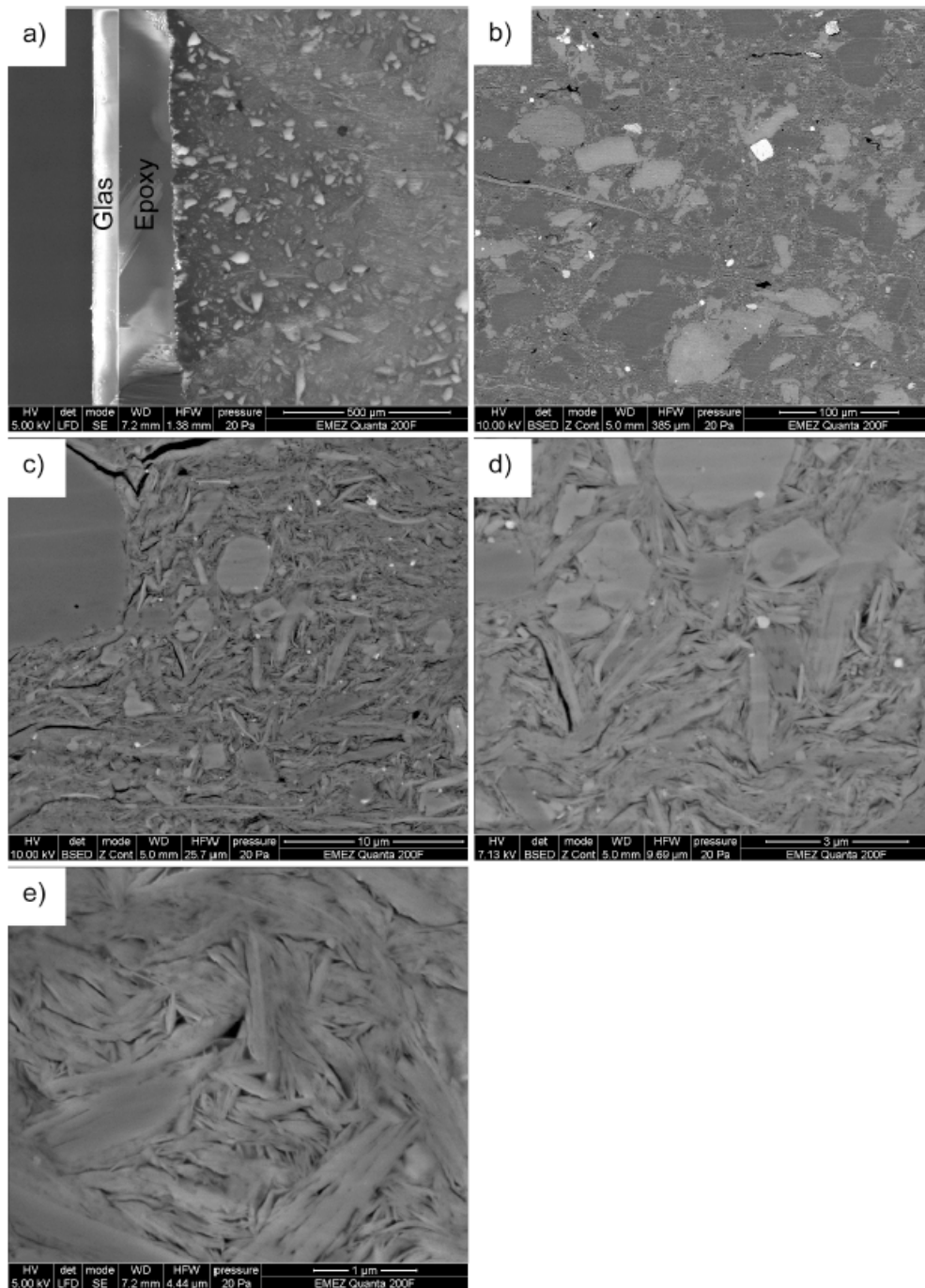


Fig. A-1: SEM images of 'Brown Dogger' BD-7 from the Schlattigen-1 borehole.

The images are related to one of cross-sections, which were polished by BIB perpendicular to bedding. The image plane is perpendicular to bedding (= parallel x-direction). a) SE image showing an overview of the polished area. Note the relief that surrounds the polished area. The use of a glass disc results in the formation of sharp edge, which avoids the propagation of sample edge roughness onto the polished surface. b) BSE image at low magnification shows the microstructure on the mm-scale. Larger non-clayey grains can be observed within a fine-grained matrix consisting predominately of clay minerals. c), d) and e) BSE images showing the fine-grained at increasingly higher magnifications.

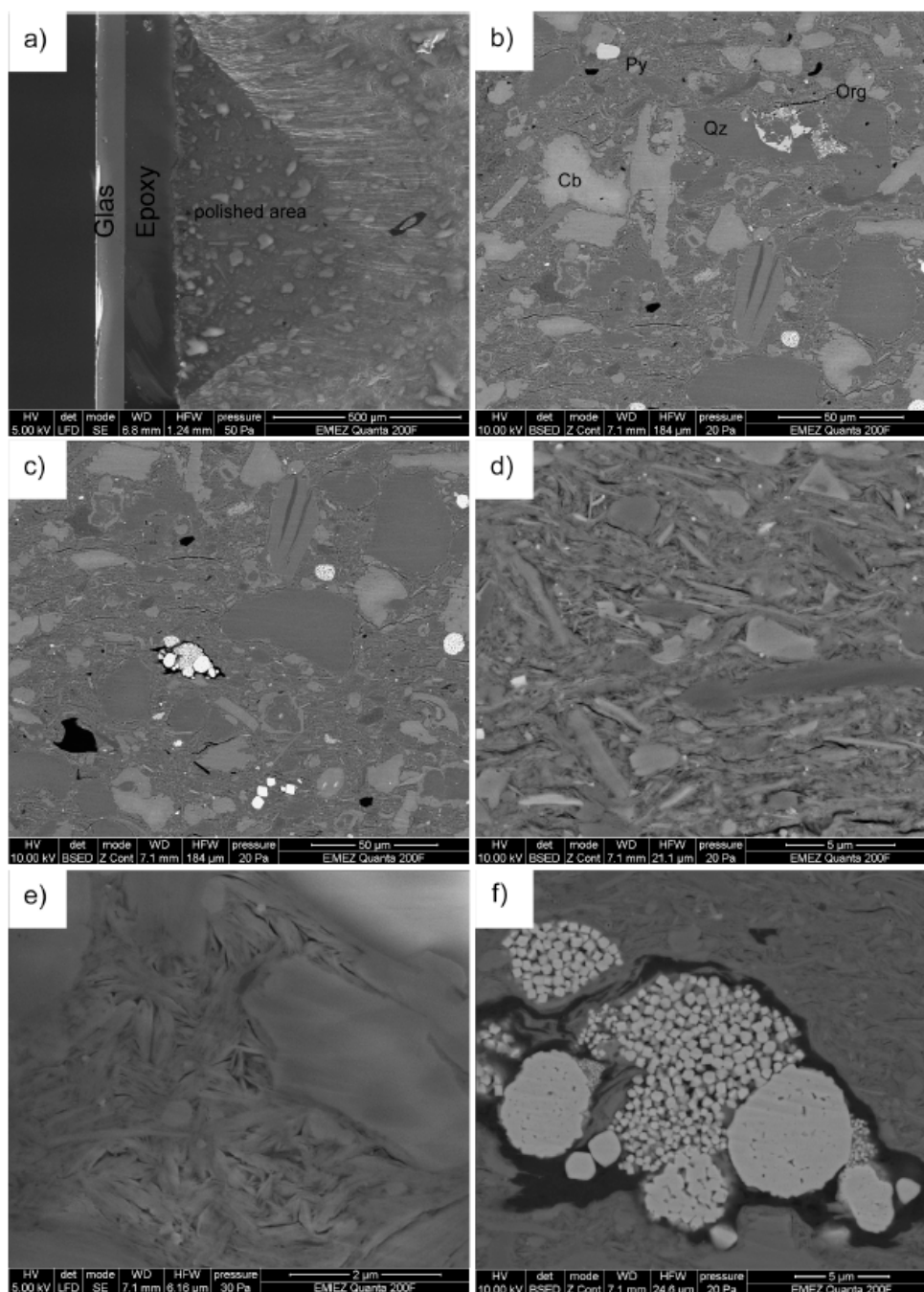


Fig. A-2: SEM images of 'Brown Dogger' BD-7 from the Schlattingen-1 borehole.

The images are related to one of two cross-sections, which were polished by BIB perpendicular to bedding. The image plane is perpendicular to bedding (= parallel x-direction). a) SE image showing an overview of the polished area. Note the relief that surrounds the polished area. The use of a glass disc results in the formation of sharp edge, which avoids the propagation of sample edge roughness onto the polished surface. b) and c) BSE image at low magnification shows the microstructure on the mm-scale. Larger non-clayey grains can be observed within a fine-grained matrix consisting predominately of clay minerals. Py = pyrite, Cb = carbonates, Qz = quartz, Org = organic. d) and e) BSE images showing the fine-grained at increasingly higher magnifications. Clay flakes are rather poorly aligned, which results in the formation of numerous pores. f) Pyrites surrounded by organic material (black).

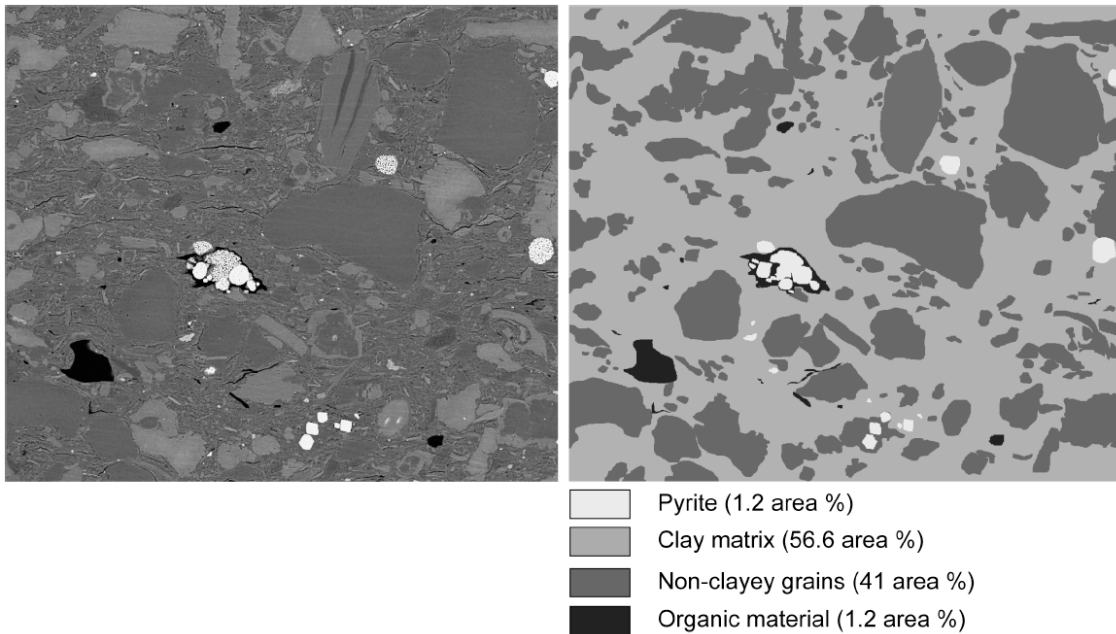


Fig. A-3: 'Brown Dogger' BD-7 from the Schlattingen-1 borehole: (left) BSE images (scale bar see Fig. A-2c) that was segmented. (right) After image segmentation, the image shows the structure of major components at this microstructural level.

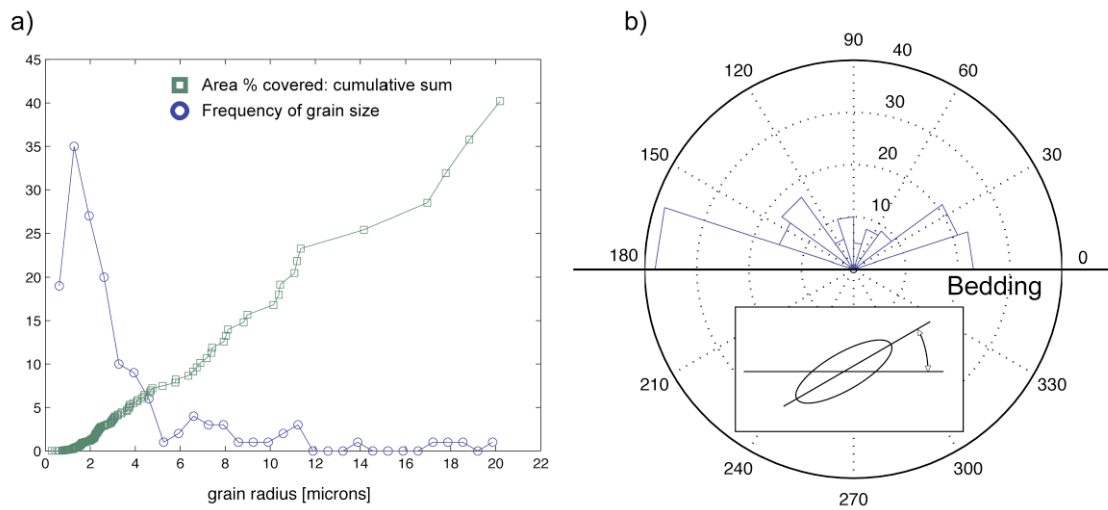


Fig. A-4: 'Brown Dogger' BD-7 from the Schlattingen-1 borehole:

Results related to an analysis of comparable larger non-clayey grains. a) Plot shows the frequency of grain sizes and the area covered by the grains. In the terms of volume, a few larger grains account for the majority of the non-clayey material present. b) Rose diagram showing the orientation of the long axis of an ellipse that was fitted to the grains. Orientation is given with respect to the bedding plane. The long axis tends to be aligned parallel to bedding.

Modal amounts of major components: OPA-3 versus 'Brown Dogger' BD-7

Figure A-5 depicts BSE images showing the 2D microstructures perpendicular to bedding on the hundreds of micron scale.

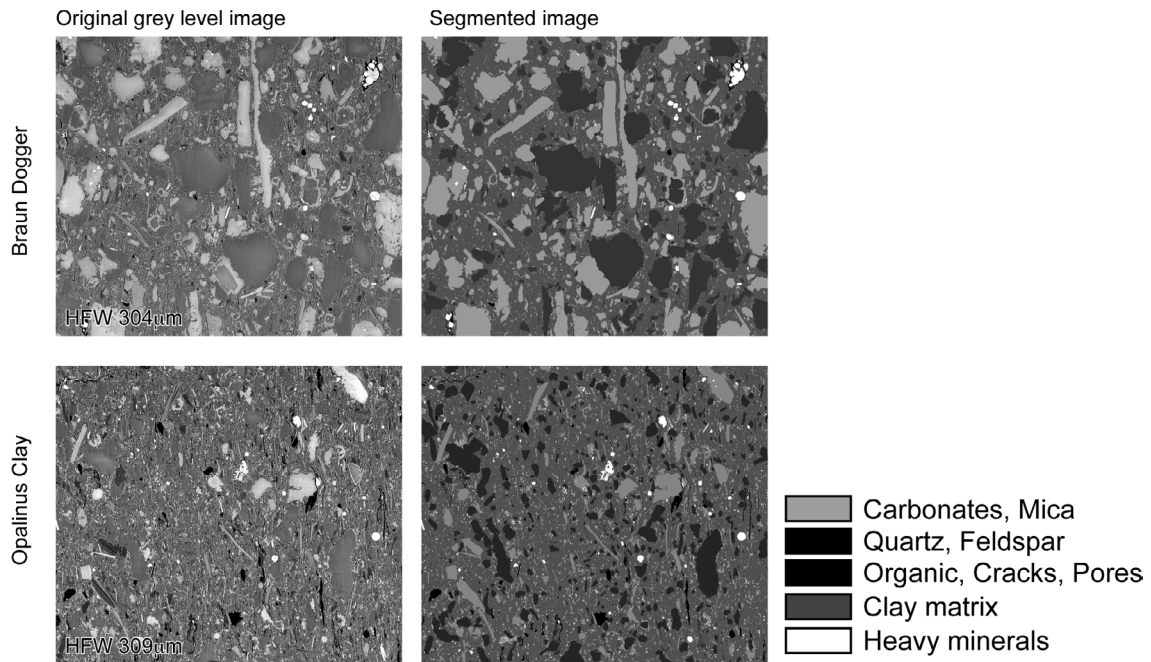


Fig. A-5: Left column are BSE images of shale rocks with different clay contents. Bedding is vertical. Right columns are the corresponding segmented images. (HFW = horizontal field width).

BD-7 and OPA-3 differ in clay content and grain size of non-clayey mineral grains. Based on the segmented XCT image stacks, Figure A-6 shows 3D reconstructions corresponding to major constituents. Generally, non-clayey components in OPA-3 are finer-grained when compared to sample BD-7. Grains-size distributions calculated for carbonates and quartz indicate a larger fraction of large carbonate grains in BD-7 when compared to OPA-3. Quartz grains in the two samples have a similar grain size spectrum (Fig. A-7).

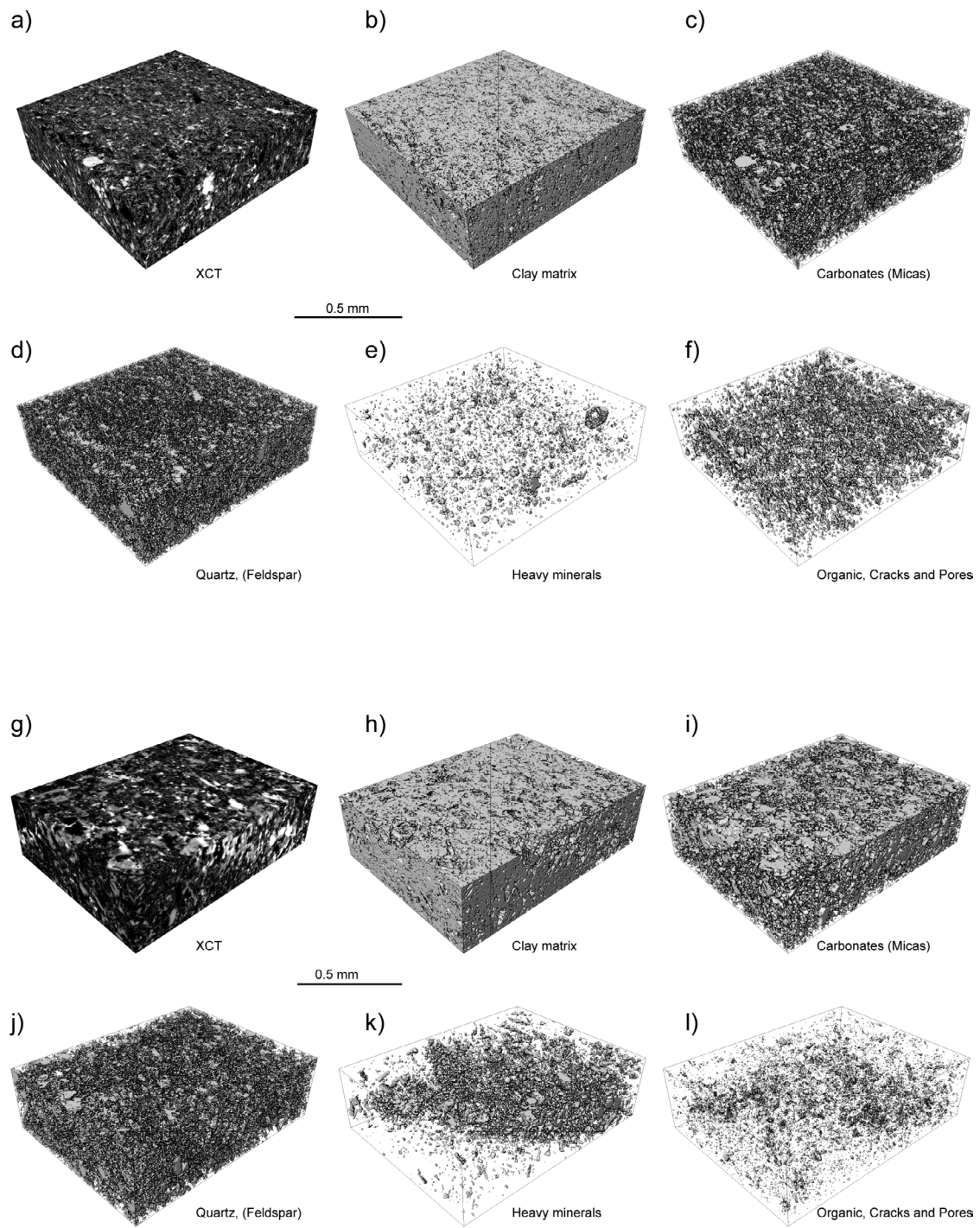


Fig. A-6: Reconstructed microstructures of major components. (a)-(f) sample OPA-3 and (g)-(l) sample BD-7. (a) and (g) are 3D reconstruction of the analyzed volume. (b)-(f) and (h)-(l) are microstructures corresponding to indicated components.

Table A-1 compares the mineral content obtained on the base of different methods. Regarding the relative content of major components, XCT and XRD yielded similar results but with systematic discrepancies regarding the absolute content of components. Regarding BD-7 carbonate contents determined by the two methods are in good agreement. For OPA-3 XCT yielded somewhat lower carbonate contents, which may be related to the presence of small-undetected carbonate grains on the clay matrix (see also Robinet et al. 2012). Tectosilicate (i.e. mainly quartz) content is systematically lower when estimated on the base of XCT, which is likely related to limited image contrast between tectosilicate grains and clay matrix (see also Robinet et al. 2012).

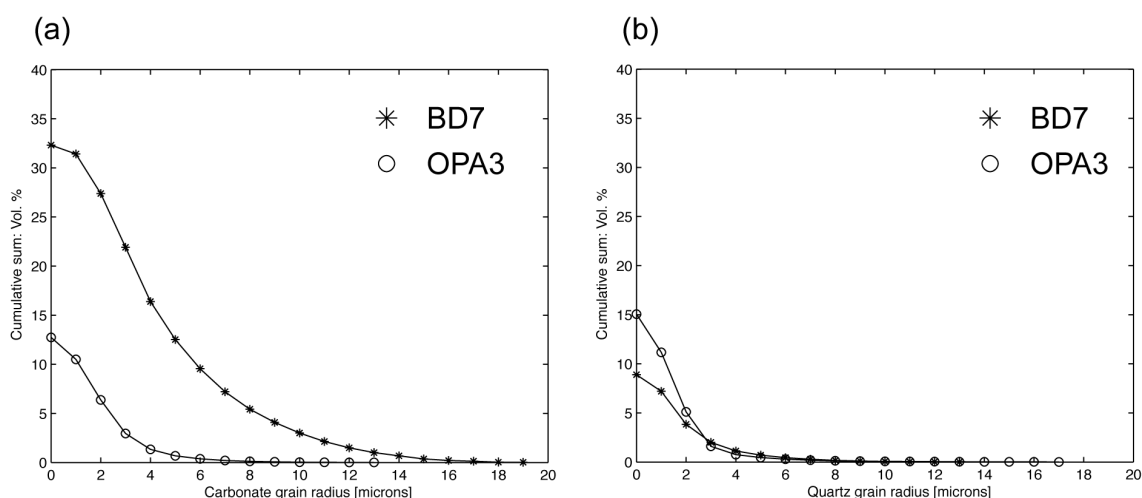


Fig. A-7: Grain size distribution of (a) carbonates and (b) quartz grains.

As a consequence, the manually selected “safe” regions used as seed for the watershed algorithm were obviously too small. However, part of discrepancy is also related to undetectable small grains, which reduces the inconsistency caused by segmentation uncertainties. Image contrast of BSE images is generally better when compared to XCT and segmentation should be associated with minor uncertainties. However, the discrepancy between results obtained by 2D BSE imaging and other methods is likely related to the comparable small-analyzed volume (i.e. area). As to be shown below, for length scales of a few hundred microns, the determination of mineral contents from a single 2D image is still affected by considerable error.

Microstructure of the clay matrix

Regarding material transport in shales, the clay matrix is of importance because it contains a network of pores, which serves pathways for transport. These nanoscale pores form because of geometric incompatibility between small clay grains and non-clayey grains. Internal pores in non-clayey grains can be found mainly in carbonates. These pores are, however, unconnected (Keller et al. 2013) and larger non-clayey grains resolved by XCT are therefore regarded as non-porous. Fundamental transport properties such as permeability of the clay matrix are controlled by the nano to micron scale microstructure of the pore space. Keller et al. (2013) showed that porosity in the clay matrix could be regarded as a sufficiently homogenous property on the few hundred micron-scale so that the clay matrix can be treated as continuum at higher-length scales where transport properties are controlled by microstructural properties of the clay matrix. In order to assess homogeneity and percolation properties of the clay matrix local porosity theory and classical percolation theory was applied to the 3D reconstructions of the clay matrix. In

addition, a statistical approach to calculate the RVE of clay matrix was applied in order to analyze the dependence of the RVE on the clay content. This paragraph summarizes the results obtained by the previously mentioned methods. All these calculations are based on a sub-volume analysis. Thereby, the analyzed volume is subdivided into a regular grid and clay content and connectivity were measured in cells or samples of different sizes L . For methodological details the reader is referred to Keller et al. (2013), who applied the same approach to the pore space of Opalinus Clay. With increasing L the local clay content distributions μ of the samples change from a wide distribution to a distribution with a single peak at the position of the bulk clay content (Fig. A-8). Regarding sample OPA-3 the formation of single peak distribution starts at smaller samples sizes L when compared to sample BD-7. Furthermore, the peak width of sample OPA-3 is smaller when compared to sample BD-7. These two facts indicate that the clay matrix of sample OPA-3 is more homogenous than the one of sample BD-7 and suggest that the homogeneity depends on clay content. Development of a single peak occurs for cells with edge lengths $L > \sim 100 \mu\text{m}$. Local clay content distributions μ can be regarded as a probability measure to find a local clay content within a cell or sample of certain size L . This means that at few hundred-micron scale length scales there is a high probability to find a local clay content that equals the bulk clay content, which in turn can only be true if the clay matrix, at this length scale, possesses a certain degree of homogeneity.

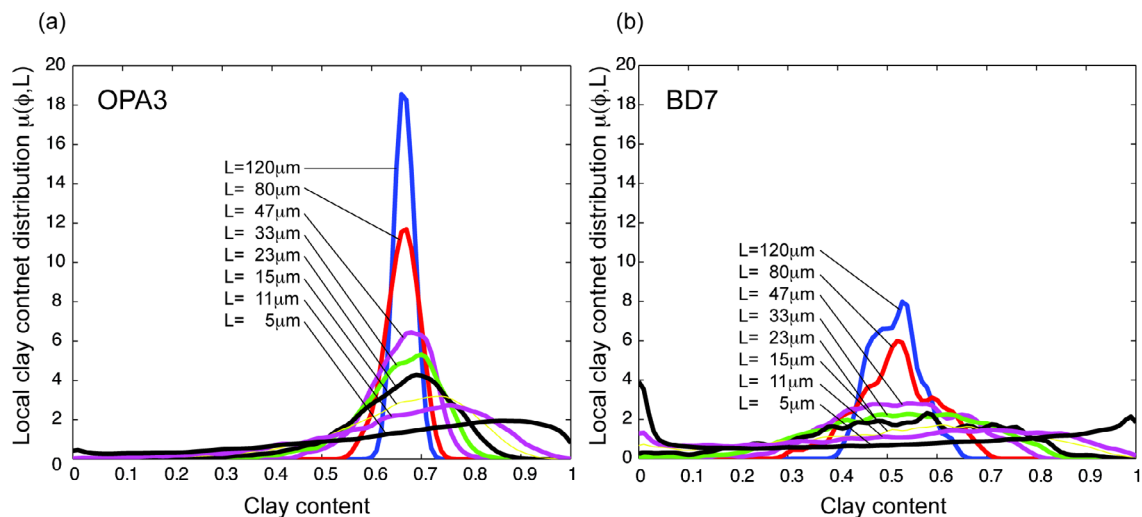


Fig. A-8: Local porosity distributions calculated for different length L of measuring cell and on the base of XCT data. a) OPA-3, b) Sample BD-7.

Calculated percolation probabilities for percolation along different directions as well as bulk percolation probabilities (i.e. simultaneous percolation along all principle directions) related to clay matrix are displayed in Fig. A-9. Smooth curves are fitted sigmoid function curves, which were used as input for the calculation of the percolation threshold (see below and Keller et al. 2013). The sigmoid functions were fitted to the data by using the simplex search method of Lagarias et al. (1998). Regarding sample BD-7, the positions of the curves corresponding to $L = 15 \mu\text{m}$ do not differ and the clay matrix is therefore considered as near isotropic in its connectivity. On the contrary, sample OPA-3 is less connected along x-direction (i.e. perpendicular to bedding) when compared to in bedding plane y- and z- directions. Figs. A-9c, d show to bulk percolation probabilities and the relative position between bulk clay content and the position of the curves gives an idea of the connectivity of the clay matrix. Concerning both

samples major connectivity changes for subsample sizes occur at lower clay contents as the bulk clay content. This indicates good connectivity of the sample.

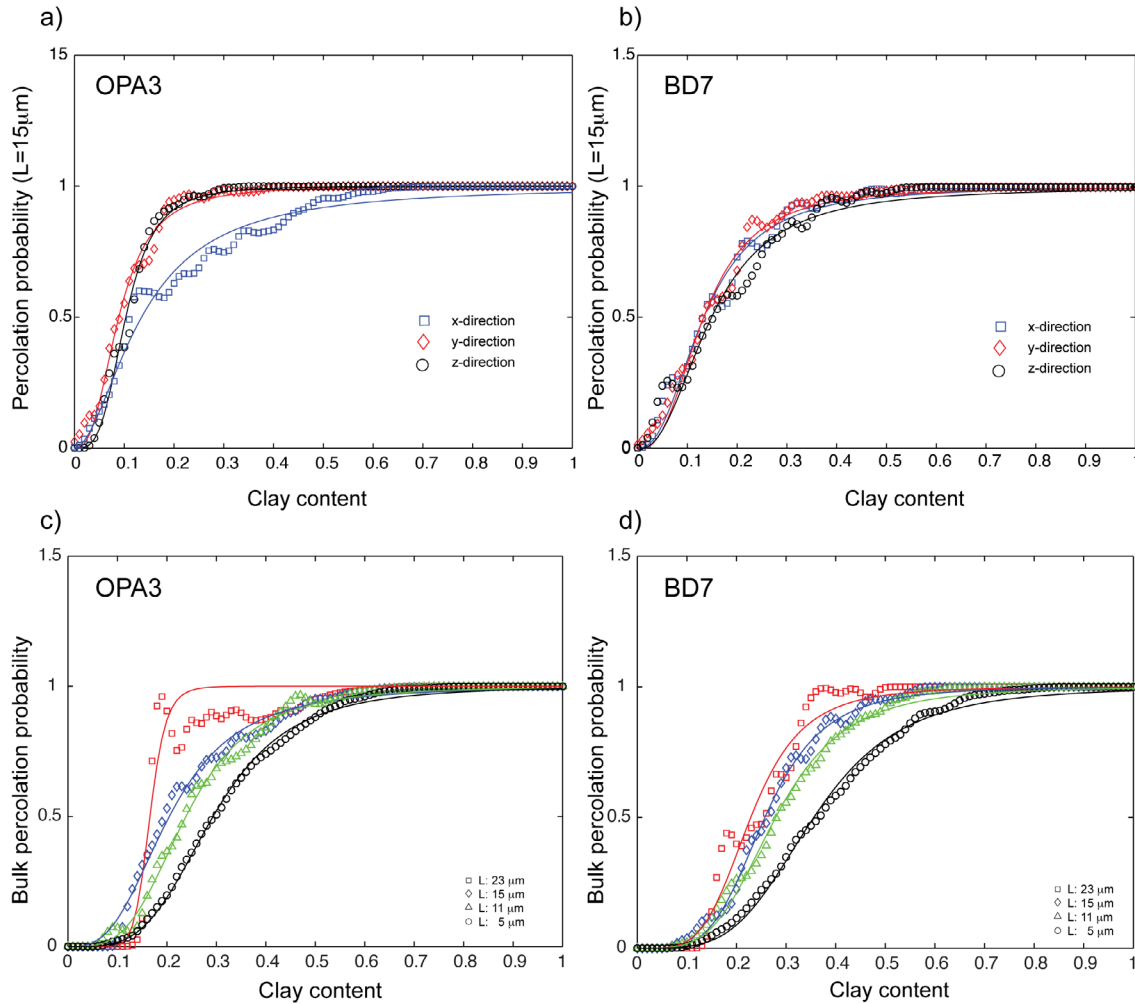


Fig. A-9: Percolation probabilities of clay matrix. a) and b) along different directions and for a cell size L of 15 μm . c) and d) are bulk percolation probabilities calculated for different cell sizes L . Symbols are computed values and lines smooth interpolations.

The critical clay content ϕ_c (i.e. percolation threshold) at which one can expect a full connectivity of the clay matrix is a crucial parameter. Here, two finite-size scaling schemes in combination with the results obtained from local percolation analysis were used to calculate the critical clay content (for details see Pringle et al. 2009; Keller et al. 2013). The calculations suggest that if clay content exceeds about 23 vol. % (i.e. highest value obtained) the clay matrix is very likely connected along all principle directions (Fig. A-10).

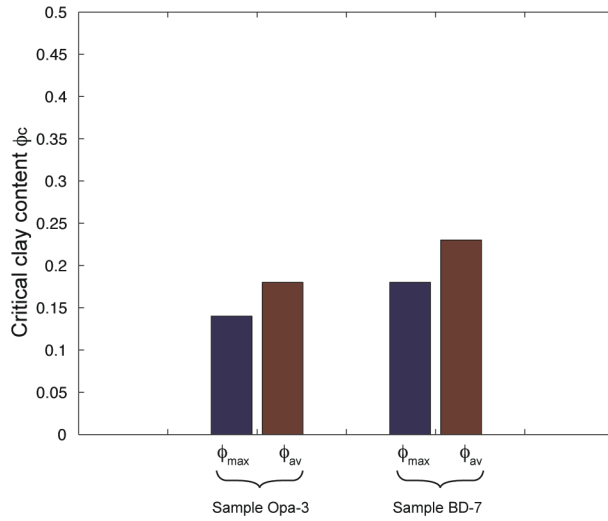


Fig. A-10: Bar plot shows a compilation of the calculated bulk percolation thresholds related to clay matrix of the. The values are grouped according to the applied scaling scheme (i.e. ϕ_{max} and ϕ_{av}).

The dependence of the size of RVE on clay content was calculated on the statistical approach outlined by Kani et al. (2003) (see also Keller et al. 2013 for some details). By inspection of Figure A-11 it can be seen that the mean clay content does not vary much with increasing cell size and that the associated interval of confidence decreases asymptotically.

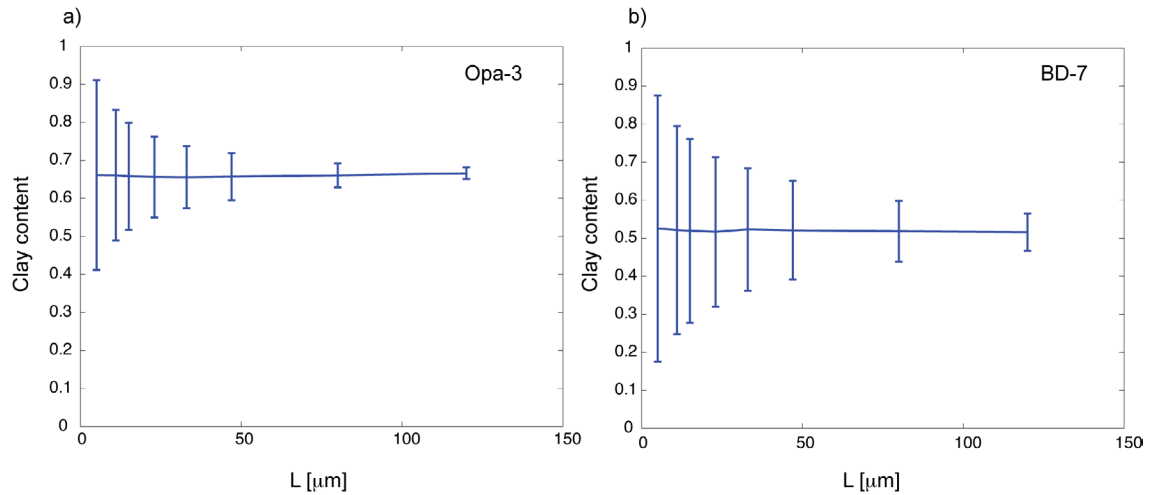


Fig. A-11: Mean value of clay content and intervals of confidence versus size of measuring cells L . (a) Sample OPA-3, (b) sample BD-7.

These results indicate that the true mean value of clay content can be predicted from a sample size that is smaller than the representative volume element (RVE) and that only a sample of infinite size will produce an error-free measurement. In this way of thinking, a realistic size of RVE (i.e. not too large), which can also be used for macroscopic modeling, should be calculated for an acceptable error. Kanit et al. (2003) provide an expression $V = \{(4[1-M_\phi]A_3)/(M_\phi N \varepsilon_r^2)\}^{1/\alpha}$ for the smallest volume V that must be measured to determine the clay content for a given relative error ε_r and number of realization N . The meaning and approach to determine parameters A_3 and α can be found in Keller et al. (2013b). The true mean value of clay content M_ϕ was set to the measured bulk clay content. This is supported by the fact that calculated mean values do not vary much in dependence of L . Then, the size of the RVE can be calculated for a given precision of the mean value that results from different realizations N (i.e. independent measures cells with the size of the RVE). For $N = 1$, Fig. A-12 shows the relative precisions ε_r in dependence of L_{RVE} .

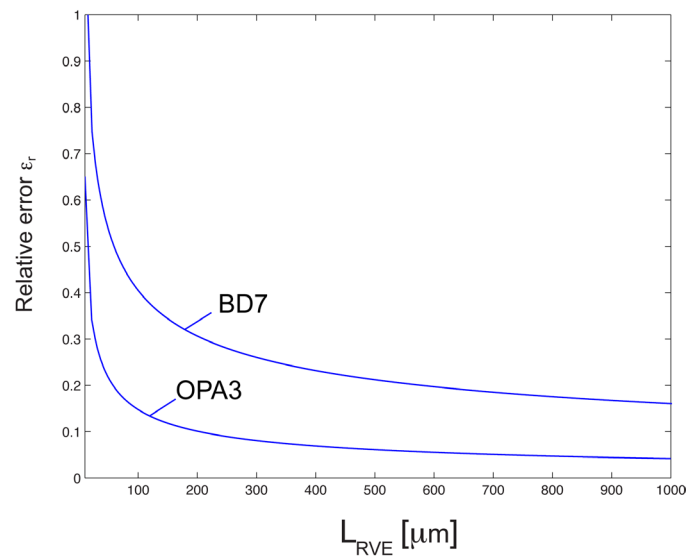


Fig. A-12: Relative error ε_r vs. RVE of clay matrix for a single XCT realization. The plot gives an idea of the relative error on clay content that is related to a single XCT scan. As an example: for a sample with volume edge length of 200 μm the relative error on clay content is about 0.1 for sample OPA-3 and about 0.3 for sample BD-7.

For a given relative error the size of the RVE is larger for sample BD-7 with low clay content when compared to sample OPA-3 with higher clay content (Table A-1). This suggests that the size of RVE of the clay matrix depends on clay content. This can plausibly be explained by realizing that the geometry of the clay matrix is in fact defined the microstructure of non-clayey grains. Sample BD-7 contains more, larger and a larger size spectrum of non-clayey grains when compared to sample OPA-3. Hence, in sample BD-7 a higher geometric complexity of the non-clayey grains/clay matrix microstructure can be expected, which then increase the size of the RVE. This lets to the speculation that size of the RVE related to the clay matrix is controlled by the grain size spectrum of non-clayey grains.

References

- A. Buades, B. Coll., and J.M. Morel, A non local algorithm for image denoising, in Proc. Int. Conf. Computer Vision and Pattern Recognition (CVPR), 2005, vol. 2, pp. 60-65.
- Kanit, T., S. Forest, I. Gailliet, V. Mounoury, and D. Jeulin (2003): Determination of the representative volume for random composites: statistical and numerical approach, *Int. J. Solids Struct.* 40, 3647-3679.
- Keller, L.M., L. Holzer, P. Schuetz, and P. Gasser (2013): Pore space relevant for gas permeability in Opalinus Clay: Statistical analysis of homogeneity, percolation and representative volume element. *Journal of Geophysical Research, Solid Earth*, 118, doi:10.1002/jgrb50228.
- Lagarias, J. C., Reeds, J. A., Wright, M. H. and Wright, P. E. (1998): Convergence Properties of the Nelder-Mead Simplex Method in Low Dimensions. *SIAM Journal of Optimization*, 9, 112-147 (1998)
- Robinet, J.-C., P. Sardini, D. Coelho, J.C. Parneix, D. Prêt, E. Boller, and S. Altmann (2012): Effects of mineral distribution at mesoscopic scale on solute diffusion in a clay-rich rock: example of the Callovo-Oxfordian mudstone Bure, France, *Water Resources Research*, 48, W05554
- Pringle, D. J., J. E. Miner, H. Eicken, and K. M. Golden (2009): Pore-space percolation in sea ice single crystals, *Journal of Geophysical Research*, 114, C12017.
- Revil, A., Cathles, L. M. (1999): Permeability of shaly sands. *Water Resources Reserach.* 35, 651-662.

B Pore-space in "Effingen Member": homogeneity, percolation and RVE of porosity

Lukas M. Keller

ZHAW, Zurich University of Applied Sciences, 8400 Winterthur, Switzerland

Summary

Local porosity theory in combination with percolation theory was applied to Effingen Member microstructures that were reconstructed on the base of Focused Ion Beam nanotomography (FIB-nt). This way we studied connectivity and spatial homogeneity of Effingen Member microstructures.

We observe a grain-supported microstructure with a framework of non-clayey grains (mostly carbonates), the majority of which have radii $< 2 \mu\text{m}$. Regarding two FIB-nt realizations, the fraction of larger pores ϕ (radii $> 20\text{nm}$) is in the 0.002-0.008 range. The majority of pores are located in the fine-grained clay matrix of which content is in the 0.13-0.29 range. If we consider that the pores are located in the clay matrix, its porosity is in the ~ 0.01 -0.06 range which is similar to the one of Opalinus Clay. Thus, low bulk porosity of the Effingen Schichten reflects comparable low clay content of the grain-supported microstructure.

Nanoporosity possesses a certain degree of homogeneity and we determined the RVE of porosity for a given relative error. For example, if we accept a relative error of 10%, the RVE is on the one cm range. This value is at least one order of magnitude higher when compared to the one of Opalinus Clay (i.e. $\text{RVE}_{\text{OPA}} \sim \text{few hundred-micron scale}$). The difference reflects stronger micron scale porosity fluctuations in the grain-supported microstructure where pores are separated by non-clayey grains.

The microstructure shows an anisotropy in connectivity and percolation threshold. Using two finite-scaling schemes we found percolation thresholds with critical porosities $\phi_{c,z} = 0.03$ -0.06, $\phi_{c,y} = 0.09$ -0.10 and $\phi_{c,x} = 0.11$ -0.16. Thus, for the analyzed samples we found the relation $\phi < \phi_c$ which shows that the pore space of the sample is clearly below to the percolation threshold so that gas transport along larger pores of the Effingen Member is not a likely scenario.

Analytical methods

The absolute size of the analyzed volumes, voxel size and bulk porosity related to the respective tomographic methods are documented in Table B-1.

Tab. B-1: Overview of properties of FIB-nt data sets.

Method	Size [μm^3]	Voxel size (nm) ³	Porosity	Resolved pore radii [nm]	Clay content [Vol. %]
FIB 1	1275	20 ³	0.008	≥ 20	13
FIB 2	2075	20 ³	0.002	≥ 20	29

Sample preparation

Electron microscopy requires drying of the samples prior to analysis. Conventional drying and/or freeze-drying of moist clay may cause preparation artifacts such as drying shrinkage (conventional drying), ice formation during freeze drying. Special methods such as high-pressure freezing and subsequent freeze-drying were used to avoid these artifacts. The sample preparation includes the following steps: Clay slabs with a thickness of 200 to 300 μm and a diameter of 5 to 6 mm were cut with the help of a saw with a very fine (thickness of saw blade = 200 μm) diamond blade parallel to the bedding plane. Then, the slabs were frozen under high pressure (2100 bar) and within milliseconds by using the HPM 100 high-pressure freezing system. Freezing at high pressure occurs by the injection of pressurized liquid nitrogen. This treatment prevents the formation of ice-crystals and thus preserves the delicate framework of the pore space. Then, the vitrified water was sublimated under high vacuum using a system for freeze-drying. Details of high-pressure freezing techniques and their application for cryofixation are given by . To stabilize the dry clay slabs, they were sandwiched between two 50 μm thick glass discs which were glued together with epoxy. Then, a cross-section was cut with a diamond saw perpendicular to the bedding plane. The surface of this cross-section was polished by using a broad ion beam (BIB) instrument and subsequently investigated by SEM and FIB-nt. SEM imaging of BIB polished clay samples is used for a material characterization on the mm-scale (for comparison: typical sample size of the FIB-nt analyzed volume is a cube of 10-30 μm edge length).

Focused ion beam nanotomography

FIB-nt is done with dual beam FIB-SEM instruments, in which an ion beam and an electron beam focus intersect at a point on the sample surface. 3D information can be obtained by acquiring a sequence of cross sectional images spaced evenly through a region of a bulk specimen, and reconstructing those two-dimensional images into a three-dimensional representation of the sampled volume. The process begins by the milling of a wedge shaped trench in the sample. One wall of the trench is vertical (i.e., normal to the specimen surface) and becomes the initial cross section imaged by the electron beam. After imaging, the ion beam is used to remove a layer of uniform thickness of material from this wall, advancing the cross section a predetermined distance through the sample volume. Another electron image is collected. By repeating this milling/imaging process, the cross section advances through the targeted volume, which results in a stack 2D images. Two image stacks were collected (see above and Figs. B-2, A-3, Table B-1).

Sample

The analyzed sample is from the Schlattigen borehole (depth 739m) and belongs to the "Effingen Member".

Micro- to macro- scale structures based on BIB and SEM imaging

Panoramic SEM images on the hundreds of micron scale of the prepared samples are shown in Fig. B-1. The SEM images reveal a grain-supported texture where non-clayey grains are largely touching (Fig. B-1). The major part of non-clayey mineral grains is carbonate but few quartz grains were also observed.

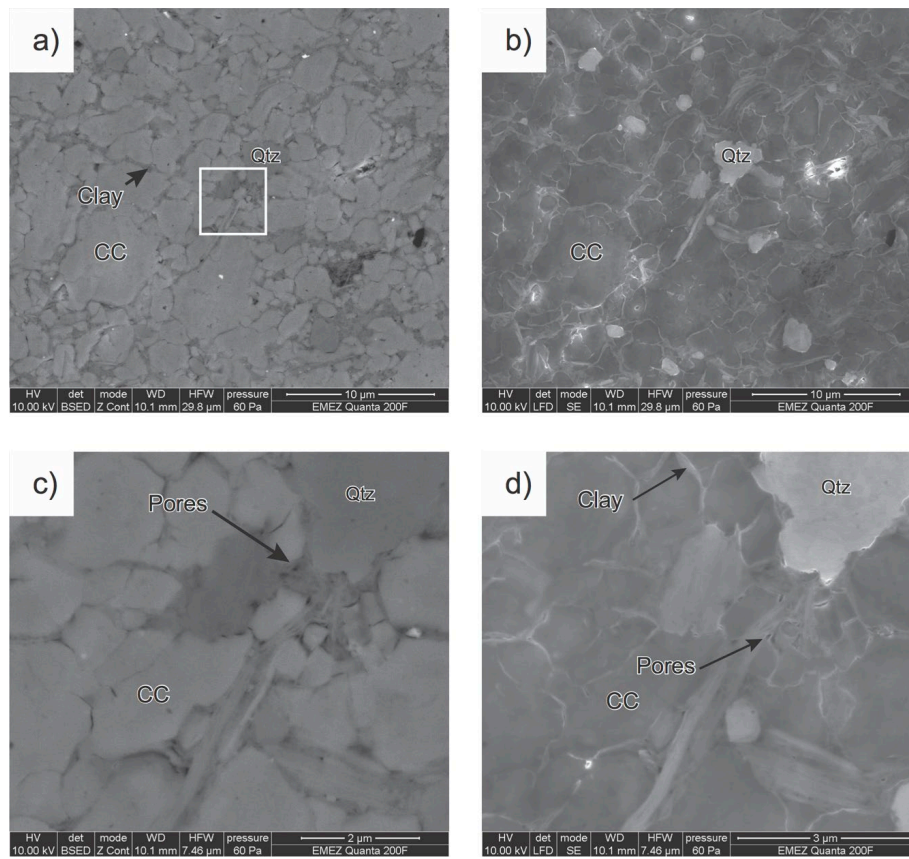


Fig. B-1: (a, c) BSE (back-scatter) and (b, d) LFD (large-field) images of a sample taken from the Effingerschichten. Images were made from BIB-polished surfaces. BSE images show phase contrast whereas the LFD detector was used to visualize the fine-grained clay grains between non-clayey grains (platy bright minerals between carbonates in b and d) (CC = carbonates, Qtz = quartz). The white rectangle marks the area which was imaged at higher resolution (c, d). The majority of the pores are within the fine-grained clay matrix are formed due to geometric incompatibilities between platy clay grains and more granular non-clayey grains.

Nano- to micro- scale structures based on FIB-nt

In order to analyze grain size of non-clayey grains, the touching grains (Figs B-2a, B-3a) were separated by an imaging technique known as watershed grain separation. The resulting grain microstructure is displayed in Figs B-2b, B-3b and calculated grains size distributions are shown in Fig. B-4.

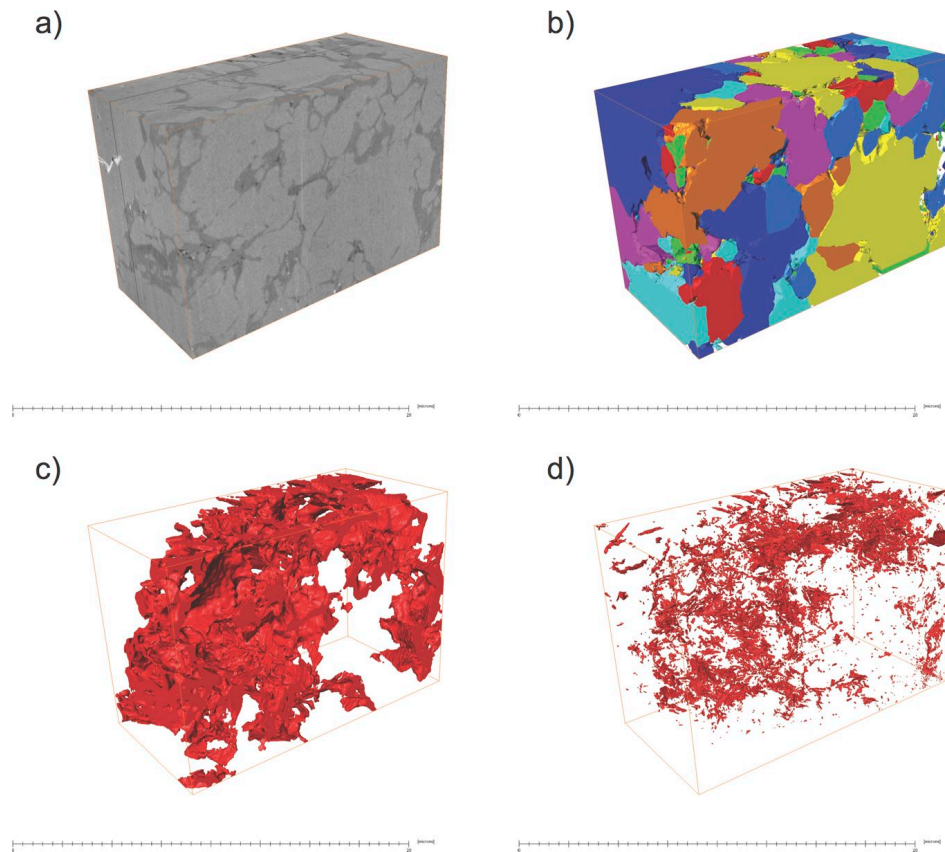


Fig. B-2: Stages of FIB-nt data processing. (First realization) a) 3D reconstruction of the analyzed volume based on BSE images. b) 3D reconstruction of the framework of the non-clayey grains. Colors are label colors of individual grains. Grains were separated using watershed separation. c) 3D structure of the clay matrix. d) 3D reconstruction of the pore space which is based on segmented SE images. The reconstructions reveal that a major part of the pore space is localized in the clay matrix.

Most non-clayey grains have radii $< 2 \mu\text{m}$ but with a substantial fraction of grains with radii $< 1 \mu\text{m}$ (Fig. B-4). Clay minerals fill the space between the non-clayey grains and the clay content determined for the first and second FIB-nt realization is 0.13 and 0.29 (Table B-1). Concerning the sample size that can be analyzed by FIB-nt, the clay content is connected along all directions.

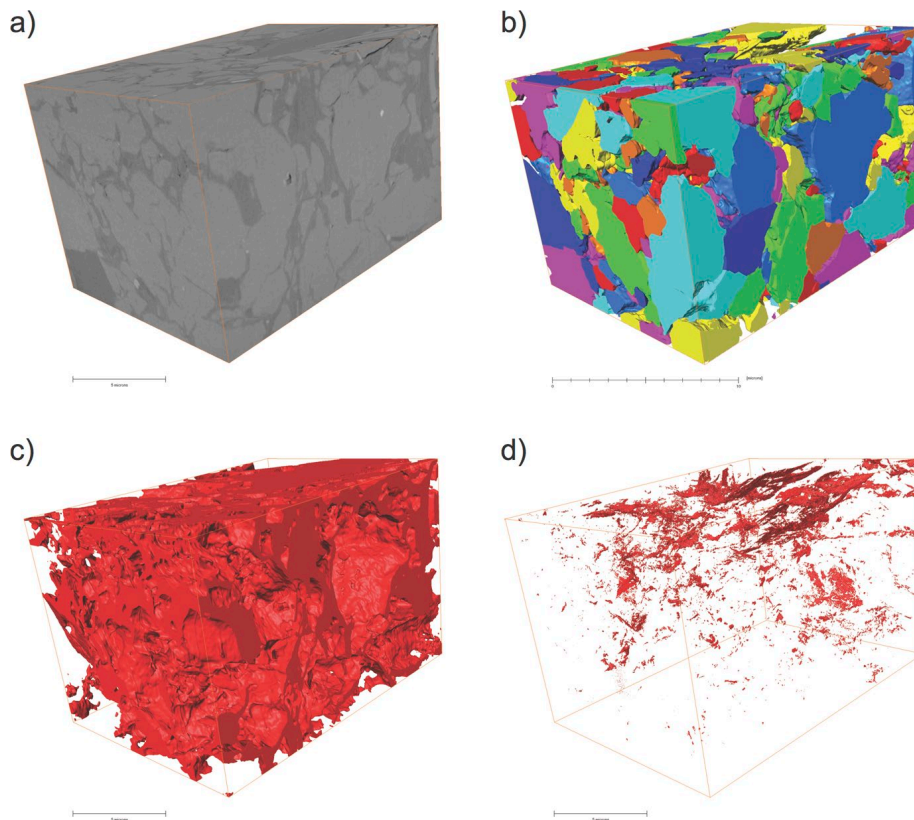


Fig. B-3: Stages of FIB-nt data processing. (Second realization) a) 3D reconstruction of the analyzed volume based on BSE images. b) 3D reconstruction of the framework of the non-clayey grains. Colors are label colors of individual grains. Grains were separated using watershed separation. c) 3D structure of the clay matrix. d) 3D reconstruction of the pore space which is based on segmented SE images. The reconstructions reveal that a major part of the pore space is localized in the clay matrix.

The 3D pore structures in the clay matrix are displayed in Fig. B-2c, B-3c. The resolved porosity ϕ in the first and second FIB-nt realization is 0.008 and 0.002, respectively. The resolved pore radii range between 20 and about 200 nm with the majority of the pores having radii < 50 nm (Fig. B-4) (Muench & Holzer 2008). On the first glance porosity in Effingen Member appears substantial lower when compared to Opalinus Clay. If we, however, consider that the pores are mainly found within the fine-grained clay matrix and if we relate the pore volume to the volume of the fine-grained matrix, the porosity of the clay matrix of the first and second FIB-nt realization is 0.06 and 0.01. This porosity range is similar to the one of Opalinus Clay and suggests that bulk porosity of the Effingen Member is related to the clay content.

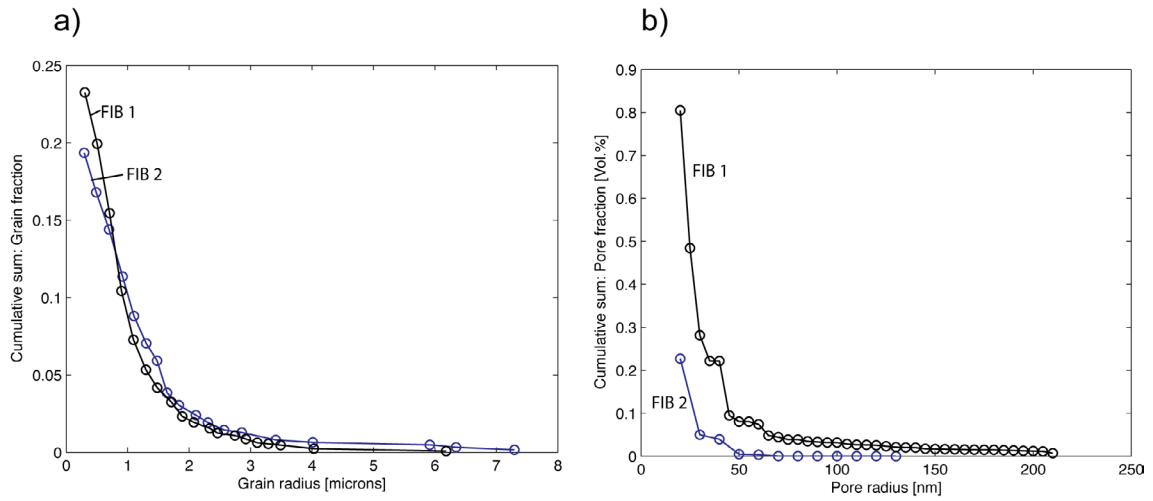


Fig. B-4: (a) Grain size distribution of grains depicted in Figs B-2b and B-3b. b) Continuous pore size distributions of pores depicted in Figs B-2d and B-3d.

Local porosity analyses

The local porosity distributions $\mu(\phi, L)$ (see appendix) corresponding to the nano-porosity in the clay matrix are displayed in Fig. B-5.

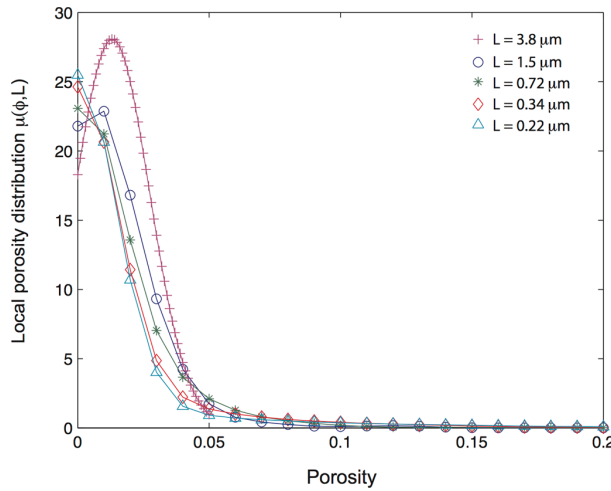


Fig. B-5: Local porosity distributions calculated for different length L of measuring cell.

With increasing L the μ curves change from a wide distribution to a distribution with a single peak at the position of the bulk porosity. Development of a single peak occurs for cells with edge lengths $L > 3.8 \mu\text{m}$. This means, that at this length scale there is a high probability to find a local porosity that equals the bulk porosity, which in turn can only be true if the pore space, at this length scale, possesses a certain degree of homogeneity. In addition, the function component at the origin decreases with increasing L (Fig. B-5). All these indicate that similarities between local geometries increase with increasing L . It also indicates that the nano-porosity in the clay matrix possesses a certain degree of homogeneity on the few micron scale.

Local percolation analyses

Calculated percolation probabilities $\lambda_\alpha(\phi, L)$ related to nanoporosity in the clay matrix are displayed in Fig. B-6. Smooth curves in Fig. B-6 are fitted curves, which were used as input for the calculation of the percolation threshold (see below).

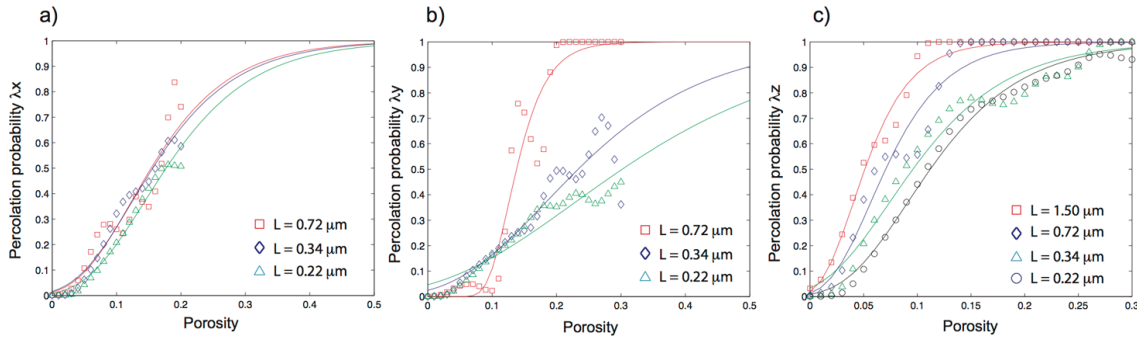


Fig. B-6: Percolation probabilities $\lambda_\alpha(\phi, L)$ along different directions. Symbols are computed values and lines smooth interpolations. a) x-direction, b) y-direction and c) z-direction.

One notices that the clay porosity is anisotropic in its connectivity. Sample has a higher connectivity in z direction when compared to the x and y directions (i.e. a higher percolation probability in z direction). However, major connectivity changes occur at much higher porosities when compared to the bulk porosity of the sample. This indicates that nanopores are very poorly connected. Thus, long-range percolation along the pores space is rather unlikely (see also below).

Percolation threshold

The critical porosity at which one can expect a percolating pore network is a crucial parameter. Here, we used two finite-size scaling schemes in combination with the results obtained from local percolation analysis (Pringle et al. 2009).

Percolation threshold based on finite-size scaling

The calculated percolation probability $\lambda_\alpha(\phi, L)$ can be regarded as the probability that a sample with a given porosity ϕ and size L percolates along a direction α (Stauffer & Aharony 1995). For infinite (i.e. large L) L and if ϕ is below a critical value ϕ_c there is no percolating path across the sample, whereas for small L it is possible to find a percolating path even if $\phi < \phi_c$. This is the present situation for the nanoporosity where we have $\lambda_\alpha(\phi < \phi_c) = 0$ for the sample size that can be analyzed by FIB-nt. For subvolumes, however, we found $\lambda_\alpha(\phi, L) > 0$. The question is now how can we determine the critical value ϕ_c (i.e. percolation threshold) for an infinite sample from the calculated $\lambda_\alpha(\phi, L)$ curves related to small values of L . Regarding percolation theory, this can be done by a technique known as finite-scaling (Stauffer & Aharony 1995). For an infinite sample, $\lambda_\alpha(\phi, \infty)$ is a step function with $\lambda_\alpha(\phi < \phi_c) = 0$ and $\lambda_\alpha(\phi > \phi_c) = 1$. This transition widens as sample size decreases (Fig. B-6). Fig. B-6 shows that the porosity range of our samples does not cover full transition from $\lambda_\alpha(\phi, L) = 0$ to 1 for all L . To improve the covered porosity range and to avoid influence of local percolation fluctuations we analyzed smooth curves fit to our data (see also Pringle et al. 2009). The derivation $d\lambda/d\phi$ is essentially the

probability of the first occurrence of a percolating sample with porosity ϕ (Stauffer & Aharony 1995). If we define the effective percolation threshold as the porosity with maximum probability ϕ_{\max} for first occurrence, ϕ_{\max} can be found by calculating the point of inflection of $\lambda(\phi)$ (i.e. porosity with maximum of $d\lambda/d\phi$) (Stauffer & Aharony 1995; Pringle et al. 2009). The point of inflection converges to ϕ_c as (Stauffer & Aharony 1995):

$$\phi_{\max} - \phi_c \propto L^{1/\nu}, \tag{BA-1}$$

where ν is the critical exponent of the correlation length, which has a universal value depending only on the system dimension and in 3D we have $\nu = 0.88$ (Bunde & Havlin 1995); Pringle et al. 2009).

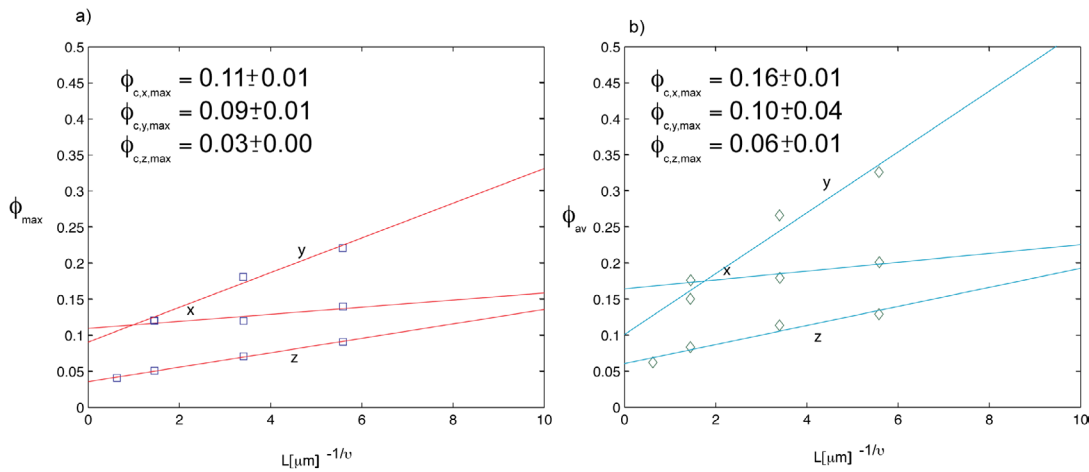


Fig. B-7: (a) ϕ_{\max} and b) ϕ_{av} vs. $L^{-1/\nu}$. Lines are least square fits of which intercept values are given in the plots and are considered as percolation thresholds.

Fig. B-7 shows a plot of numerically calculated ϕ_{\max} vs. $L^{-1/\nu}$. $L^{-1/\nu}$ decreases with increasing L , which implies that for $L \rightarrow \infty$ the value for the infinite size limit is given by the vertical axis intercept (Pringle et al. 2009). A linear least square fit yielded an intercept values for percolation in different directions (Fig. B-7).

A similar behavior is shown by ϕ_{av} , the average porosity at which a percolating cluster appears for the first time. This is defined by (Stauffer & Aharony 1995)

$$\phi_{av} = \int_0^1 \phi \left(\frac{d\lambda}{d\phi} \right) d\phi \tag{BA-2}$$

Then, a similar scaling scheme (i.e. $\phi_{av} - \phi_c = L^{-1/\nu}$) as for ϕ_{\max} is applied (Pringle et al. 2009). Numerically calculated values of ϕ_{av} are plotted vs. $L^{-1/\nu}$ and a linear least square fit yielded an intercept values for the different percolation directions (Fig. B-7). Concerning the Effingen Member, the calculations yielded values for the percolation threshold in z-direction $\phi_{c,z}$ and y-direction $\phi_{c,y}$ that range between 0.03–0.06 and 0.09–0.10, respectively. Percolation threshold

in x-direction is higher and ranges between 0.11-0.16. Note, that the found thresholds are restricted to the pore spaces that were resolved by FIB-nt (Table B-1).

RVE of porosity

Local porosity analysis shows that porosity possesses a certain spatial homogeneity on the few micrometer scale. However, at this length scale the mean porosity is still related to an error, which decreases asymptotically with increasing L (Fig. B-8a).

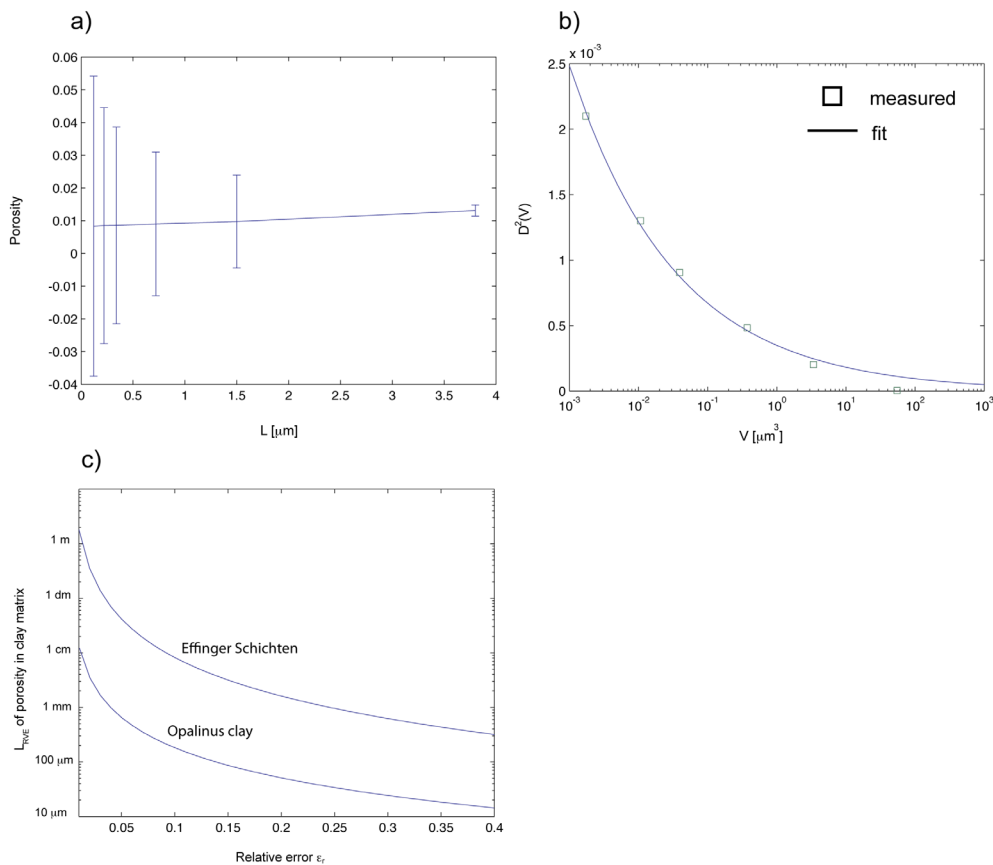


Fig. B-8: (a) Mean value of porosity and intervals of confidence versus size of measuring cells L . b) variances of porosities vs. volume of measuring cells. c) RVE of porosity vs. relative error ϵ_r for Effingen Member and Opalinus Clay.

In addition, the mean porosity does not vary much in dependence of L . These results indicate that the true mean value of porosity can be predicted from a sample size that is smaller than the RVE and that only a sample of infinite size will produce an error-free measurement. In this way of thinking, a realistic size of RVE (i.e. not too large), which can also be used for macroscopic modeling, should be calculated for an acceptable error. In what follows and in order to calculate the size of the RVE for a given error we used the method which is outlined by Kanit et al. (2003) and references therein. Based on classical sample theory, the relative error on the exact mean value of porosity M (or volume fraction in general), obtained from N independent realization of volume V , is given by:

$$\varepsilon_r = \frac{2D_\phi(V)}{M_\phi \sqrt{N}}, \quad (\text{BA-3})$$

where $2D(V)$ is the interval of confidence. Following Kanit et al. (2003) the variance of porosity is given by:

$$D_\phi^2(V) = \frac{M_\phi(1-M_\phi)A_3}{V^\alpha}, \quad (\text{BA-4})$$

where A_3 is referred as to the integral range which gives information of the domain size of the pore structure for which the porosity in the measured volume V has a good statistical representativity. For a finite integral range $\alpha = 1$ and in the case of an infinite integral range $\alpha \neq 1$ (Lantuejoul 1991; Kanit et al. 2005). Using Eq. (AA-3) in Eq. (AA-4) gives an expression for the smallest volume with a given relative error ε_r , N realization and the true mean value M :

$$V(N, \varepsilon_r) = \left(4 \frac{(1-M_\phi)}{M_\phi} \frac{A_3}{N \varepsilon_r^2} \right)^{1/\alpha}. \quad (\text{BA-5})$$

The integral range A_3 for porosity was approximated by computing the variance $D^2(V)$ for the recorded porosities of the respective measuring cells of size V . Then, the integral range A_3 was obtained by fitting equation (4) to our data (Fig. 8b). Here one has the problem that the true mean value M of porosity or clay content cannot be predicted from tomographic methods because they have been applied to volumes, of which sizes are far from infinite. The latter statement assumes the true porosity can be obtained from a rock body of infinite size. The calculated RVE is not only related to an error and number realizations N but also to the respective microstructural level that can be resolved by FIB-nt. Here, we assumed that bulk volume fraction of porosity is a valid estimate of the true volume fractions. This is supported by the fact that calculated mean values do not vary much in dependence of L . The values of A_3 , α and volume fractions for each method are $0.044 [\mu\text{m}^3]$ and 0.285 , respectively. Then, the size of the respective RVE can be calculated for a given precision of the mean value that results from different realizations N (i.e. independent measures cells with the size of the RVE). For $N = 1$, Fig. B-8c shows the L_{RVE} for relative precisions ε_r . For example, if we tolerate an ε_r of 10%, the RVE of porosity is in the 1 cm range (Fig. 8c). This is more than order of magnitude larger than the RVE of Opalinus Clay. This is because the pores, which are located in the fine-grained clay matrix, are more dispersed in the grain-supported microstructure of the Effingen Member when compared to a clay-matrix supported microstructure of Opalinus Clay (BDR1_oc).

Discussion and Conclusions

The microstructure of the analyzed Effingen Member from the Schlattingen borehole is a grain-supported microstructure in which the framework of non-clayey grains are characterized by grain radii $< 2 \mu\text{m}$. The clay content is in the $\sim 13\text{-}30$ vol. % range and bulk sample porosity is < 1 vol. %, which is substantial lower when compared to the one of Opalinus Clay. If we consider that the pores are located in the clay matrix, its porosity is in the $\sim 1\text{-}6$ vol. % range

which is similar to the one of Opalinus Clay. Thus, low bulk porosity of the Effingen Member reflects comparable low clay content of the grain-supported microstructure.

The nanoporosity in the clay matrix of the Effingen Member possesses some spatial homogeneity on the few micron scale. On this length scale, however, the relative error associated to the mean value of porosity is $> 10\%$. If we accept a relative error of 10% , the RVE of porosity is on the cm scale and is at least one order of magnitude larger when compared to the RVE of Opalinus Clay. This, reflects stronger micron scale porosity fluctuations in the grain-supported microstructure when compared the more homogenous clay-matrix supported microstructure of Opalinus Clay.

The clay matrix is fully connected on length scales that can be analyzed by FIB-nt. However, the pore space in the clay matrix is very poorly connected due to the presence of non-clayey grains.

Regarding pores with radii > 20 nm, we found a percolation anisotropy. Percolation threshold in clay the matrix is as low as $\sim 0.03 - 0.06$. The measured fraction of larger pores (i.e. radii > 20 nm) is, however, much lower (i.e. < 0.01). Because larger pores control gas transport, this implies that gas percolation is not reasonable in the Effinger Member.

Addendum

Input format of 3-D Data

The segmented images were transferred into binary images, in which the pores were set to white and the remaining area to black. The resulting images are two-dimensional arrays of ones (i.e. white) and zeros (i.e. black). The images were then read into three-dimensional arrays of 0's and 1's, in which the ones indicate the pore space. The analysis of XCT data should reveal the influence of non-clayey mineral grains and layers on the degree of homogeneity of the clay matrix. Thus, images obtained by XCT are arrays, in which the 0's and 1's indicate mineral grains (e.g. calcite and quartz) or clay matrix, respectively. The voxel arrays were then regularly subdivided into cubic sub-arrays of $N*N*N$ voxels. This operation divides the analyzed volume into a regular cubic grid/lattice, in which each cell $K(x, L)$ is located a position x and has an edge length L that corresponds to a certain number of voxels. Once the image stacks are subdivided into such a grid it is possible to determine quantities (e.g. porosity, clay content and connectivity) for each cell $K(x, L)$, which are then used as input for the calculation of the local porosity distribution. For the small data sets available, the use of non-overlapping cells led to poor statistics with strong fluctuations in the results. To overcome this problem we used overlapping cells (see also Biswal et al. 1998).

Local porosity theory

To characterize the heterogeneity of the material and to evaluate the representativeness of tomographic methods in characterizing the pore space we followed the approach outlined in (Hilfer 1991; Biswal et al. 1998; Hu & Stroeven 2005; Hilfer & Helmig 2004). Based on the gridded 3D array (see above), the local porosity $\phi(x, L)$ can then be measured in each cubic cell $K(x, L)$ by counting the numbers of pore voxels. The local porosity distribution is then defined as:

$$\mu(\phi, L) = \frac{1}{m} \sum_{i=1}^m \delta(\phi - \phi(x_i, L)) \quad (BB-1)$$

where m is number of placements of measurement cells and $\delta(t)$ denotes the delta function (sometimes called the Dirac delta function). The function $\mu(\phi, L)$ is a measure for the probability to find the local porosity ϕ in a cell with side length L .

Regarding permeability and material transfer the question whether or not a pore space percolates is fundamental. A cell $K(x, L)$ is considered as percolating in x -direction if there exists a continuous path along the pores space which connects the two faces perpendicular to the x -direction. This definition is also applied to the other directions. The following formulation is used as an indicator for percolation.

$$\Lambda_\alpha(x, L) = \begin{cases} 1 & \text{if } K(x, L) \text{ percolates in } \alpha \text{ direction} \\ 0 & \text{otherwise} \end{cases} \quad (BB-2)$$

As an example, Λ_3 indicates that a cell can be traversed along in all three directions, while Λ_1 indicates that there exists at least one direction along which the cell is percolating. Λ_0 indicates a blocking cell.

The local percolation probability is then defined by:

$$\lambda_\alpha(\phi, L) = \frac{\sum_{i=1}^m \Lambda_\alpha(x_i, L) \cdot \delta(\phi - \phi(x_i, L))}{\sum_{i=1}^m \delta(\phi - \phi(x_i, L))} \quad (BB-3)$$

where $\lambda_\alpha(\phi, L)$ is the fraction of cells with local porosity ϕ and side length L that allow percolation in α -direction. A pore space is fully connected if $\lambda_3 = 1$. In practice, the Dirac delta function $\delta(t)$ is seen as kind of limit of a sequence of functions having a tall spike at the origin. Different approximating functions can be defined. Here we used the following function

$$\delta(t) = \frac{1}{2\sqrt{\pi\zeta}} e^{-\frac{t^2}{4\zeta}} \quad \text{with } \zeta = 0.00001. \quad (BB-4)$$

When plotted against t the above function appears as a narrow spike at $t = (\phi - \phi(x, L)) = 0$ and vanishes outside a very narrow range symmetric around $t = 0$. Thus, if a certain locale porosity is found within a cell, the function acts as a kind of an "impulse response function" and in combination with Eq. (BB-1) collects the response of local porosities and yields and continuous functions of local porosity density. The determination of $\Lambda_\alpha(f, L)$ requires the determination of the connected pore regions in the measuring cell. The Matlab® function 'bwlabeln' labels the connected regions and thus, allows determining whether these regions connect the faces of the measuring cell or not.

References

- Biswal, B., Manwart, C., Hilfer, R. (1998) Three-dimensional local porosity analysis of porous media, *Physica, A* 255, 221-241.
- Bunde, A., Havlin, S. (1995). Percolation I, in *Fractals and Disordered Systems*, edited by A. Bunde and S. Havlin, pp. 59-114, Springer, Berlin.
- Hilfer, R. (1991). Geometric and dielectric characterization of porous media. *Physical Review*, 44, 60-75.
- Hilfer, R., Helmig, R. (2004). Dimensional analysis and upscaling of two phase flow in porous media with piecewise constant heterogeneities, *Advances in water resources*, 27, 1033-1040.
- Hu, J., Stroeven, P. (2005) Local analysis of pore structure in cement paste, *Cement and Concrete research*, 35, 233-242.
- Kanit, T., Forest, S., Gailliet, I., Mounoury, V., Jeulin, D. (2003). Determination of the representative volume for random composites: statistical and numerical approach. *Int. J. Solids Struct.* 40, 3647-3679.
- Lantuejoul, Ch. (1991) Ergodicity and intergral range, *Journal of Microscopy*, 161, 387-403.
- Liu, J., Regenauer-Lieb, K. (2011). Application of percolation theory to microtomography of structured media: Percolation threshold, critical exponents, and upscaling. *Physical Review, E* 83, 016106-1-13.
- Matheron, G. (1971). *The theory of regionalized variables and its application*, Paris School of Mines Publications.
- Münch, B., Holzer, L. (2008). Contrasting geometrical concepts in pore size analyzes attained with electron microscopy and mercury intrusion. *Journal of American Ceramic Society* 91, 4059-4067.
- Pringle, D. J., Miner, J. E., Eicken, H., Golden, K. M. (2009). Pore-space percolation in sea ice single crystals. *Journal of Geophysical Research*, 114, C12017.
- Stauffer, D., Aharony, A. (1995). *Perkolationstheorie – Eine Einführung*. VCH, Weinheim, New York, Basel, Cambridge, Tokyo, 202p.